Spring 4-13-2022

Reliability of Quantum Simulation on NISQ-era Devices

Karthik R. Chinni
University of New Mexico

Karthik Chinni

Candidate

Physics and Astronomy

Department, The University of New Mexico

This dissertation is approved, and it is acceptable in quality and form for publication:

Approved by the Dissertation Committee:

Ivan H. Deutsch (Chair)

Pablo M. Poggi

Tameem Albash

Poul S. Jessen

Defended February 9th, 2022.

Reliability of Quantum Simulation on NISQ-era Devices

by

Karthik Chinni

M.S., Physics, University of New Mexico, 2018
B.S., Physics, Southern Illinois University Carbondale, 2015
B.S., Electrical Engineering, Southern Illinois University Carbondale, 2015

DISSERTATION

Submitted in Partial Fulfillment of the
Requirements for the Degree of

Doctor of Philosophy
Physics

The University of New Mexico
Albuquerque, New Mexico

May, 2022

To my parents and my sister for all their support.

Acknowledgments

This dissertation would not have been possible without the support of many people. First and foremost, I would like to thank my advisor Ivan Deutsch for his support and guidance throughout the course of my PhD. He was always encouraging and patient. I have enjoyed thoroughly working under his supervision and learned very much about being a physicist. Next, I am very thankful to Pablo Poggi, who was always available to chat with me about my research projects, and played a significant role in all of my projects. I have learned a great deal about research work, among many other things. I am also very grateful to my committee members, Tameem Albash and Poul Jessen, for their feedback on my dissertation. I would also like to thank Elizabeth Crosson for all the insightful discussions on my work.

Next, I would like to thank Nitant Kenkre for his support and wisdom. I was always inspired by his enthusiasm about physics and feel very fortunate to have had the opportunity to work as his teaching assistant. I also want to express my sincere thanks to Mark Byrd, who has first inspired me to work in the field of quantum information and computation at my undergraduate institution. I am also grateful for the support provided by my undergraduate faculty Thushari Jayasekera, Eric Chitambar and Richard West.

I want to thank postdocs and my senior students at UNM, namely Gopi, Rafael, Sayonee, Chris, Anirban, Anastasia, Satomi, Tzu-Cheng, Ezad and Xi, for all their guidance throughout my time at UNM. Particularly, special thanks to Gopi, who was very helpful when I first started working under Ivan, and provided me all the career advice. I am also grateful to all the graduate students in Ivan's group, Manuel, Anupam, Siva, Vikas and Andrew Forbes, whose support made this endeavor easier. I have benefited greatly from working with Manuel on multiple projects. Thanks to Poul's group at the University of Arizona, particularly Kevin, for all the insightful discussions about my work. Finally, thanks to all of my friends and colleagues at CQuIC for the informative discussions and support: Austin, Changhao, Andrew Zhao, Sam, Tyler, Philip, Jun and Mitchell.

Reliability of Quantum Simulation on NISQ-era Devices

by

Karthik Chinni

M.S., Physics, University of New Mexico, 2018
B.S., Physics, Southern Illinois University Carbondale, 2015
B.S., Electrical Engineering, Southern Illinois University Carbondale, 2015
Ph.D., Physics, The University of New Mexico, 2022

ABSTRACT

We study the reliability of quantum simulation on Noisy intermediate-scale quantum (NISQ)-era devices in the presence of errors and imperfections, with a focus on exploring the relationship between the properties of the system being simulated and the errors in the output of the simulator. We first consider simulation of the Lipkin-Meshkov-Glick (LMG) model, which becomes chaotic in the presence of a background time-dependent perturbation. Here we show that the quantities that depend on the global structure of the phase space are robust, while other quantities that depend on the local trajectories are fragile and cannot be reliably extracted from the simulator. Next we analyze the effects of Trotterization on the simulation of p-spin models. We show that even in the absence of chaos, Trotter errors proliferate in the "structural instability regions", where the effective Hamiltonian associated with the Trotterized unitary becomes very different from the target p-spin Hamiltonian.

Contents

List of figures

1

Introduction

The world's first documented "computer" dates back to circa 150 B.C. when Antikythera Mechanism device was used to predict astronomical phenomena [GG18]. It was a hand-held device consisting of interlocking mechanical gears, enclosed in a wooden case, that would accurately predict the future location of planets. It was about the size of a mantel clock with a knob on the side that would allow the device to move forward or backward. As the knob was turned, the hands in the device would display celestial time with at least seven hands, each one displaying the location of sun, moon and other five planets that are visible to the naked eye [FHD+21]. This de-

vice is an example of an analog "computer" that used the one-to-one correspondence between the physical position of the astronomical bodies and the mechanical system to simulate the location of the planets.

In the last century, there have been significant advancements in the field of classical computing. To start with, there have been many developments on the theoretical side such as Shannon's idea of using Boolean algebra for describing electrical switches and Alan Turing's idea of Turing machine that eventually lead to the development of a general-purpose computer [GG18]. The first digital, programmable, general purpose computer, ENIAC was built in the year 1945 [McC99]. The ENIAC consumed about 2000 times the electricity of a modern computer and used $18,000$ vacuum tubes. With the invention of transistors in the year 1947, which were smaller and consumed little power compared to the vacuum tubes, the development of modern-day computers was accelerated. The next breakthrough in integrated circuits in 1960s allowed the computer size to be reduced significantly and the idea of personal computer soon became a reality.

Noticing the significant improvement in the power of computer hardware after the discovery of transistors, Robert Moore in the year 1975 made a prediction that the number of transistors on a chip, which can be regarded as equivalent to the computational power of the computer, would double every year beginning in 1975 [McC99]. This prediction has been proven correct and referred to as Moore's law. However, we are reaching the fundamental limitations on how small transistors can be made, and Moore's law cannot hold true for long time in future within the framework of classical computing. A path forward that would further improve the power of

computing is to move to a different framework known as quantum computing.

1.1 Quantum Computing

In classical computers, information is stored and processed as bits, which can take values 0 or 1. On the other hand, the fundamental unit of quantum computation used by quantum computers is a quantum bit (qubit), which can be $|0\rangle$, $|1\rangle$ or in any superposition of being both 0 and 1, $\alpha|0\rangle + \beta|1\rangle$. Qubits in superposition states can lead to quantum interference and entanglement, which are the essential components for speedup associated with quantum computers [NC02]. The speedup we obtain with quantum computers is dependent on the choice of the problem. For instance, Shor's quantum algorithm provides exponential speedup with factoring integers compared to the best known classical algorithm [Sho94], while Grover's quantum algorithm provides only quadratic speedup over the classical case [Gro96].

One of the most prominent application of quantum computer is simulation of quantum systems. The idea of quantum simulation was first proposed by Feynman in 1982 [Fey82]. The fundamental equation that governs the dynamics of a state $|\psi\rangle$ under a Hamiltonian $H(t)$ in quantum mechanics is given by Schrödinger equation

$$i\frac{d}{dt}|\psi\rangle = H(t)|\psi\rangle, \tag{1.1}$$

that has the solution $|\psi(t)\rangle = U(t)|\psi(0)\rangle$ with the propagator formally given by

$$U(t) = \mathcal{T}\left(\int_0^t dt' \exp\left[-iH(t')\right]\right) \tag{1.2}$$

$$= 1 + \sum_{n=1}^{\infty} \frac{(-i)^n}{n!} \int_0^t dt_1 \int_0^t dt_2 ... \int_0^t dt_n \, T\left[H(t_1)H(t_2)...H(t_n)\right] \tag{1.3}$$

where $\mathcal{T}\left(\int_0^t dt' \exp\left[-iH(t')\right]\right)$ is referred to as the time-ordered exponential of the Hamiltonian that is defined by the right hand side of Eq. (1.3). The operation $T\left[H(t_1)H(t_2)...H(t_n)\right]$ produces the time-ordered product of operators, where the factors are arranged in a manner such that the time arguments will decrease from left to right.

Feynman pointed out that simulation of an arbitrary quantum system evolving under Eq. (1.1) is intractable on a classical computer [Llo96]. That is, it requires exponential amount of resources in space and time to keep track of the state as a function of time. For instance, consider a system with N spin-1/2 particles, then the description of the state itself requires parameters that grow exponentially in the number of particles, 2^N. In addition, calculation of the time-evolution requires a number of operations that grow exponentially in the system size ($2^N \times 2^N$). A way to overcome this problem is to simulate quantum mechanical systems with a device whose constituent parts also follow quantum mechanical laws. Note that, on the other hand, for a classical system, the state space increases only linearly with the number of particles in the system.

Quantum simulators have many applications in quantum chemistry [GAN14,

AGDLHG05, BN09], high-energy physics [MMS+16, KDM+18], condensed-matter physics [EWL+21, HQ18] and atomic physics [YN11]. As a specific example of a problem for which quantum simulators could provide real-world advantage is understanding the mechanism of nitrogen fixation (process that converts atmospheric nitrogen to ammonia under ambient conditions) by the enzyme nitrogenase. A key process in the fertilizer production is manufacturing ammonia that is being produced, at present, using Haber-Bosch process, which requires intense pressure and high temperature. In fact, about 3% of the today's world's energy is spent on manufacturing fertilizers. However, the enzyme nitrogenase converts atmospheric nitrogen into ammonia at room temperature and standard pressure using significantly smaller amount of energy compared to industrial process. To better understand the biological nitrogen fixation and take advantage of this process to reduce our energy needs for manufacturing fertilizers, one needs to simulate the active site of nitrogenase with sufficient accuracy. The nitrogenase active site has large number of strongly interacting (correlated) electrons that makes the computation intractable for classical computers with the existing methods [RWS+17]. Likewise, quantum simulation could help us with understanding high-temperature superconductivity that is not described by Fermi-liquid model [ZLI+21].

1.2 Noisy Intermediate Scale Quantum Era

Since Feynman's proposal of quantum simulation, rapid advancements in the field brought us into the current era of Noisy Intermediate-Scale Quantum (NISQ) devices [Pre18]. These devices are large enough such that they would be able to

tackle problems that are intractable for classical computers but also noisy enough that full-fault tolerant error correction cannot be performed [AAB+19, ZWD+20]. One of the main goals associated with these NISQ devices is to perform a computation that is less demanding than required for universal quantum computation, but that can still surpass the capabilities of the present-day classical computers referred to as having quantum advantage. There has been ongoing effort to achieve quantum advantage in the NISQ devices along different avenues such as sampling [AAB+19, ZWD+20], optimization problems [CAB+21, SKS+21] and quantum simulation [EWL+21, SSW+21, ZPH+17, BSK+17, BDN12].

In a recent seminal experiment, Arute et al. have claimed quantum advantage based on sampling from the output distribution of a pseudo-random circuit on a 53 qubit system at Google [AAB+19]. This pseudo-random circuit was obtained by repeated application of random single-qubit operations alternating with a two-qubit gate. They were able to verify that their device indeed sampled from the intended probability distribution, where the sampling from the distribution is classically hard, using linear cross entropy benchmarking fidelity [AAB+19]. Another recent work by Zhong et al. showed quantum advantage using boson sampling based on the theoretical proposal by Aaranson and Arkhipov [ZWD+20, AA11]. Boson sampling involves sampling from the probability distribution of the output modes after photons are allowed to pass through a linear optical network consisting of beam splitters and phase shifters. Due to interference among photons, this process can result in random outcomes from a probability distribution that cannot be efficiently sampled on a classical computer [AA11].

Another application of NISQ-era devices is hybrid quantum-classical optimization such as variational quantum eigensolver (VQE) [PMS+14] and quantum approximate optimization algorithm (QAOA) [FGG14]. In these type of optimizers, a low depth quantum circuit is executed on a quantum computer to prepare a state and the measurement results are passed on to the classical computer. The classical computer then sends instructions back to the quantum computer, based on classical optimization, to prepare a new quantum state using a different set of parameters. This process is then repeated until the associated cost function is minimized for the purpose of solving some optimization problem. When this paradigm is used for solving classical combinatorial problems, it is referred to as QAOA. It is referred to as VQE when applied to finding the low-energy states of a many-body system [Pre18].

One of the strongest contenders for achieving quantum supremacy in NISQ-era devices is the task of quantum simulation. Even though quantum simulation on quantum computers with fault-tolerant error correction in the future will lead to transformative applications, it can also be a very useful application in the NISQ-era devices. We expect a small error in the simulation such as flipping of a single-spin in a large spin system to not affect the macroscopic observables describing the phases of the system as opposed to Shor's algorithm whose advantage depends on finding the exact configuration of the final state [Deu20]. Quantum simulators can solve problems involving many-body systems that cannot be simulated efficiently by numerical methods on a classical computer or the problems that are not amenable to analytic approximation [CZ12]. Such problems include obtaining the phase diagram of high-temperature superconductor [GAN14] or the phase diagram of a dynamical

quantum phase transition [ABC+21, ZPH+17].

There have been many recent studies of equilibrium quantum phase transitions and out-of-equilibrium dynamics on large quantum simulators (> 50 qubits) that have been claimed to be intractable on classical computers [EWL+21, SSW+21, ZPH+17, BSK+17]. However, it is questionable if these phenomena would be hard to simulate classically even in the presence of decoherence resulting from control errors, inhomogeneities or environmental effects. This is because the decoherence would restrict the ability of the system to generate coherence and entanglement, which can be regarded as the reason why the system is intractable on the classical computer in the first place. In general, how errors impact quantum simulation is not very well understood.

1.3 Methods of quantum simulation

Quantum simulation requires the ability to prepare an initial state of interest, then evolve the initial state under the target time-evolution operator and the capability to perform measurements on the final state. Here we will primarily focus on the aspect of producing the targeted time evolution. Quantum simulation can be broadly categorized into two different types: Hamiltonian based simulation (emulation) and gate-based simulation.

1.3.1 Hamiltonian-based Simulation

The Hamiltonian-based simulation, also referred to as emulation, involves realizing the target Hamiltonian or an analogous Hamiltonian, which has one-to-one correspondence with the system of interest, in the lab. Then, by letting the system naturally

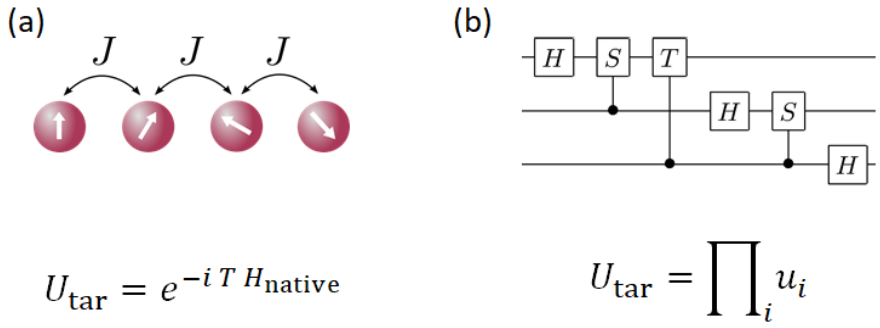

Figure 1.1: The above figure presents different types of the quantum simulation models. **(a)** Emulation: the required time evolution is obtained by letting the system naturally evolve under the native Hamiltonian constructed in the lab. **(b)** Gate-based simulation: the intended time evolution is broken down into a sequence of gates.

evolve with time, one obtains the targeted time evolution as illustrated in Fig 1.1(a). Depending on the experimental platform used for the emulation, some interactions appear naturally and lead to realization of particular type of Hamiltonians. However, as better control of the qubits used in the experimental platform is achieved, wider classes of Hamiltonians can be implemented. The disadvantages of emulators is that they cannot realize arbitrary Hamiltonian and cannot be made fault-tolerant through the existing methods of error correction (see Sec. 1.4).

Consider the experiment using the ion-trap system where the authors claim that they have simulated computationally intractable features associated with non-equilibrium dynamics in a 53-qubit system [ZPH+17]. On this platform, the qubits are encoded in the hyperfine clock states of the $^{171}Yb^{+}$ ion. With the help of an external magnetic field h and spin-dependent forces that arise from an applied laser field, they were able to implement Ising-type Hamiltonian with long-range spin-spin interactions. Typically, problems associated with non-equilibrium dynamics involve evolution over exponential number of excited states accompanied by high entanglement,

which makes it difficult to have a theoretical description. Moreover, the long-range interactions lead to faster growth in entanglement restricting the efficient numerical simulations using matrix product states to short-time dynamics. In the experiment, Zhang et al. obtain information about the various aspects of the non-equilibrium phenomena including long-time average of two-body spin correlations and higher-order correlation observables in these long-range models in a 53 qubit system, which is expected to be hard or impossible to compute classically.

1.3.2 Gate-based Simulation

In the paradigm of gate-based quantum simulation, the time evolution under a given Hamiltonian is realized by breaking down the evolution into a sequence of fundamental unitary maps or "gates", which are assumed to be easier to implement, as shown in Fig 1.1(b). Typically, in this framework, one has access to a "universal gate set", which then allows an arbitrary unitary operation to be efficiently approximated using the gate set as stated by the Solovay-Kitaev theorem [NC02]. A digital simulator of this type with a universal gate set can perform universal quantum computations. Also, when the allowed gates are chosen from a finite set of maps, this simulation can be made fault-tolerant.

One of the first algorithms that was proposed in this framework is the first-order Trotter-Suzuki decomposition of the target unitary [Llo96]. Consider the time-independent Hamiltonian given by

$$H = \sum_{j=1}^{K} H_j \tag{1.4}$$

Suppose the time evolution associated with each of the individual terms in the summation can be implemented using a given gate set $\{e^{-iH_j l}\}$ where l is a constant. Then the time-evolution operator associated with the Hamiltonian of interest can be realized approximately using the first-order Trotter-Suzuki decomposition given by

$$U_{\text{trot}}^{(1)} = \left(e^{-iH_1 \frac{t}{n}} e^{-iH_2 \frac{t}{n}} \ldots e^{-iH_K \frac{t}{n}}\right)^n \equiv (U_\delta(\tau))^n \tag{1.5}$$

$$= e^{-iHt} + \mathcal{O}\left(\frac{K^2 t^2}{n}\right) \tag{1.6}$$

with the Trotter-step size denoted by $\tau = t/n$. In the limit $n \to \infty$, the unitary operator under Trotter decomposition becomes identical to target unitary $U_{\text{tar}} = \exp(-iH_{\text{tar}}t)$. In practice, n is a finite number and leads to an error in the overall simulation according to

$$||U_{\text{trot}}^{(1)} - U_{\text{tar}}|| = \mathcal{O}\left(\frac{\sum_{i,j} ||[H_i, H_j]|| t^2}{n}\right), \tag{1.7}$$

where $n = \mathcal{O}\left(\sum_{i,j} ||[H_i, H_j]|| t^2/\epsilon\right)$ is chosen so that the simulation has an overall accuracy ϵ [CST+21]. For Hamiltonians with local interactions, the number of terms in the target Hamiltonian decomposition given by K in Eq. (1.4) grows polynomially with the system size, allowing efficient simulation of the Hamiltonian through first-order Trotterization [Llo96]. The second-order Trotter decomposition can also be constructed so that error in the lower-order terms cancel as shown below.

$$U_{\text{trot}}^{(2)} = \left(e^{-iH_K \frac{t}{2n}} \ldots e^{-iH_1 \frac{t}{2n}} e^{-iH_1 \frac{t}{2n}} \ldots e^{-iH_K \frac{t}{2n}}\right)^n = e^{-iHt} + \mathcal{O}\left(\frac{K^3 t^3}{n^2}\right) \tag{1.8}$$

Similarly, the high-order Trotter decompositions can be recursively constructed that lead to lower error in the decomposition [CST+21]. All of these Trotter decomposition formulas are collectively referred to as product formulas. Notice that even though higher-order product formulas lead to low error, the length of the circuit required to produce higher-order decomposition increases drastically with the order of the decomposition and may not be practically useful [TLM+19].

More recently, a number of new algorithms such as simulation through truncated Taylor series [BCC+15], quantum signal processing [LC17] and qubitization [LC19] have been proposed that significantly improve the error bounds asymptotically [CMN+18]. These methods are referred to as the post-Trotter methods. Even though many of these post-Trotter algorithms are known theoretically to have better asymptotic performance in time or error precision compared to product formulas, it was shown empirically in some cases that the product formulas perform better than those other methods [CMN+18]. Moreover, product formulas do not need any additional overhead in terms of ancilla qubits making them a relevant choice for quantum simulation in the NISQ era.

1.4 Digital vs. Analog Simulation

Quantum simulators can be also classified into analog and digital simulators. A digital simulator accepts inputs and produces outputs that belong to a discrete state space and implements circuits using a finite set of discrete unitary maps [Deu20]. Even though the qubit state is defined on a continuum described by superposition states, we can consider the input and output state space to be described by the discrete outcomes

of a bit. The finite set of unitary maps are then typically chosen to be a universal gate set in a digital quantum simulator. This discretization allows for quantum error correction using a finite number of error syndrome measurements on digital simulators. Quantum error correction works on the principle of redundantly encoding information using an overhead that scales polynomially, but leads to exponential suppression of errors [NC02]. As a result, the threshold theorem states that provided the error per gate is below some threshold value, a digital quantum computer can then perform an arbitrary quantum computation efficiently even in the presence of noise [NC02].

For an analog simulator, on the other hand, the system's inputs, outputs and the allowed set of unitary operations are all specified on a continuum [Deu20]. Typically, these analog simulators are emulators that are engineered to emulate the dynamics of a quantum system. In addition, there are many simulators that are not strictly digital or analog but rather a hybrid between them. For example, consider the kind of simulator used in [HHZ19], where they simulate the time evolution of the LMG Hamiltonian through approximation of Trotter-Suzuki decomposition, $U_{\text{LMG}} \equiv e^{i(H_1+H_2)T} \approx (e^{iH_1\frac{T}{n}}e^{iH_1\frac{T}{n}})^n$, with access to all the unitaries of the form $\left\{e^{i\tau H_1}, e^{i\tau H_2}\right\}$ with $\tau \in R$. Even though the input and the output in this simulation can be encoded in discrete outcomes of a bit, the allowed unitary transformations are defined on a continuum. These kind of simulators, either analog or hybrid simulators, do not allow for error correction with finite resources, which limits their potential for simulation.

All the NISQ-era devices are fundamentally analog or hybrid simulators that cannot support error correction because they implement continuous time evolution or have

a set of gates that are chosen from a continuum [Deu20], and the noise level is above the threshold needed for fault-tolerant error correction [CTV17]. The absence of error correction in these devices raises the question of whether we can trust the output of these simulators in the presence of noise and imperfections [HCT+12, Deu20, SZZ17]. For instance, some imperfection in the device could lead to propagation of errors in an uncontrolled manner [SOE+19, HHZ19], particularly in the simulation of chaotic systems that are known to be hypersensitive to perturbations [SC93].

In this dissertation, I will present the work performed during my PhD that aims to explore the relationship between how errors accumulate in the simulator and the physical properties of the system. As mentioned before, a key goal for near-term applications of quantum information processing devices is to simulate complex quantum systems, and in particular simulating various aspects of equilibrium quantum phase transitions and non-equilibrium dynamics. In my first project, we have explored the effects of chaos on the quantum simulation of various aspects of the ground-state quantum phase transition and dynamical quantum phase transition present in the Lipkin-Meshkov-Glick (LMG) model. For this, we consider an emulator simulating the LMG model, which is an integrable system, in the presence of an oscillating background field that makes the system chaotic.

In my second project, we study the behavior of errors that arise in the quantum simulation of non-equilibrium phenomena associated with the p-spin models from the approximation of the dynamics via the Trotter-Suzuki decomposition. By mapping the simulated dynamics obtained from the Trotter-Suzuki decomposition to that of a time-dependent periodic Hamiltonian, we have explored the connection between

"structural instability" regions, characterized by multiple bifurcations on the associated classical phase space, and the Trotter errors. In summary, we consider two different physical properties (chaos and structural instabilities), and explore how these properties would affect the reliability of a NISQ-era quantum simulator when simulating various features of equilibrium and non-equilibrium phenomena.

1.5 Outline

The rest of this dissertation is organized as follows. In chapter 2, we provide a brief introduction to the theory of equilibrium phase transitions and describe them using Landau theory illustrated through the classical Ising model. We then introduce the p-spin models, which are fully-connected Ising models. Followed by it, we analyze the thermodynamic limit (mean-field limit/classical limit) of this Hamiltonian to explain the presence of various phase transitions present in these models. The material presented in this chapter provides the knowledge necessary to understand the work presented in Chapters 3 and 4.

Chapter 3 is based on the publication [CPD21]. In this work, we have analyzed the reliability of an analog quantum simulator that is targeted to simulate the ideal Lipkin-Meshkov-Glick (LMG) model, which is integrable in the classical limit, but ends up simulating a perturbed LMG model that is chaotic. We have shown here certain quantities like the time-averaged magnetization, which depend on the local structure of the associated classical phase space, are fragile. However, the quantities like the critical point estimates of the phase transitions, which correspond to changes in the global structure of the phase space, are robust to the perturbations.

Chapter 4 is based on the publication [CMAPD21]. Here, we have identified a new physical mechanism that leads to large errors when the simulation is performed through Trotter-Suzuki decomposition of the time-evolution operator. We have characterized these high-error regions through the use of unitary perturbation theory in the p-spin models. Moreover, we were also able to construct an effective Hamiltonian that describes the Trotter evolution in the high-error regions and therefore helps us understand the origin of these errors.

Lastly, we summarize all of our work in Chapter 5 and suggest potential avenues of research for future work.

2

Equilibrium Phase Transitions and p-spin Models

This chapter provides the necessary background material about equilibrium phase transitions for the work to follow in the upcoming chapters. In the first half of this chapter, we will provide a mean field description of the phase transitions present in the nearest-neighbor classical Ising models followed by a brief discussion of the quantum phase transition present in the quantum Ising model with transverse field. In the later half of the chapter, we introduce the completely connected Ising models, where

each spin interacts with every other spin in the system, and analyze the quantum phase transitions present in these models.

2.1 Classical Phase Transitions

A phase transition can be defined as a qualitative change in the macroscopic properties of the state of the system as a function of some external parameter [NO10]. The point of phase transition is referred to as the critical point and the two types of equilibrium states present on either side of the critical point correspond to two different "phases" of the phase transition. Traditionally, the phase transitions are considered in equilibrium thermodynamics. The equilibrium state of a given system is the state that minimizes the Helmholtz free energy [NO10], which is defined as the Legendre transform of the internal energy:

$$F(T, V) \equiv U(S, V) - TS = -k_B T \log(Z) \tag{2.1}$$

where U is the internal energy, T is the temperature, S is the entropy and Z is the partition function. The change in qualitative properties at the phase transition is then manifested in non analyticity in the free energy of the system as a function of the external parameter. The phase transitions are traditionally categorized into two types depending on the type of singularity. If the first-order derivative of the free energy has a singularity, the phase transition is said to be discontinuous. On the other hand, when the singularity appears in second or higher-order derivatives, the phase transition is said to be continuous. Also, the phase transitions are commonly referred

by the order of the free energy derivative that has singularity. A phase transition is said to be of n^{th} order when the free energy of the system has a singularity in the n^{th} derivative at the point of the phase transition.

One familiar example is the phase transition between ice and water. At low temperatures, the free energy is dominated by the internal energy of the system resulting in ice as the most stable phase. However, as the temperature is increased, the entropy will have more significant contribution resulting in the liquid phase as the more stable state. Suppose one starts with ice and provides heat to the system, then the temperature of the system will increase until the free energy of the solid phase becomes equal to that of the liquid phase. Beyond this point, the two phases coexist and the heat provided will be used by the system solely to convert the solid phase into the liquid phase. This additional energy that is used to convert solid phase to liquid phase is called the latent heat. Once the ice has been fully converted to water, the temperature of the system will increase again as heat is added to the system. These type of systems where the phase of the system changes suddenly as a function of external parameter (temperature in this case) are indicative of a first-order phase transition. These first-order phase transitions involve latent heat and the two phases can coexist simultaneously at the critical point [Gol18].

On the other hand, in the continuous phase transitions, the phase of the system changes continuously from one phase to the another. An example of this kind of phase transition is the ferromagnetic-paramagnetic transition in the magnetic materials. If a magnetic material like iron is heated to high temperatures, it loses it ferromagnetic character continuously and becomes paramagnetic at temperatures higher than the

"Curie temperature". In these materials, the lowest energy state corresponds to the configuration where all the spin states are aligned (either all spins pointing up or down). At low temperatures, this is indeed the equilibrium state, which has ferromagnetic character with a net nonzero magnetization. However, as the temperature is increased, the disordered states minimize the free energy as they correspond to states with large entropy. The resulting equilibrium state at higher temperatures is paramagnetic in nature with zero magnetization.

Phase transitions are typically characterized by an order parameter, a macroscopic property that is zero in one phase (disordered phase) and nonzero in the other phase (ordered phase). In a first-order phase transition, the order parameter realized in the equilibrium state jumps discontinuously from zero to a nonzero value at the critical point, whereas it changes smoothly in a second-order phase transition. Moreover, in the case of continuous phase transitions, various thermodynamic quantities show power-law behavior as a function of reduced temperature ($t = \frac{T-T_c}{T_c}$ where T_c is the critical point of the phase transition) [Car96]. For instance, the correlation length ξ, which is the characteristic length scale associated with the two-point correlation function between constituent particles of the system, diverges as the system passes through a phase transition in the following manner

$$\xi \sim |t|^{-\nu} \tag{2.2}$$

where ν is called the critical exponent. For a more detailed discussion on correlation length and other critical exponents, refer [Gol18]. These critical exponents are have

been found to be independent of the system details, but only depend on the symmetry group of the Hamiltonian, its spatial dimensionality and type of interactions (short-ranged or long-ranged), a phenomenon that is referred to as universality [Gol18].

2.1.1 Ising Model

Consider the classical Ising model with nearest-neighbor interactions described by the following Hamiltonian

$$H = -h \sum_{i=1}^{N} \sigma_i - \gamma \sum_{\langle i,j \rangle} \sigma_i \sigma_j \ , \tag{2.3}$$

where σ_i denotes the spin configuration of the i^{th} classical spin, h and γ are the external magnetic field and the interaction strength respectively. The notation $\sum_{\langle i,j \rangle}$ is used to denote that the summation is performed only over the spins i and j that are nearest neighbors. The spins are placed on a d-dimensional lattice containing N sites. Here σ_i can take two values $+1$ or -1 depending on whether the spin is pointing up or down respectively. The magnetization associated with a particular configuration is then given by $m = \frac{1}{N} \sum_i \sigma_i$. The partition function associated with the Ising model can be written as

$$Z = \sum_{\{s_i\}} e^{-\beta E(\{s_i\})} \tag{2.4}$$

$$Z = \sum_{m} \sum_{\{s_i\}|m} e^{-\beta E(\{s_i\})} \equiv \sum_{m} e^{-\beta F_l(m)} \ , \tag{2.5}$$

where $E(\{s_i\})$ is the energy associated with a spin configuration $\{s_i\}$ and $\beta \equiv \frac{1}{k_B T}$. The summation over all the spin configurations $\{s_i\}$ in the partition function (Eq. (2.4)) has been broken down into two summations (Eq. (2.5)). We first sum over all the spin configurations that result in net magnetization m, denoted by $\{s_i\}|m$, and then sum over all the allowed magnetization values. There are $N+1$ allowed magnetization values that lie in the range $-1 \leq m \leq 1$. Note that we have also defined a new quantity F_l, which will be referred to as Landau free energy, using $\sum_{\{s_i\}|m} e^{-\beta E(\{s_i\})} \equiv e^{-\beta F_l(m)}$. In the large N limit, the allowed values of the magnetization form a continuum, and the partition function can be expressed through the following integral

$$Z = \frac{N}{2} \int_{-1}^{1} dm \; e^{-\beta N f_l(m)} \; . \tag{2.6}$$

where the quantity $f_l(m)$ is the Landau free energy density defined by $f_l(m) \equiv F_l(m)/N$. The dominant contribution to the above integral comes from the minimum value of the integrand $f_l(m_{\min})$ provided N is large (saddle-point approximation). The multiplicative factor here does contain an m dependent term, but it can be ignored in the large N limit. Hence, we have the following expression for the partition function

$$Z \approx e^{-N\beta f_l(m_{min})} \tag{2.7}$$

However, we know from Eq. (2.1) that the partition function can also be expressed in terms of free energy density as $Z = e^{-N\beta f}$. Therefore, we have

$$f = \frac{F}{N} \approx f_l(m_{min}) \tag{2.8}$$

As a result, one can obtain the equilibrium magnetization of the system by minimizing the Landau free energy density $f_l(m)$ with respect to m. The goal is then to obtain Landau energy function. Here, we obtain this function using the mean-field approximation as shown below

$$e^{-\beta F_l(m)} = \sum_{\{s_i\}|m} e^{-\beta E(\{s_i\})} \tag{2.9}$$

$$\approx \Omega(m) e^{-\beta E(m)} \,, \tag{2.10}$$

where $\Omega(m)$ is the number of spin configurations that result in magnetization m and $E(m)$ is the mean-field energy associated with all the configurations that have net magnetization m. The mean-field energy is then obtained by replacing the effect of neighboring spins in the Hamiltonian (Eq. (2.3)) by a mean-field spin m

$$E(m) = -hNm - \frac{q}{2} N\gamma m^2 \,, \tag{2.11}$$

where q denotes the number of nearest-neighbors associated with each spin. The number of nearest neighbors depend on the lattice arrangement and the spatial dimension of the system. For a square lattice in d dimensions, $q = 2d$. The number

of spin configurations that have net magnetization $m = \frac{1}{N}(N_\uparrow - N_\downarrow)$ with $N_\uparrow$ spins pointing up and $N_\downarrow$ ($N_\downarrow = N - N_\uparrow$) spins pointing down is given by

$$\Omega = \frac{N!}{N_\uparrow!\,(N - N_\uparrow)!} \tag{2.12}$$

The function f_l then evaluates to

$$e^{-N\beta f_l(m)} = \sum_{\{s_i\}|m} e^{-\beta E(\{s_i\})} \tag{2.13}$$

$$\approx \Omega(m) e^{N(\beta h m + \frac{q\gamma\beta}{2} m^2)} \tag{2.14}$$

$$f_l(m) \approx -\frac{1}{N\beta}\log(\Omega(m)) - hm - \frac{q\gamma}{2}m^2 \tag{2.15}$$

Using Stirling's approximation, $\log(N!) = N\log(N) - N$, the first term in $f_l(m)$ (Eq. (2.15)) can be written as

$$\frac{\log(\Omega(m))}{N} = \log(2) - \frac{m-1}{2}\log(2) + \frac{m+1}{2}\log(2)\,, \tag{2.16}$$

resulting in

$$f_l(m) \approx -hm - \frac{q\gamma}{2}m^2 - \frac{1}{\beta}\left(\log(2) + \frac{1-m}{2}\log(1-m) - \frac{m+1}{2}\log(m+1)\right) \tag{2.17}$$

The equilibrium magnetization is then obtained by solving $\frac{\partial f_l}{\partial m} = 0$, which leads to

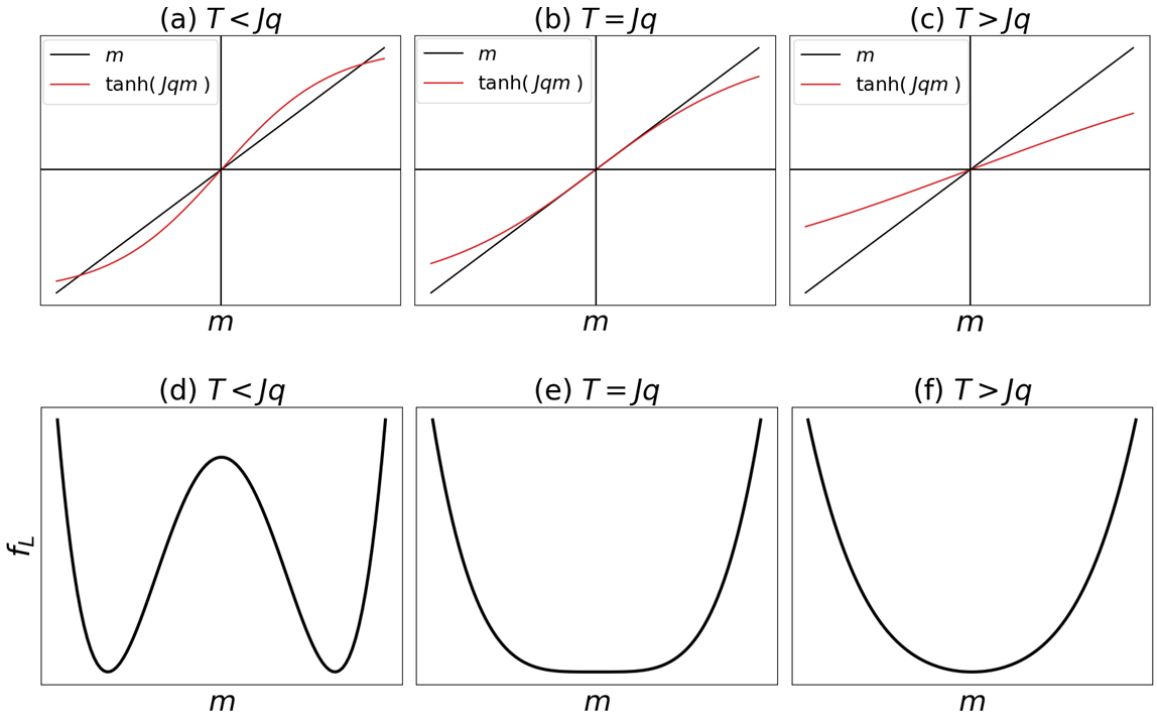

Figure 2.1: (a-c) The solution to the self-consistency equation $m = \tanh(\beta(h + Jqm))$ can be obtained by looking at the intersection of the black and the red-colored curves. As can be seen above, these curves intersect at $m = \pm M$ (equilibrium solutions) and $m = 0$ (corresponds to unstable point) for $T < Jq$ while they intersect only at $m = 0$ (equilibrium solution) for $T > Jq$ indicative of a phase transition at $T = Jq$. **(d-f)** The above figure shows the Landau free energy density ($f_l(m) = \frac{1}{2}(T - Jq)m^2 + \frac{1}{12}Tm^4$) plotted as a function of order parameter m for different values of T. The equilibrium state, which corresponds to point of global minima, changes continuously at the point of phase transitions $T = Jq$.

following self-consistency equation

$$m = \tanh(\beta(h + Jqm)) \tag{2.18}$$

$h = 0$: Second-order phase transition

In the absence of the external magnetic field, the self-consistency equation for the equilibrium magnetization reduces to $m = \tanh(\beta Jqm)$. When $\beta Jq < 1$ or equivalently for $k_B T > Jq$, as shown in Fig. 2.1(c), the self-consistency equation has a

solution $m_0 = 0$, which corresponds to the case where the system has zero equilibrium magnetization. On the other hand, when $\beta Jq > 1$ or $k_B T < Jq$, there are three possible solutions for the equilibrium magnetization given by $m = \pm M$ and $m = 0$ as shown in Fig. 2.1(a). The solution $m = 0$ corresponds to an unstable point and not a point of global minima. Hence, the system has a nonzero equilibrium magnetization given by $m_0 = \pm M$. Therefore, the system prefers a high entropy (disordered) state with zero magnetization at high temperatures and an ordered state with nonzero magnetization at low temperatures resulting in a phase transition. The critical temperature associated with the phase transition is given by $k_B T_c = Jq$. This can be further understood by plotting Landau free energy as a function of temperature. For small values of m, the Landau free energy density in Eq. (2.17) can be Taylor expanded, leading to the following expression

$$f_l(m) \approx \frac{1}{2}(T - Jq)m^2 + \frac{1}{12}Tm^4 \,, \tag{2.19}$$

where the constant term $-k_B T \log(2)$ has been ignored in the above expansion. This free energy density function shown in Eq. (2.19) is plotted in Fig. 2.1 (d-f) as a function of m for different values of the ratio T/Jq. As it can be noted, the function f_l changes from a double well with two global minimas at $m_0 \neq 0$ to a single well with one global minima at $m_0 = 0$ as T/Jq is varied from values smaller than one to large than one. This means that the equilibrium state of the system changes from a configuration that has equilibrium magnetization $m_0 = \pm M$ for $T/Jq < 1$ to a configuration that has magnetization zero for $T/Jq > 1$. The associated equilibrium

states in the ferromagnetic phase ($T/Jq < 1$) correspond to the configurations that have all the spins aligned. Here, the configuration with all the spins pointing up is as equally favorable, as the state with all the spins pointing down because this system is invariant under the spin flips, i.e. $\sigma_i \to -\sigma_i$ for all $i = \{1, ..., N\}$. However, an arbitrarily small symmetry breaking perturbation from the environment will determine the ferromagnetic state that will be realized resulting in "spontaneous symmetry breaking" [NO10].

Notice that the order parameter, which is the equilibrium magnetization, changes continuously from zero to nonzero value as expected for a continuous phase transition. An explicit expression for the order parameter around the critical point of the phase transition can be obtained by minimizing Eq. (2.19)

$$m_0 = \begin{cases} 0 & T > T_c \\ \pm\sqrt{3\left(\frac{T_c - T}{T}\right)} & T < T_c \,, \end{cases} \tag{2.20}$$

The equilibrium magnetization shown above is plotted in Fig 2.3(a). The Landau free energy function can be used further to derive other mean-field critical exponents, which describe the power-law behavior of various quantities around the critical point.

$h \neq 0$: First-order phase transition

Analyzing the self-consistency equation (Eq. (2.18)) in this case, one finds that there is no phase transition present in the model as a function of temperature when the external field is held constant. However, when the magnetic field is varied from

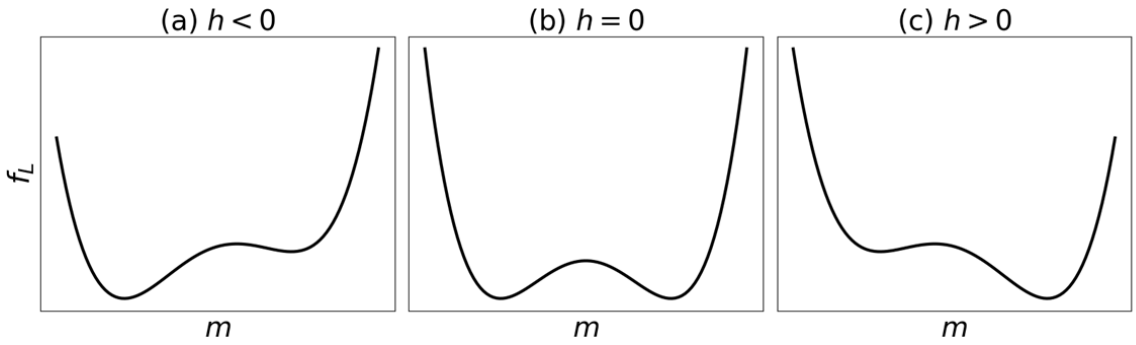

Figure 2.2: The above figure shows the Landau free energy density ($f_l(m) = -mh + \frac{k_B}{2}(T - T_0)m^2 + \frac{k_B}{12}Tm^4$) plotted as a function of order parameter m for (a) negative, (b) zero and (c) positive values of h when $T < T_0$. The equilibrium state, which corresponds to point of global minima, changes discontinuously at $h = 0$ as the external field is varied from negative values to the positive values.

negative to positive values, this model shows a first-order phase transition in the mean-field limit for $T < T_0 \equiv \frac{Jq}{k_B}$, a second-order phase transition for $T = T_0$, and does not have a phase transition for $T > T_0$. We will focus here on the low-temperature $T < T_0$ case. The Landau free energy density obtained from Taylor expanding Eq. (2.17) around $m = 0$ in the presence of external magnetic field is given by

$$f_l(m) \approx -mh + \frac{k_B}{2}(T - T_0)m^2 + \frac{k_B}{12}Tm^4 \,, \tag{2.21}$$

The function f_l in this case has been plotted in Fig. 2.2(a-c) as a function of m as the magnetic field is flipped from the negative values to the positive values. For $h < 0$, the free energy has a global minima with net magnetization at $m_0 = -M$ as shown in Fig. 2.2(a). Moreover, the system also has a metastable state characterized by an additional local minima at some positive value of m. As the magnetic field is changed from negative to positive values, the Landau free energy density associated with the metastable state decreases. At $h = 0$, the energy of the metastable state

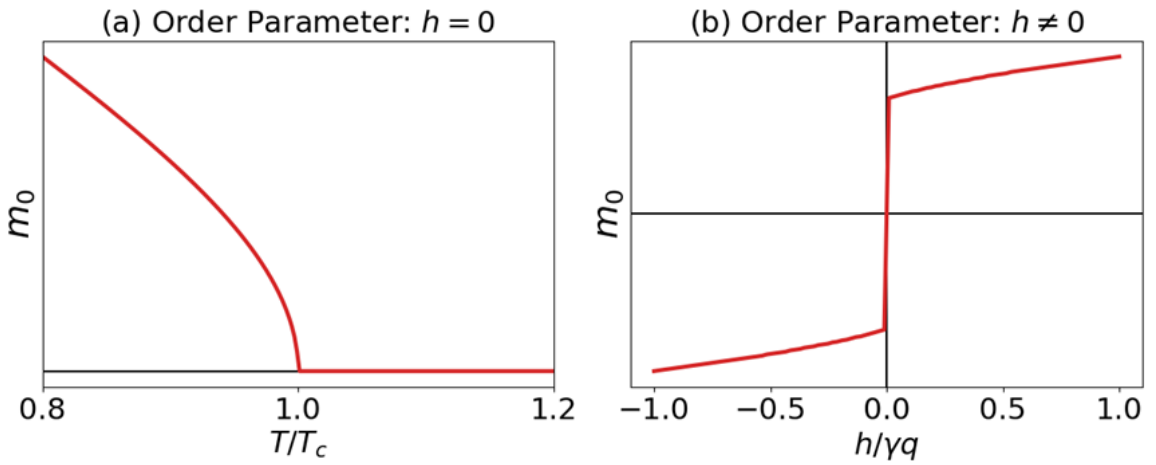

Figure 2.3: The order parameters for the classical Ising model described in Eq. (2.3) are shown above for the $h = 0$ case and $h \neq 0$ case in (a) and (b) respectively. The order parameter changes continuously from nonzero value to zero value in (a), while it changes discontinuously in (b), indicative of continuous and discontinuous phase transitions correspondingly.

becomes equal to that of global minima (see Fig. 2.2(b)). As the magnetic field is further increased, the global minima suddenly jumps from being at negative value of m to positive value of m signifying a first-order phase transition as shown in Fig. 2.2(c). Note that the order parameter in this phase transition jumps discontinuously as expected, shown in Fig. 2.3(b).

Finally, it should be noted that the one-dimensional $d = 1$ Ising model does not have a thermal phase transition even though the mean-field theory predicts it. In fact, the mean-field theory fails completely in one-dimensional Ising model, but it provides correct estimates of critical exponents in higher dimensional systems $d \geq 4$ [Gol18]. This results from the fact that the neglected fluctuations as a result of mean-field approximation in computing the energy associated with various spin configurations play an important role when the dimensionality of the system is reduced. These fluctuations increase the disorder in the system lowering the critical temperature to zero at the lower critical dimension of the system d_l [Car96]. For $d < d_l$, the system

does not have a phase transition. On the other hand, for spatial dimension larger than the "upper critical dimension" d_u, the mean-field theory is exact. This is the case where each spin in the system has a large number of neighbors such that it experiences the mean-field effect. For the nearest-neighbor Ising model, $d_l = 1$ and $d_u = 4$. It should also be mentioned that here we compute $f_l(m)$ using the mean-field approximation. In general, the "Landau theory" postulates the form of Landau free energy density only taking symmetries of the system into account besides assuming that it is an analytic function in m and attempts to explain the universality. Furthermore, the "Landau-Ginzberg theory" then generalizes the Landau theory formalism to inhomogeneous systems where the order parameter is allowed to vary in space.

2.1.2 Quantum Phase Transitions

Quantum phase transitions (QPTs) are the phase transitions that take place at zero temperature, $T = 0$ [Sac11]. At $T = 0$, the free energy and the internal energy of the system are equal (see Eq. (2.1)) indicating that the equilibrium state corresponds to the state with the lowest energy. Similar to the case of classical phase transitions, the QPTs are characterized by singularities in the free energy, which is equivalent to the ground-state energy, as a function of the external parameter. The phase transitions in this case are driven by competing terms in the Hamiltonian whose strengths are changed by varying some external parameter like the magnetic field or pressure. Suppose the external parameter that drives the phase transition is denoted by s, then the energy gap associated with the lowest excited state in the case of continuous quantum

phase transitions vanishes near the critical point s_c in the following manner

$$\Delta \sim |s - s_c|^{z\nu} \tag{2.22}$$

where z and ν are the critical exponents. The critical exponent ν is associated with the divergence in the correlation length of the system around the critical point

$$\xi^{-1} \sim |s - s_c|^{\nu} \tag{2.23}$$

Similar to the case of the classical phase transitions, these critical exponents are universal meaning that they are independent of the microscopic details. Consider the nearest neighbor quantum Ising model with transverse field, which is given by

$$H = -h \sum_i \sigma_i^{(z)} - \gamma \sum_{\langle i,j \rangle} \sigma_i^{(x)} \sigma_j^{(x)} \ , \tag{2.24}$$

where the $\sigma_i^{(\alpha)}$'s are the Pauli operators, h and γ are the strengths of the external magnetic field term and the interaction term respectively. This system describes N spin-1/2 particles interacting with nearest-neighboring spins in the presence of an external magnetic field along the transverse direction. This Hamiltonian is invariant under the parity symmetry $\Pi \equiv e^{i\pi \sum_i \sigma_z^i}$, which rotates all the individual spins by π around the z-axis. Here, we focus on the one-dimensional Ising model. When the external field is zero ($h/\gamma = 0$), the ground state of the system is degenerate and the degenerate states correspond to the configurations in which all the spins are

either pointing up along the x-axis or pointing down along the x-axis, denoted by $|\rightarrow\rightarrow ... \rightarrow\rangle$ and $|\leftarrow\leftarrow ... \leftarrow\rangle$. Therefore, the system is in the ferromagnetic phase. On the other hand, when the external field is very large ($h/\gamma \gg 1$), the ground state is given by the paramagnetic state $|\uparrow\uparrow ... \uparrow\rangle$, where all the spins are pointing up along the field direction. As the ratio of h/γ is varied, the character of the ground-state changes continuously from being paramagnetic ($h/\gamma \gg 1$) to ferromagnetic ($h = 0$) resulting in a second-order QPT at $h/\gamma = 1$. The order parameter associated with the phase transition is given by the longitudinal magnetization denoted by $\langle J_x\rangle \equiv \frac{1}{N}\sum_i \langle\psi_{gs}|\sigma_x^{(i)}|\psi_{gs}\rangle$. As expected, the order parameter is zero in the paramagnetic phase and changes continuously to a nonzero value in the ferromagnetic phase. This can be seen by noting that a paramagnetic ground state will respect the parity symmetry and the longitudinal magnetization is odd under the action of the parity operator. Hence, $\langle\psi_{gs}^{(\text{para})}|\sum_i \sigma_x^{(i)}|\psi_{gs}^{(\text{para})}\rangle = \langle\psi_{gs}^{(\text{para})}|\Pi^\dagger\big(\Pi\sum_i \sigma_x^{(i)}\Pi^\dagger\big)\Pi|\psi_{gs}^{(\text{para})}\rangle = -\langle\psi_{gs}^{(\text{para})}|\sum_i \sigma_x^{(i)}|\psi_{gs}^{(\text{para})}\rangle$ resulting in zero value for the order parameter in this phase. However, spontaneous symmetry breaking favors one of the symmetry broken ferromagnetic states $|\psi_{gs}^{(\text{ferro})}\rangle$, which has a non-zero magnetization.

2.2 p-spin models

In this section, we consider the "p-spin models" where each spin in the previously considered Ising model (Eq. 2.24) interacts with every other spin in the system as opposed to interacting only with the nearest neighbor. Specifically, these models are

described by the following Hamiltonian

$$\begin{aligned} H &= -\frac{h}{2}\sum_{i=1}^{N}\sigma_z^{(i)} - \frac{\gamma}{2pN^{p-1}}\sum_{i_1,i_2,\ldots,i_p=1}^{N}\sigma_x^{(i_1)}\sigma_x^{(i_2)}\ldots\sigma_x^{(i_p)}\ , \\ &= -hJ_z - \frac{\gamma}{pJ^{p-1}}J_x^p\ , \end{aligned} \tag{2.25}$$

where $J_\mu = \frac{1}{2}\sum_{i=1}^{N}\sigma_\mu^{(i)}$ with $\mu = x, y, z$, are the collective spin operators with J being the largest eigenvalue of any of the collective spin operators. These family of models describe N spin-1/2 particles interacting through the p-body coupling along the longitudinal direction with coupling strength (γ) in the presence of an external magnetic field (h) along the transverse direction. The p-spin models have been introduced in the context of spin glasses [Kny16, BFK+13] and have been studied extensively in quantum annealing problems [BS12, ONL18, JKK+10, MNV+17]. Quantum annealing aims to solve optimization problems using adiabatic quantum evolution. This involves adiabatically evolving the ground state of a Hamiltonian, which can be easily obtained, to the ground state a problem Hamiltonian, which encodes the solution to an optimization problem. In the case of p-spin models, the system is initialized in the ground state of the external magnetic field term and the solution, which is encoded in the ground state of the ferromagnetic interaction term, is obtained by slowly decreasing the strength of the magnetic field term while simultaneously increasing the strength of the ferromagnetic term. The hardness of the problem is then determined by the ground-state spectral gap of the Hamiltonian at the intermediate stages, where the Hamiltonian contains both the external field term and the ferromagnetic interaction term. All the p-spin models show GSQPT (ground-state quantum

phase transition) at these intermediary stages, where the spectral gap is smallest, and therefore a bottleneck for adiabatic evolution. In this setting, these family of models have been categorized into two classes based on the type of the GSQPT shown by the model: (a) the $p = 2$ model has a second-order GSQPT, whose ground-state gap closes polynomially with the number of spins in the system at the critical point, (b) all other models with $p > 2$ have a first-order GSQPT, where the ground-state gap closes exponentially with the number of spins in the system [JKK+10].

For the remaining part of the dissertation, we will consider a single-parameter version of the $p-$spin Hamiltonian. To achieve this, we define a dimensionless parameter $s = \gamma/h$ and then normalize the coefficients of the Hamiltonian terms in Eq. (2.25) such that they add to one resulting in the following Hamiltonian

$$H = -(1-s)J_z - \frac{s}{pJ^{p-1}}J_x^p, \tag{2.26}$$

where the parameter s is restricted to be in the range $0 \leq s \leq 1$, interpolating the Hamiltonian between the external magnetic field term and the interaction term. Note that the interaction term has been normalized with an extra factor of p, as it will make the equations of motion have a universal form for all p-spin models in the mean-field limit [MnADJP20]. The p-spin Hamiltonian commutes with the total angular momentum $[H, J^2] = 0$, so the dynamics of the system is constrained to the symmetric subspace if the initial state is chosen in that subspace. The symmetric subspace is spanned by the $2J + 1$ Dicke states, given by $\{|J, J\rangle, |J, J-1\rangle, ..., |J, -J\rangle\}$, that are symmetric under the exchange of any two qubits. This subspace is also spanned by

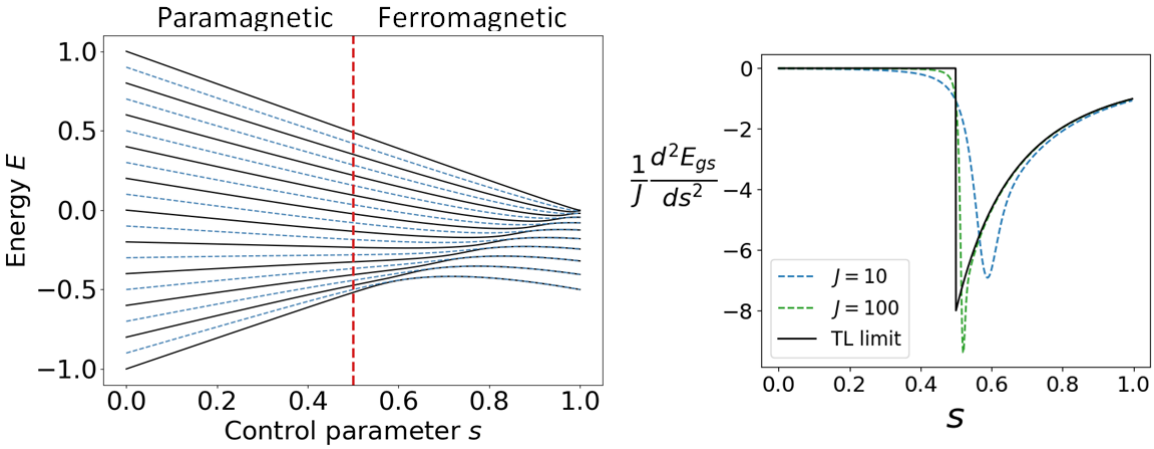

Figure 2.4: (a): The spectrum of the LMG Hamiltonian is shown as a function of the control parameter. The black thick lines label the positive parity eigenstates and the blue dotted lines label the negative parity eigenstates. The red-colored vertical line is drawn at the critical point of the GSQPT. **(b)**: The second derivative of the ground-state energy is plotted as a function of the control parameter for different system sizes. The discontinuity in the second-order derivative can be seen in the thermodynamic limit at the critical point of the GSQPT.

a set of overcomplete spin-coherent states, $\{|\theta, \phi\rangle\}$, which are the states that are polarized along different directions on the generalized Bloch sphere, i.e. $|\theta, \phi\rangle \equiv |\uparrow\rangle^{\otimes N} = e^{-i\theta(J_x \cos\phi - J_y \sin\phi)}|J, J\rangle$. In addition, the p-spin models also have parity symmetry, $[H, e^{i\pi J_z}] = 0$, for even p models. This can be seen from the fact that the interaction term in the Hamiltonian is invariant under π rotation around the z-axis as $(J_x)^p \to (-J_x)^p$ for even values of p.

2.2.1 Equilibrium Quantum Phase Transitions in the p-spin Models

As mentioned before, the p-spin models undergo various quantum phase transitions such as the ground-state quantum phase transitions (GSQPTs), excited state quantum phase transitions (ESQPTs) and the dynamical quantum phase transitions (DQPTs). In this chapter, we will focus on the equilibrium quantum phase transitions present in the p-spin models with emphasis on the $p = 2$ case. The p-spin Hamiltonian in

the $p = 2$ instance reduces to a special form of the well known Lipkin-Meshov-Glick (LMG) model [LMG65, STPB16, CLPHLM06].

$$H = -(1-s)J_z - \frac{s}{2J}J_x^2, \tag{2.27}$$

The LMG Hamiltonian was originally introduced in nuclear physics, but was later studied in many different contexts such as the dynamics of two-mode Bose Einstein condensates for applications of quantum metrology [JDZO$^+$12, SML$^+$14, PSO$^+$18], quantum chaos [TMS$^+$17, MAF$^+$18] and the study of quantum phase transitions [ZPH$^+$17, XSL$^+$20]. The spectrum of the Hamiltonian mentioned in Eq. (2.27) is shown in Fig. 2.4(a), where the positive parity eigenstates are shown by the black-colored thick lines and the negative parity eigenstates are labelled by the blue dashed lines. In the thermodynamic limit, $N \to \infty$, this Hamiltonian undergoes a GSQPT at $s = 1/2$, and the second derivative of ground-state energy with respect to the control parameter, s, has a discontinuity at the critical point of the phase transition as shown in Fig 2.4(b). Therefore, the ground-state character changes continuously from the paramagnetic phase to the ferromagnetic phase as s is increased from 0 to 1. The energy gap between the ground state and the first excited state, which has opposite parity to that of the ground state, becomes zero for all $s > 1/2$ in the thermodynamic limit. As a result of the spontaneous symmetry breaking, the ground-state collapses into one of the degenerate ferromagnetic states. In Fig. 2.4(a), the gap starts to close at $s_c^{(\mathrm{gpt})}(N)$ that is slightly larger 1/2 due to finite-size effects. In fact, this shift in the finite-system size "critical point", $s_c^{(gpt)}(N)$, from the thermodynamic critical

point, $s_c^{(gpt)}$, can be expressed through the following equation

$$\frac{s_c^{(gpt)}(N) - s_c^{(gpt)}}{s_c^{(gpt)}} \propto N^{-\frac{1}{\nu^*}} \tag{2.28}$$

where $\nu^* = 3/2$ is the critical exponent associated with the divergence of the coherence number at the critical point [BJ83, KNG+08, WSH19]. The above equation is derived in Appendix A, and we will discuss more about the finite-size critical point and its scaling later in this chapter. In addition, as mentioned before, the spectral gap at $s = 1/2$ closes polynomially with the number of spins as $\Delta \sim N^{-z}$ where $z = 1/3$ is the dynamical critical exponent [CFS08]. On the other hand, the gap closes exponentially with the number of spins $\Delta \sim e^{-aN}$ for $s > 1/2$ [CFS08]. The order parameter associated with this phase transition is the magnetization along the x-axis $\langle\psi_{gs}|J_x|\psi_{gs}\rangle$, which is zero in the paramagnetic phase and nonzero in the ferromagnetic phase.

Similarly, the models with $p > 2$ also exhibit GSQPTs between the paramagnetic phase and the ferromagnetic phase that correspond to the first-order phase transitions [MnADJP20]

2.2.2 Large N Limit and Mapping to the Double-well Potential

In this subsection, we analyze the p-spin models in the large N limit to explain the presence of equilibrium quantum phase transitions. Notice the similarity between the spectrum of the LMG Hamiltonian and a single-particle system whose potential is changing from a single-well for $s \lesssim 1/2$ to a double well ($s \gtrsim 1/2$), whose barrier depth

is increasing as s is increased further from around 1/2 to 1. This connection can be made rigorous through the semi-classical expansion analysis performed in [JDZO+12]. This analysis was carried out through the use of Schwinger-boson representation for the LMG model, but it can be extended to the all p-spin models in a straightforward manner. The Schwinger-boson representation maps the spin angular momentum algebra to that of two uncoupled harmonic oscillators, referred to as the "plus" type and the "minus type" [SN14]. The Schwinger-boson representation (rotated with respect to the standard representation) is shown below.

$$J_x \to -\frac{1}{2}(a_+^\dagger a_+ - a_-^\dagger a_-) \equiv -\frac{1}{2}(n_+ - n_-) \tag{2.29}$$

$$J_y \to \frac{1}{2i}(a_+^\dagger a_- - a_-^\dagger a_+) \tag{2.30}$$

$$J_z \to \frac{1}{2}(a_+^\dagger a_- + a_-^\dagger a_+) \tag{2.31}$$

The Dicke states $\{|J,m\rangle\}$ in this new representation are denoted by Fock basis $\{|n_+,n_-\rangle\}$ where the number of particles of the plus type, n_+, and the minus type, n_-, is the number of spins pointing up and down respectively. Using this representation, one can rewrite the p-spin Hamiltonian obtained from Eq. (2.26) as follows:

$$H = -\frac{(1-s)}{2}(a_+^\dagger a_- + a_+ a_-^\dagger) - \frac{s(-1)^p}{pJ^{p-1}2^p}(n_+ - n_-)^p \tag{2.32}$$

and an arbitrary state can be written using the Fock basis (harmonic-oscillator basis)

$$|\psi\rangle = \sum_{k=0}^{N} C_k |k, N-k\rangle \tag{2.33}$$

The action of LMG Hamiltonian on an arbitrary state is given by

$$H|\psi\rangle = \sum_{k=0}^{N} -\frac{(1-s)}{2N}\Bigg(c_k\sqrt{k(N-k+1)}|k-1,N-k+1\rangle + c_k\sqrt{(k+1)(N-k)}|k+1,N-k-1\rangle\Bigg) - \frac{(-1)^p s}{2pN^p}(N-2k)^p|k,N-k\rangle\ . \tag{2.34}$$

In the large N limit, the difference in the number of particles between the two modes given by $x = 2\frac{k}{N} - 1$ becomes a continuous variable in the range $-1 \leq x \leq 1$. Defining ψ as a function associated with the coefficients in the Fock basis $\psi(x = 2\frac{k}{N} - 1) = \sqrt{\frac{N}{2}}c_k$ with $h = \frac{1}{N}$, one obtains the following Schrodinger equation

$$\begin{aligned} i\frac{\partial}{\partial t}\langle k,N-k|\psi(t)\rangle &= \langle k,N-k|H|\psi(t)\rangle \\ ih\frac{\partial}{\partial t}\psi(x,t) &= -\frac{(1-s)}{2}\big(\psi(x+2h)b_h(x) + \psi(x-2h)b_h(-x)\big) - \frac{s}{2p}x^p\psi(x)\ , \end{aligned} \tag{2.35}$$

where $b_h(x) = \sqrt{\frac{1-x^2}{4}}\sqrt{1+\frac{2h}{1+x}}$. Expanding the terms on the right hand side of the above equation to $\mathcal{O}(h^2)$, one obtains the following equation

$$\begin{aligned} ih\frac{\partial}{\partial t}\psi(x,t) &= -h^2(1-s)(\frac{\partial}{\partial x}\sqrt{1-x^2}\frac{\partial}{\partial x})\psi(x,t) \\ &\quad - \frac{1}{4}\Bigg(2(1-s)\sqrt{1-x^2} + \frac{2s}{p}x^p + (1-s)\Bigg(\frac{2h}{\sqrt{1-x^2}} - h^2\frac{1+x^2}{(1-x^2)^{3/2}}\Bigg)\Bigg)\psi(x,t). \end{aligned} \tag{2.36}$$

Two important conclusions can be drawn from Eq. (2.36). First, the p-spin models in the large N limit can be mapped to a system with a particle present in a potential

given by

$$V(s,x) = -\frac{1}{4}\left(2(1-s)\sqrt{1-x^2} + \frac{2s}{p}x^p - (1-s)\left(\frac{2h}{\sqrt{1-x^2}} - h^2\frac{1+x^2}{(1-x^2)^{3/2}}\right)\right) \tag{2.37}$$

Second, the energy density (E/N) of the system in the thermodynamic limit expressed in terms of order parameter (x) is given by

$$\mathcal{E} \equiv \frac{E}{N} = -\frac{1}{2}(1-s)\sqrt{1-x^2} - \frac{s}{2p}x^p \tag{2.38}$$

Note the overall energy density could have also been obtained directly in the thermodynamic limit by computing the expectation value of the Hamiltonian in the spin-coherent states and neglecting fluctuations:

$$\frac{\langle\theta,\phi|H|\theta,\phi\rangle}{N} = -\frac{1}{2}(1-s)\cos\theta - \frac{s}{2p}\sin^p\theta \tag{2.39}$$

Then, substituting $x = \frac{\langle J_x\rangle}{J} = \cos\theta$ in the above equation provides us with the energy density given in Eq. (2.38).

In Fig 2.5(a)(iv-vi), the energy density of this system has been plotted for various values of the control parameter with $p = 2$. Note that this energy density transitions from a single well to a double well exactly at the critical point of the GSQPT in accordance with the Landau theory. As a result of this transition from the single well to the double well, the point of global minima changes from $x = 0$, which corresponds to the paramagnetic ground state, for $s < 1/2$ to two other points $x = \pm\, x_0$ that

correspond to the ferromagnetic ground states. The spontaneous symmetry breaking then collapses the state into one of the wells (ferromagnetic states) resulting in non-zero magnetization along the x-axis. As a result, the ground-state magnetization changes continuously from zero to nonzero value at the critical point as expected for continuous phase transitions.

For the case of $p = 4$, the energy density has been plotted in Fig. 2.5(b)(v-viii). In this case, as predicted by the Landau theory, the energy first develops two local minima at $x = \pm\ x_0$ with the global minimum present at $x = 0$ for $s < s_c$ as the value of the control parameter is increased from zero. The value of the control parameter at which these local minima first appear is referred to as the spinodal point, $s = s_{\text{spino}}$. These local minima eventually become global minima, which correspond to the ferromagnetic states, for values of control parameter larger than the critical point, $s > s_c^{(gpt)}$. Notice that in this case, the global minimum suddenly jumps from zero to non-zero value at the critical point as expected from the first-order phase transition.

Also note that the Eq. (2.37) provides us potential well with finite-size corrections. We can use this equation to derive Eq. (2.28), which predicts the way in which critical point of the GSQPT changes as a function of the system size in the LMG model ($p = 2$). The main idea here is to identify the critical point of the GSQPT with the value of s at which the zero-point energy (lowest energy state that is allowed) of the potential equals the barrier height of the double-well. In the classical limit, the zero point energy is the global minima of the potential, and it equals barrier height at $s = 1/2$. However, as $h = \frac{1}{N}$ is increased, the zero-point energy state appears

at values larger than the global minima. As a result, the GSQPT happens at larger values of $s > 1/2$, where the barrier height becomes large enough to become equal to the zero point energy. For more details, refer to Appendix A.

2.2.3 Equations of motion in the mean-field limit (thermodynamic limit or classical limit)

The mean-field limit in the p-spin models is same as the classical limit or the thermodynamic limit [BS12]. The evolution of expectation value of an observable A under a given Hamiltonian H is given by the following equation

$$\frac{d\langle A\rangle}{dt} = i\langle[H, A]\rangle + \langle\frac{\partial A}{\partial t}\rangle \tag{2.40}$$

Substituting different collective spin operators in the above equation for the p-spin models, we have the following equations of motion

$$\begin{aligned}
\frac{d\langle J_x\rangle}{dt} &= (1-s)\langle J_y\rangle \\
\frac{d\langle J_y\rangle}{dt} &= -(1-s)\langle J_x\rangle + \frac{s}{pJ^{p-1}}\sum_{i=1}^{p}\langle\ C_i(J_x^{p-1}J_z)\ \rangle \\
\frac{d\langle J_y\rangle}{dt} &= -\frac{s}{pJ^{p-1}}\sum_{i=1}^{p}\langle\ C_i(J_x^{p-1}J_y)\ \rangle
\end{aligned} \tag{2.41}$$

where $C_i(AB...C)$ produces the i^{th} combinatorial arrangement associated with the product of operators $AB...C$. The mean-field dynamics is then obtained by neglecting the fluctuations $\langle AB\rangle \approx \langle A\rangle\langle B\rangle$ in the Heisenberg equations of motion resulting in the following coupled differential equations for the p-spin models [MCWW97,

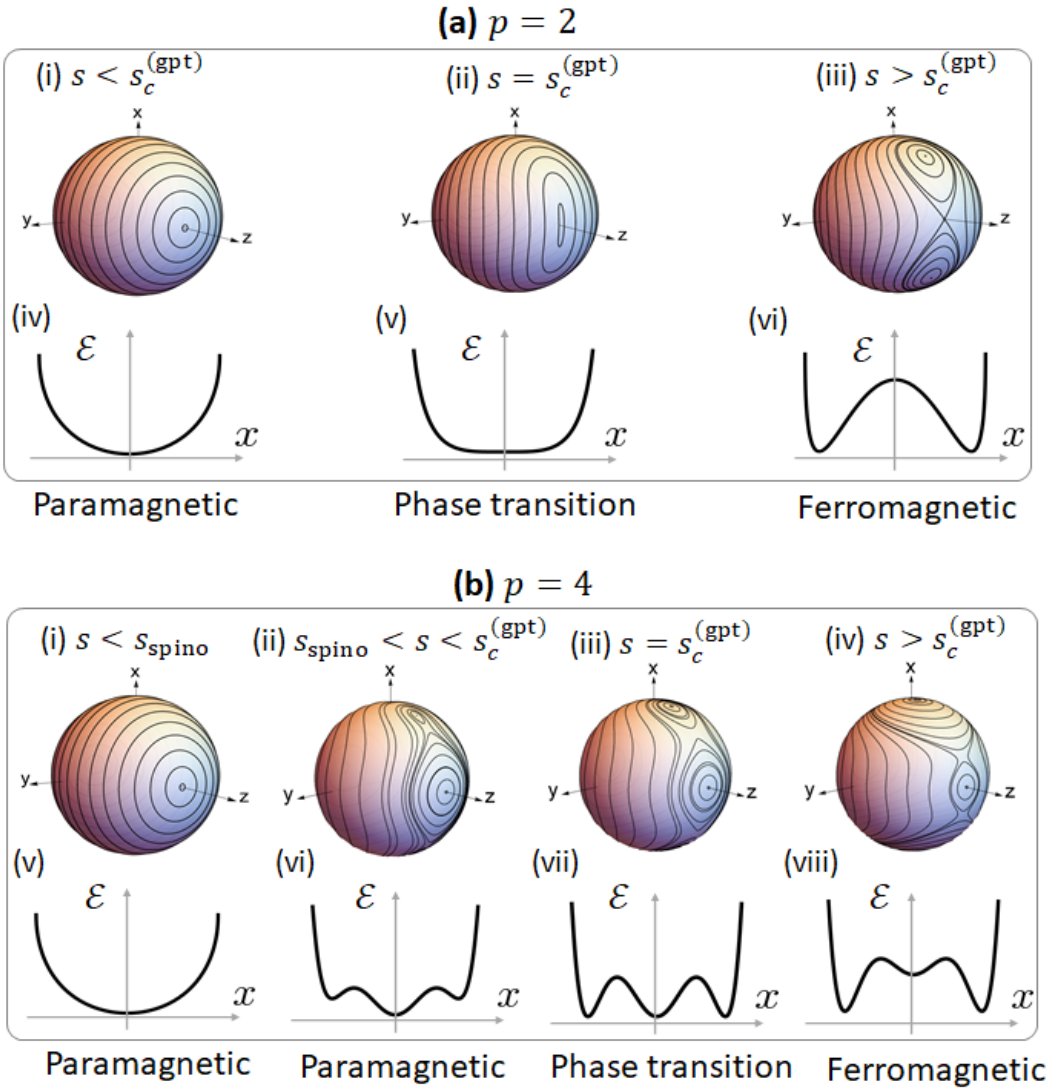

Figure 2.5: **(a)**(i-iii) The phase-space trajectories corresponding to different values of the control parameter for the $p = 2$ case are shown here. The structure of the phase-space trajectories changes at the critical point of the phase transition as a result of pitch-fork bifurcation. **(a)**(iv-vi) The energy density of the LMG model transitions from a single well to a double well at the critical point of the phase transition resulting in a continuous change in the order parameter from zero to non-zero value as predicted by the Landau-Ginzberg theory. **(b)**(i-iv) The phase-space trajectories for the $p = 4$ case are shown here. The structure of the phase-space trajectories changes at $s = s_{\text{spino}}$ of the phase transition as a result of the saddle-node bifurcations. **(b)**(v-viii) The energy density of the $p = 4$ model develops a local minima at $s = s_{\text{spino}}$ that become global minima at the critical point of the phase transition resulting in a discontinuous change in the order parameter at the critical point in accordance with the Landau-Ginzberg theory.

MnADJP20]

$$\begin{aligned}\frac{dX}{dt} &= (1-s)Y,\\ \frac{dY}{dt} &= -(1-s)X + sX^{p-1}Z,\\ \frac{dZ}{dt} &= -sX^{p-1}Y.\end{aligned} \tag{2.42}$$

with $\{X, Y, Z\} = \lim_{J\to\infty} \frac{1}{J}\{\langle J_x\rangle, \langle J_y\rangle, \langle J_z\rangle\}$, describing the motion of a classical "top". Note that the summation terms over the p combinatorial arrangements in Eq. (2.41) such as $\sum_{i=1}^{p}\langle\ C_i(J_x^{p-1}J_z)\ \rangle$ yield the same non-linear term p times in the mean-field limit, $\sum_{i=1}^{p}\langle\ C_i(J_x^{p-1}J_z)\ \rangle = p\langle J_x\rangle^{p-1}\langle J_z\rangle$. This is the reason for normalizing the interaction term with an additional factor of p in Eq. (2.25), as it will ensure that we have universal set of equations for all p-spin models with higher degree of nonlinearity as p is increased without increasing the number of non-linear terms in the equations of motion.

As a consequence of the conservation of angular momentum in the p-spin models, the associated dynamics is constrained to a unit sphere $X^2 + Y^2 + Z^2 = 1$. The fact that mean-field limit matches with the classical limit can be seen from the fact that the equations of motion for the angular momentum obtained using the classical Hamilton's equations ($\dot{q} = \frac{\partial H}{\partial p_i}$ and $\dot{p} = -\frac{\partial H}{\partial q_i}$) will be same as the equations obtained from mean-field limit, shown in Eq. (2.42).

Since the dynamics associated with Eq (2.42) is constrained to a unit sphere, the p-spin models correspond to autonomous systems with one degree of freedom. Therefore,

the p-spin models are integrable in the classical limit. All the essential features of the dynamics in the classical limit can be understood by plotting different trajectories associated with Eq (2.42), which correspond to different initial conditions, for various values of s. These phase-space diagrams are shown in Fig 2.5 (a)(i-iii) and (b)(i-iv) for $p = 2$ and $p = 4$ cases respectively. In the $p = 2$ case, the topology of the phase-space trajectories changes at the $s = 1/2$, which is the critical point of the GSQPT. For values of s smaller than $1/2$, the phase trajectories correspond to precessions around the z-axis with stable fixed points located at $Z = \pm 1$. At $s = 1/2$, the "pitchfork bifurcation" of the stable fixed point located at $Z = 1$ into two other stable fixed points results in two kinds of phase-space trajectories present for $s > \frac{1}{2}$: the ones that precess around the stable fixed points, and the ones that revolve around the whole sphere. These two kinds of trajectories are separated by two homoclinic orbits (trajectories that join the saddle point to itself) referred to as separatrix trajectory, which includes the unstable fixed point located at $Z = 1$. As the value of s is increased from $\frac{1}{2}$ to 1, these stable fixed points move farther away from the unstable fixed point and the separatrix trajectory bounds more trajectories on the phase space.

For $p = 4$ case, the topology of the phase-space trajectories changes at $s = s_{\text{spino}}$ as a consequence of two symmetric "saddle-node bifurcations" resulting in creation of a pair of stable and unstable fixed points at $(\theta, \phi) = (\pm\theta_0, 0)$ where θ and ϕ are the usual spherical coordinates, $\theta = \cos^{-1}(Z)$ and $\phi = \tan^{-1}(Y/X)$. Due to this bifurcation, the system develops three different kinds of trajectories for $s > s_{\text{spino}}$, the ones that precess about $\theta = \pm\theta_0$ bounded by two homoclinic orbits, the ones that precess around $\theta = 0$ bounded by two heteroclinic orbits (trajectories that join two

different saddle points) and the ones that revolve around the whole sphere. As the value of s is increased beyond s_{spino}, the trajectories bounded by the homoclinic orbits increase, while the trajectories bounded by the heteroclinic orbits decrease.

The analysis of p-spin models presented in this chapter will be essential in understanding the work shown in the upcoming chapters. For instance, in the next chapter, the mean-field analysis of phase transitions will guide us in identifying a protocol to probe quantum phase transitions in the LMG Hamiltonian on quantum simulators. Moreover, the understanding of the phase-space trajectories will help us in studying the emergence of chaos in the system when a background perturbation is added to the LMG Hamiltonian. Also, the phase-space trajectory analysis will be an important tool in understanding the results mentioned in Chapter 4. Finally, the mean-field analysis will also be the starting point for the work shown in Appendix C.

3

Effect of Chaos on Quantum Simulation

As mentioned in Chapter 1, all the NISQ-era devices are analog devices because they operate with a set of unitary maps realized on a continuous set. The absence of error correction, as a result of the lack of digitization, may therefore severely limit the reliability of these devices. It is particularly interesting to explore the reliability of quantum simulators in the context of quantum chaotic systems because chaotic systems are characterized by their hypersensitivity to perturbations [Per84, SC93]. In fact, several works have explored the effects of chaos on various aspects of quantum computation in the early 2000s [GS00, SS01, Fla00, Bra02]. For example, in

[SS01], the effect of errors on the simulation of kicked rotor in the chaotic regime has been studied in the presence of imperfections. They found that the resulting errors in certain quantities grew exponentially with the number of qubits. On the other hand, Georgeot *et al.* analyzed the effect of static imperfections such as inter-qubit coupling and fluctuations in the energy spacings of the qubits and showed that the quantum chaos destroys the register states of the system [GS00]. In more recent works, Heyl *et al.* [HHZ19] and Sieberer *et al.* [SOE+19] studied errors in the context of quantum simulation that arise from approximating the time evolution using the first-order Trotter-Suzuki decomposition of integrable Ising-type Hamiltonians. Using this approximation, the time evolution of these Hamiltonians can be realized through the dynamics of a delta-kicked time-dependent Hamiltonians, which become chaotic for certain range of parameter values. It was shown there that the magnetization errors resulting from approximating the time evolution through Trotter decomposition increased sharply whenever the associated kicked Hamiltonians became chaotic [HHZ19, SOE+19]. We will return to the issue of Trotter errors and their relation to the nonlinear dynamics of the system in Chapter 4.

In this chapter, we will consider a situation where a background perturbation makes the quantum simulator weakly chaotic and analyze the reliability of such simulator. Specifically, we will explore the effects of chaos on the quantum simulation of various aspects related to the quantum phase transitions, specifically ground state quantum phase transition (GSQPT) and dynamical quantum phase transition (DQPT), present in the LMG model. This is motivated by the fact that in models where the thermodynamic limit is equivalent to the mean-field limit, such as the collective

spin models studied here, the quantum phase transitions are associated with the behavior of the system in the vicinity of the separatrix trajectory. Interestingly, an integrable system first develops chaos in the vicinity of separatrix trajectory when an integrability-breaking perturbation is added to the system [Rei92]. Therefore, it is natural to question the ability to reliably simulate the quantum phase transitions in the presence of integrability breaking perturbations.

Furthermore, it should be noted that we are interested in exploring the reliability of quantum simulation of the quantum phase transitions on a particular type of quantum simulator that can execute unitary transformation on the state of interest accompanied by measurement and data processing to derive the desired output [ZPH+17, LKP+20]. On this simulator, we assume product states such as the spin-coherent states can be prepared easily with high fidelity and the expectation values of various observables can be obtained followed by evolution of the initial state under a desired unitary operation. We keep this particular framework in mind and propose protocols for extracting the critical points of the GSQPT and the DQPT that only require an ability to access time-averaged expectation values of collective spin observables obtained from the time evolution under the LMG Hamiltonian for particular spin-coherent states.

3.1 Dynamical Quantum Phase Transitions

The LMG Hamiltonian has a dynamical quantum phase transition (DQPT), which characterizes sharp changes in the non-equilibrium behavior of the system under the action of a quenched Hamiltonian, in the thermodynamic limit [ZPH+17, ŽHKS18].

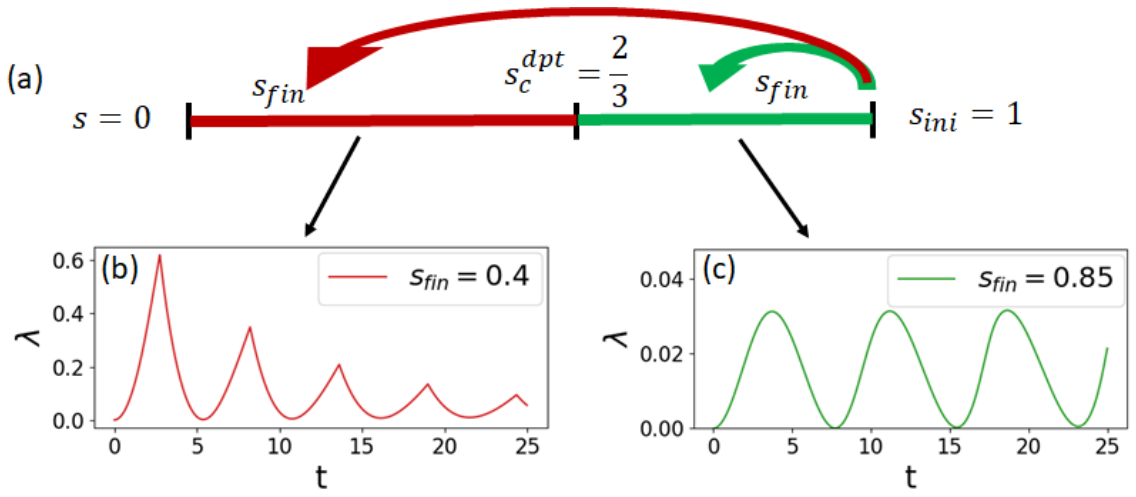

Figure 3.1: (a) This figure shows the DQPT paradigm in the LMG model where the dynamics associated with the ground state at $s_{ini} = 1$ is analyzed under the action of the quenched Hamiltonian. The resulting dynamics has different behavior in different dynamical phases with the critical point located at $s_c^{(dpt)} = 2/3$. **(b-c)** The associated rate function λ has non-analyticities in one dynamical phase (b) and has a smooth behavior in other phase (c) as a function of time.

More specifically, in this paradigm, the system is first initialized in one of the states that corresponds to symmetry-broken ground-states of the Hamiltonian in the thermodynamic limit at some initial value of the control parameter, s_{ini}, and then the dynamics of the state is analyzed as a function of time under the action of the quenched Hamiltonian at some other value of control parameter s_{fin}. The resulting dynamics then has different behavior in different "dynamical phases". A particular quantity of interest, which plays the analogous role of partition function in equilibrium phase transitions in this paradigm [ŽHKS18], is the Loschmidt probability amplitude in the degenerate subspace (subspace associated with the degenerate eigenstates in the thermodynamic limit) given by

$$P(t) = \sum_{i=1}^{K} |\langle \psi_{gs,i}(s_{\text{ini}}) | e^{-H(s_{\text{fin}})t} | \psi_{gs,1}(s_{\text{ini}}) \rangle|^2 \tag{3.1}$$

where $|\psi_{gs,1}(s_{\text{ini}})\rangle$ is one of the symmetry-broken ground states at $s = s_{\text{ini}}$ and the summation is taken over the degenerate ground-state subspace at $s = s_{\text{ini}}$ containing K states. The rate function, which serves the role analogous to free energy density, is given by

$$\lambda(t) = -\frac{1}{N}\log(P(t)) \,, \tag{3.2}$$

where N is the number of spins (or constituent particles, in general) in the system. This rate function is then either a smooth function or has non-analyticities as a function of time, corresponding to different dynamical phases in the thermodynamic limit.

Focusing on the LMG Hamiltonian, the initial value of the control parameter is typically taken to be $s_{\text{ini}} = 1$, and the final value s_{fin} is then varied between zero and one. The symmetry-broken ground states of the LMG Hamiltonian at $s_{\text{ini}} = 1$ are the states with either all the spins either pointing up or down along the x-axis: $|+\rangle \equiv |{\rightarrow}\rangle^{\otimes N}$ and $|-\rangle \equiv |{\leftarrow}\rangle^{\otimes N}$. The dynamical critical point associated with this particular setting ($s_{\text{ini}} = 1$) is at $s_c^{(dpt)} = 2/3$ (see Fig. 3.1(a)). The different dynamical phases present in this Hamiltonian can be understood by analyzing the Loschmidt amplitude, which can be expressed in this case as follows

$$P(t) = |\langle +|e^{-iH(s_{\text{fin}})t}|+\rangle|^2 + |\langle -|e^{-iH(s_{\text{fin}})t}|+\rangle|^2 \tag{3.3}$$

$$\equiv P_+(s_{\text{fin}}, t) + P_-(s_{\text{fin}}, t) \tag{3.4}$$

In the thermodynamic limit (classical limit), $P_{\pm}(s_{\rm fin},t) = e^{-N\lambda_{\pm}(s_{\rm fin},t)}$ where $\lambda_{\pm}(s_{\rm fin},t) = -\log\left(\frac{1\pm\vec{n}(s_{\rm fin},t).\vec{x}}{2}\right)$ since $|\langle n_1|n_2\rangle|^2 = \left(\frac{1+\vec{n_1}.\vec{n_2}}{2}\right)^{2J}$. Therefore,

$$P(t) \approx e^{-N\lambda(s_{\rm fin},t)} \ , \tag{3.5}$$

where $\lambda(s_{\rm fin},t) = \text{minimum}(\lambda_+(\text{s}_{\rm fin},\text{t}),\lambda_-(\text{s}_{\rm fin},\text{t}))$. For values of the control parameter $s_{\rm fin} > 2/3$, as illustrated by the green trajectory in Fig. 3.2(c), the time-evolved state given by $e^{-iH(s_{\rm fin})t}|+\rangle$ will always have a positive projection along the x-axis and therefore $\lambda(t) = \lambda_+(t)$ for all times. Hence, the rate function will be smooth as a function of time as shown in Fig. 3.1(c). On the other hand, for the values of the control parameter $s_{\rm fin} < 2/3$, the time-evolved state, as shown by the green trajectories in Fig. 3.2(a-b), will have a projection along the x-axis that will oscillate between the positive and the negative values resulting in switching the rate function given by $\lambda(s_{\rm fin},t)$ between $\lambda_+(t)$ and $\lambda_-(t)$ for every half-time period of the trajectory. Hence, the effective rate function given by $\text{minimum}\{\lambda_+(\text{s}_{\rm fin},\text{t}),\lambda_-(\text{s}_{\rm fin},\text{t})\}$ will have kinks as a function of time as illustrated in Fig. 3.1(b). The order parameter that identifies this transition between the two dynamical phases is the time-averaged magnetization along the x-axis given by

$$\overline{\langle J_x\rangle} = \lim_{T\to\infty}\frac{1}{T}\int_0^T dt\ \langle J_x\rangle(t). \tag{3.6}$$

The above quantity is zero in one dynamical phase and nonzero in the other dynamical phase. This can be observed from the fact that for $s_{\rm fin} > 2/3$, the trajectory corre-

sponding to the initial state $|+\rangle$ will be constrained to the hemisphere with $x > 0$, bounded by the homoclinic orbit, resulting in non-zero time-averaged magnetization (see green trajectory in Fig. 3.2(c)). On the other hand, for $s_{\text{fin}} < 2/3$, the corresponding trajectory will precess around the whole sphere resulting in zero time-averaged magnetization along the x-axis (see green trajectory in Fig. 3.2(a-b)). Hence, in the LMG Hamiltonian, the trajectories that give rise to different dynamical behavior determining whether the rate function is smooth or non-analytic is also responsible for the zero-nonzero transition in the order parameter. However, it should be noted that, in general, the change in non-equilibrium behavior could be manifested either only in the order parameter or the rate function. In such cases, the DQPT is referred to as DQPT I and DQPT II corresponding to the manifestation in the order parameter and the rate function respectively [SSS20].

3.2 Protocols for the Extraction of Critical Points associated with QPTs

In this section, we discuss the connection between the dynamics of the system in the classical limit and the quantum phase transitions. We then use this analysis to propose protocols for obtaining the critical points of the GSQPT and the DQPT using the time-averaged magnetization both in the case of thermodynamic limit and the finite-sized systems.

3.2.1 Classical Bifurcation

As mentioned in Chapter 2, the classical LMG Hamiltonian undergoes a pitchfork bifurcation (one stable fixed point becomes unstable and bifurcates into two other

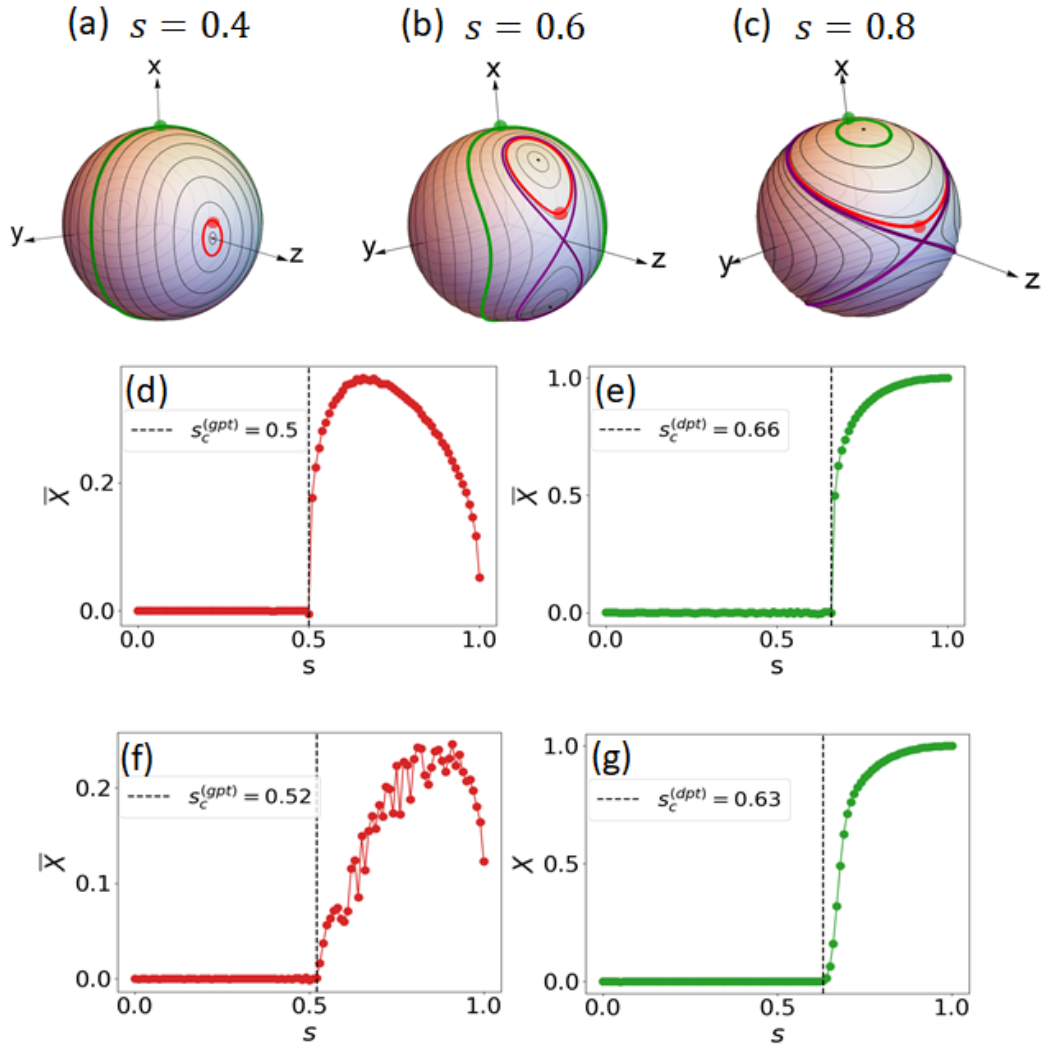

Figure 3.2: (a-c) The red and the green colored curves show the trajectories traced out by the initial conditions used in the GSQPT and DQPT bifurcation protocols. Violet-colored trajectory represents the homoclinic orbits (separatrix trajectory). The GSQPT/DQPT critical point is the value of the control parameter when the associated initial condition is first bounded by the homoclinic orbit. **(d,e)** The time-averaged magnetization as a function of the control parameter for the GSQPT and DQPT initial conditions, represented by the red curve and the green curve, respectively in the classical limit. Note that these bifurcation points coincide with the critical points of the appropriate QPTs. **(f,g)** The time-averaged magnetization obtained using a finite-sized system ($J = 100$) with the initial states being the spin-coherent states centered approximately at the initial conditions used in (d) and (e) (see text for more details).

stable fixed points) at the critical point of the GSQPT resulting in change in the topology of the phase-space trajectories for $s > 1/2$. Suppose, we let a state located slightly off the z-axis at $(\theta_0 = \epsilon_{TL}, \phi_0 = 0)$, where ϵ_{TL} is a small angle, evolve under the LMG Hamiltonian. The state then undergoes very different dynamics in the ferromagnetic phase ($s > 1/2$) (red-colored trajectories in Fig. 3.2(b-c)) compared to the dynamics in the paramagnetic phase ($s < 1/2$) (red-colored trajectory in Fig. 3.2(a)). Hence, the resulting time-averaged magnetization along the x-axis, denoted by $\overline{X} \equiv \frac{1}{T}\int_0^T X(t)dt$ (T is the time period of the trajectory and $X(t)$ is defined by the solution to Eq. (2.41) with $p = 2$), as a function of the control parameter for this initial condition will be zero in the paramagnetic phase and nonzero in the ferromagnetic phase as shown in Fig. 3.2(d). This can be understood by the fact that the trajectory in the paramagnetic phase precesses around the whole sphere resulting in $\overline{X} = 0$, but it is bounded by the homoclinic orbit (separatrix) on the hemisphere $X > 0$ in the ferromagnetic phase resulting in $\overline{X} > 0$. This implies that the time-averaged magnetization can be used as a tool in identifying the critical point of the GSQPT in the thermodynamic limit provided the initial state is located at $(\theta_0 = \epsilon_{TL}, \phi = 0)$ where ϵ is a small angle. Note that the time-averaged magnetization for the initial condition at $(\theta_0 = \pi/2, \phi = 0)$ can be similarly used to detect the critical point of DQPT, as shown in Fig. 3.2(e), because it corresponds to the order parameter of this phase transition. That is, the point $(\theta_0 = \pi/2, \phi = 0)$ corresponds to the ground state of the Hamiltonian at $s = 1$, and the bifurcation diagram constitutes the time-averaged magnetization of this initial condition evolved under the LMG Hamiltonian with different values of the control parameter. For values of $s < 2/3$, the initial

conditions precesses around the whole sphere resulting in $\overline{X} = 0$ (green trajectory in Fig. 2.2(a-b)), and for $s > 2/3$, the initial condition is bounded by the separatrix leading to $\overline{X} \neq 0$ (green trajectory in Fig. 2.2(c)). At the critical point $s = 2/3$, the initial condition is located on the separatrix.

As a consequence of parity symmetry, the time-averaged magnetization of a state initialized at $(\theta_0 = \pi/2, \phi = 0)$ will be negative of the $\overline{X}$ associated with the initial state $(\theta_0 = \pi/2, \phi = \pi)$. Therefore, $\overline{X}$ resulting from both the initial conditions $(\theta_0 = \pi/2, \phi = 0)$ and $(\theta_0 = \pi/2, \phi = \pi)$ plotted in the same figure as a function of the control parameter will have time-averaged magnetization bifurcating at the critical point of the DQPT. This also holds true for the GSQPT initial condition. Hence, we will often refer to these figures as the bifurcation diagrams even though we focus only on the positive branch of $\overline{X}$ to avoid being redundant.

We can also derive an analytic expression for these bifurcation diagrams in the thermodynamic limit ($N \to \infty$). Assuming that we have initial condition of the form $(\theta_0, \phi_0 = 0)$, the following relationship between the angular coordinates of the trajectory, $\theta(t)$ and $\phi(t)$, as a function of time follows from the conservation of energy:

$$\begin{aligned} \frac{1}{J} \langle \theta, \phi | H | \theta, \phi \rangle \big|_{(\theta=\theta_0, \phi=0)} &= \frac{1}{J} \langle \theta, \phi | H | \theta, \phi \rangle \big|_{(\theta=\theta(t), \phi=\phi(t))} \\ \cos^2 \phi(t) &= \frac{2(1-s)(\cos\theta_0 - \cos\theta(t)) + s\sin^2\theta_0}{s\sin^2\theta(t)} \,. \end{aligned} \tag{3.7}$$

The solutions to $\theta(t)$ when $\phi(t) = 0$ are given by

$$\cos\theta(t) = \cos\theta_0 \quad \text{and} \quad \cos\theta(t) = \frac{2(1-s)}{s} - \cos\theta_0 \tag{3.8}$$

The second solution will exist for initial conditions that have their trajectory bounded by the separatrix. Therefore, the bifurcation point in the bifurcation diagram, where the time-averaged magnetization changes from zero to nonzero value, can be identified as the value of control parameter after which the second solution exists, which is given by

$$s_c(\theta_0) = \frac{1}{1+\cos^2\frac{\theta_0}{2}} \tag{3.9}$$

The time-averaged magnetization along the x-axis can be evaluated by averaging $X(t)$ over one time period of the classical trajectory,

$$\overline{X} = \frac{1}{T}\int_0^T dt X(t) = \frac{1}{T}\int_0^T dt \sin\big(\theta(t)\big)\cos\big(\phi(t)\big)\ , \tag{3.10}$$

where $\theta(t)$ and $\phi(t)$ are the spherical coordinates of the associated trajectory. The classical equations of motion associated with the LMG Hamiltonian obtained in Eq. (2.39), expressed in terms of spherical coordinates, are given by

$$\frac{d\theta}{dt} = \frac{s}{2}\sin(\theta)\sin(2\phi) \tag{3.11}$$

$$\frac{d\phi}{dt} = -(1-s) + s\cos(\theta)\cos^2(\phi) \tag{3.12}$$

Using the above equations of motion and Eq. (3.7), the numerator in Eq. (3.10) can be evaluated in a straightforward manner leading to

$$\overline{X} = -\frac{\pi}{sT} \tag{3.13}$$

for all initial conditions of the form $(\theta = \theta_0, \phi = 0)$. The denominator in Eq. (3.13), which is the time period associated with the trajectories, can then be evaluated as follows:

$$T = 2\int_0^{T/2} dt = \frac{2}{s}\int_{\theta_0}^{\theta(T/2)} \frac{d\theta}{\sin(\theta)\cos(\phi)\sin(\phi)} \ , \tag{3.14}$$

$$T = \frac{1}{s}\frac{2i}{\sin\theta_0}\left[F\left(\frac{\pi}{2}\middle|1+\frac{2a}{\sin^2\theta_0}\Delta z\right) - F\left(\sin^{-1}\Big(\frac{1}{\sqrt{1+\frac{2a}{\sin^2\theta_0}\Delta z}}\Big)\middle|1+\frac{2a}{\sin^2\theta_0}\Delta z\right)\right] . \tag{3.15}$$

where F is the incomplete elliptic integral of the first kind. The time-averaged magnetization is then given by

$$\overline{X} = \mp\frac{\pi}{2}\frac{\sin\theta_0}{i\left[F\left(\frac{\pi}{2}\middle|\lambda(\theta_0,s)\right) - F\left(\sin^{-1}\big(\frac{1}{\sqrt{\lambda(\theta_0,s)}}\big)\middle|\lambda(\theta_0,s)\right)\right]} \ , \tag{3.16}$$

where $\lambda = 1 + \frac{4(1-s)}{s\sin^2\theta_0}\big(\cos(\theta_0) - \frac{1-s}{s}\big)$. Note that the above expression in Eq. (3.16) is valid only for initial conditions that have their trajectories bounded by the homoclinic orbit because the limits of the integral were chosen assuming this condition holds true. Using various identities, the above expression can be reexpressed as

$$\overline{X} = \frac{\pi}{2}\frac{\sin\theta_0}{K\big(\Lambda(\theta_0,s)\big)} \ , \tag{3.17}$$

where the function K is the complete elliptic integral of the first kind and $\Lambda(\theta_0, s) = -\frac{4(1-s)}{s\sin^2(\theta_0)}\big(\cos(\theta_0) - \frac{1-s}{s}\big)$. In summary, we have the following expression for the time-

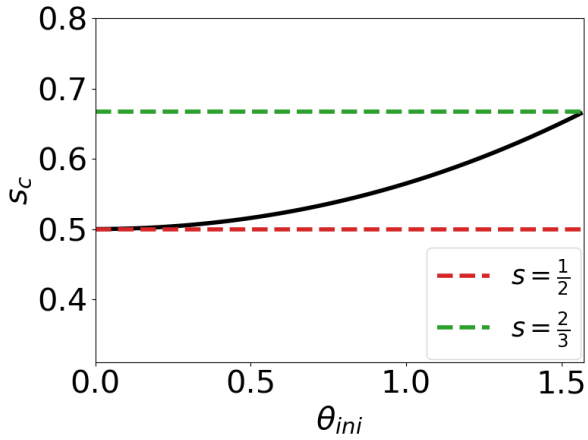

Figure 3.3: The above figure shows the bifurcation point plotted as a function of θ_0. For initial condition close to $\theta_0 = 0$, the bifurcation point is at $s = 1/2$, whereas the bifurcation point is at $s = 2/3$ for $\theta_0 = \pi/2$. Notice that the black curve is flatter at $\theta_0 = 0$ showing that the GSQPT protocol is robust to small variations in θ_0.

averaged magnetization for an initial condition of the form $(\theta_0, \phi_0 = 0)$

$$\overline{X} = \begin{cases} 0 & s < \frac{1}{1+\cos^2\left(\frac{\theta_0}{2}\right)} \\ \frac{\pi}{2}\frac{\sin\theta_0}{K\left(\Lambda(\theta_0,s)\right)} & s \geq \frac{1}{1+\cos^2\left(\frac{\theta_0}{2}\right)} \end{cases} \tag{3.18}$$

The above result provides us information about both the bifurcation points and the bifurcation curves associated with the phase transition. As expected, for $\theta_0 = \epsilon_{TL}$ (GSQPT) and $\theta_0 = \frac{\pi}{2}$ (DQPT), the critical points are given by $(1+\cos^2(\frac{\epsilon_{TL}}{2}))^{-1} \simeq 0.5$ and $(1+\cos^2(\frac{\pi}{4}))^{-1} = \frac{2}{3}$ respectively. In addition, note that the GSQPT bifurcation protocol is robust with respect to variations in the initial value of θ around zero because of the absence of the first-order term in the Taylor expansion of $(1+\cos^2(\frac{\theta}{2}))^{-1}$ around $\theta = 0$. This is illustrated in Fig. (3.3). Finally, notice the above expression for $\overline{X}$ can be shown to change continuously from zero to nonzero value at the bifurcation point for both $\theta_0 \to 0$ (GSQPT) and $\theta = \pi/2$ (DQPT), as expected for continuous

phase transitions.

3.2.2 Quantum Bifurcation

In this subsection, we show that the above-mentioned bifurcation protocols can be adapted to the case of quantum (finite-sized) systems for estimating the finite-size critical points, $s_c(N)$, provided that we start with the spin-coherent states that are centered roughly at the initial conditions used for the classical bifurcation curves. For the case of GSQPT, the initial state $|\psi(0)\rangle$ is a spin-coherent state $|\theta_0, \phi = 0\rangle \equiv |\uparrow\rangle^{\otimes N}_{\theta_0=\epsilon(N),\phi=0}$ centered at a point slightly off the z-axis, $(\theta_0 = \epsilon(N), \phi_0 = 0)$ with $\epsilon(N) = \epsilon_{TL} + \frac{1}{\sqrt{N}}$.Here $\epsilon(N)$ takes the quantum uncertainty of the spin-coherent state into account through the factor $\frac{1}{\sqrt{N}}$, which is the variance of the spin-coherent state. Also, note that $\epsilon(N)$ approaches ϵ_{TL} in the thermodynamic limit. Consider the time-averaged magnetization associated with this initial condition,

$$\overline{\langle J_x \rangle(t)} = \frac{1}{T}\int_0^T \mathrm{dt} \langle\psi(0)|e^{iHt} J_x e^{-iHt}|\psi(0)\rangle \tag{3.19}$$

$$= \sum_{n,m} c_n^* c_m \langle u_n|J_x|u_m\rangle \frac{1}{T}\int_0^T \mathrm{dt}\; e^{i(E_n - E_m)t} \tag{3.20}$$

where the initial state $|\psi(0)\rangle$ in Eq. (3.19) has been expressed in the energy eigenbasis of the LMG Hamiltonian $\{|u_i\rangle\}$ in Eq. (3.20), $|\psi(0)\rangle = \sum_i c_i|u_i\rangle$, and E_i is the energy eigenvalue corresponding to energy eigenstate $|u_i\rangle$. For values of the control parameter s in the paramagnetic phase, the energy eigenstates are non-degenerate. Therefore, the time-averaging over the phases in Eq. (3.20) leads to Kronecker delta function $\delta_{n,m}$ provided the averaging time is much larger compared to the inverse spectral gap

associated with the energy eigenstates in the paramagnetic phase, $T \gg \frac{2\pi}{E_n - E_m}$. The time-averaged magnetization can then be simplified to the following expression in this regime

$$\overline{\langle J_x \rangle(t)} = \sum_n |c_n|^2 \langle u_n | J_x | u_n \rangle \tag{3.21}$$

The above expression is identically zero because the operator J_x is odd under the action of the parity operator ($\Pi = e^{i\pi J_z}$) and the energy eigenstates are the parity eigenstates leading to $\langle u_n | J_x | u_n \rangle = \big(\langle u_n | \Pi^\dagger\big)\big(\Pi J_x \Pi^\dagger\big)\big(\Pi | u_n \rangle\big) = -\langle u_n | J_x | u_n \rangle$. For s values larger than the critical point of the GSQPT, $s > s_c^{(gpt)}(N)$, the energy gap between the ground state and the first excited state, which have opposite parity, is exponentially small in the system size. In the case when the averaging T is small compared to the inverse gap in the ferromagnetic phase, the gap will not be resolved and the energy levels look degenerate, in which case Eq. (3.21) will not be valid leading to nonzero value of the time-averaged magnetization. Hence, using the averaging time T that is larger compared to the typical inverse gap associated with the eigenstates in the paramagnetic phase but smaller compared to the inverse gap in the ferromagnetic phase, which is exponentially large in the system size, produces the expected bifurcation curve as shown in Fig. 3.2(f).

Note that all the above mentioned details related to the choice of initial condition and averaging time can be understood in a straightforward manner when this system is thought in terms of the double-well potential picture, which is valid for even finite-sized systems, introduced in Eq. (2.36). In this picture, the potential transitions from

a single well with minima located at $x = 0$ to a double well with the barrier located at $x = 0$ at the GSQPT critical point. The initial condition chosen in our protocol for the GSQPT is a state that is slightly off the point $x = 0$. Therefore, the time-averaged magnetization associated with this initial condition will be nonzero once the potential transitions to a double-well, as the state is trapped on one side of the double well provided that the averaging time T is smaller compared to the tunnelling time between the wells, which is exponentially large in the system size. On the other hand, we would like T to be large compared to time period of the oscillation, which is inversely proportional to the spectral gap, in the paramagnetic phase, so that the state samples the whole trajectory leading to $\overline{X} = 0$ in this phase.

For the case of the DQPT, the ground state at $s = 1$, which is a spin-coherent state centered at $(\theta = \frac{\pi}{2}, \phi_0 = 0)$, is time-evolved under the action of the LMG Hamiltonian for different values of s to obtain the the bifurcation diagram shown in Fig. 3.2(g). Since the order parameter of the DQPT is being measured in this case, we expect this protocol to give us a correct estimate of the finite-size critical point for all system sizes. This can also be understood based on the double-well picture. At values of the control parameter above the critical point of the DQPT $s > s_c^{(dpt)}$, the initial state corresponding to DQPT will be trapped on one side of the double-well resulting in $\overline{\langle X \rangle} > 0$, whereas the initial state will have energy higher than the barrier height and performs oscillations over both wells of the double well for $s < s_c^{(dpt)}$ leading to $\overline{\langle X \rangle} = 0$.

3.3 Chaos in the Quantum Simulation

A classically integrable system has a number of conserved quantities that are equal to the number of degrees of the freedom associated with the system [Rei92]. The classical LMG Hamiltonian is a system with one degree of freedom that has energy conserved indicating that this system is integrable (see Sec 2.2). The integrability can also seen by the regular periodic trajectories present on the phase space of the Hamiltonian as shown in Fig. 3.2(a-c). The integrability, however, could be broken through an external perturbation that does not respect the symmetries of the system. For instance, the energy of the system is not conserved anymore in the presence of a weak time-dependent perturbation, and therefore the dynamics of the LMG Hamiltonian could potentially become chaotic in the presence of this perturbation. Here, we study the effects of such integrability-breaking perturbation in the context of quantum simulation of various quantities related to GSQPT and DQPT present in the LMG model.

Particularly, we consider a perturbation in the form of a weak-oscillating magnetic field along the y-axis resulting in the following Hamiltonian

$$H = -(1-s)\, J_z - \frac{s}{N} J_x^2 - \varepsilon_0 \cos(\omega t) J_y. \tag{3.22}$$

It was shown that the above Hamiltonian shows chaotic dynamics for a range of values of the perturbation amplitude ε_0, control parameter s and the perturbation frequency ω [MAF+18]. When an integrability-breaking perturbation is added to an

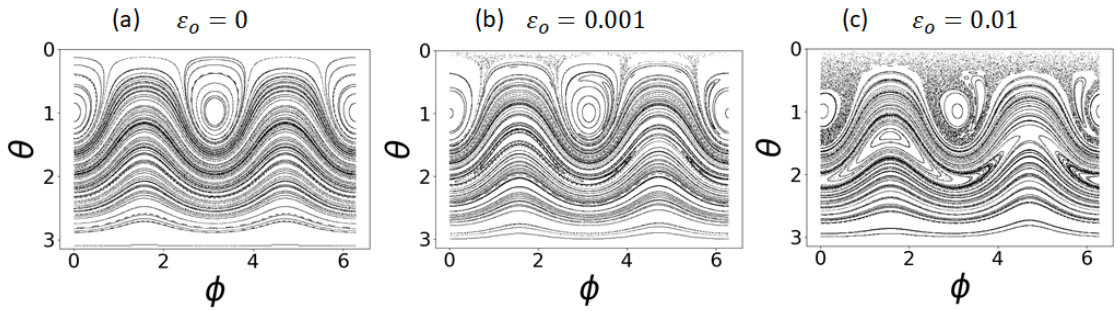

Figure 3.4: The Poincaré sections associated with the LMG Hamiltonian plotted as a function of spherical coordinates for various values of the perturbation amplitudes. Note that chaos originates in the vicinity of the homoclinic orbits through the mechanism of homoclinic tangle.

integrable system, the Kolmogorov–Arnold–Moser (KAM) theorem guarantees that the regular trajectories remain stable and slowly deform into new trajectories provided that they either do not correspond to the resonant orbits or near-resonant orbits [Rei92]. However, for the resonant and near-resonant orbits, it can be shown through the Poincaré-Birkhoff theorem that the system develops chaotic dynamics in the vicinity of these orbits. Therefore, a small integrability-breaking perturbation leads to a mixed phase space containing both integrable and chaotic regions. The primary mechanism underlying the emergence of chaos in the system is the so called "homoclinic (heteroclinic) tangle" that takes place in the vicinity of the homoclinic (heteroclinic) orbit on the classical phase. In the presence of an integrability-breaking perturbation, the stable and the unstable manifolds associated with these orbits intersect transversally at infinite number of points leading to exponential sensitivity of the trajectories near the homoclinic/ heteroclinic orbits [Rei92].

We can characterize the emergence of the chaos in the system through Poincaré sections. Note that the system described in Eq. (3.22) has one and half degree of freedom due to time-dependence in the Hamiltonian leading to phase-space trajecto-

ries in a three-dimensional phase space. This dynamics can then be represented on a two-dimensional plane by identifying the points of intersection of the trajectories in the three dimensions with a plane defined by setting one of the phase-space variables to be constant. These lower-dimensional phase space figures are referred to as Poincaré sections. On these figures, the trajectories in the regular part of the phase space are represented by the closed trajectories and the trajectories corresponding to chaotic sea are identified by the seemingly random points on the phase space.

To obtain a Poincaré section for a time periodic system, it is natural to sample the dynamics of the system every time period given by $\omega T = 2\pi$. The Poincaré sections obtained by sampling at every time period for the system in Eq. (3.22) are shown in Fig. 3.4 for various perturbation amplitudes. In Fig. 3.4(a), the ideal phase space of the LMG Hamiltonian is plotted as a function of the spherical coordinates. This is equivalent to the phase space plotted on the sphere in Fig. 2.5(a)(iii). In Fig. 3.4(b), for a very small perturbation amplitude, it can already be seen that a thin layer of chaos is formed around the separatrix trajectory. As the perturbation strength is increased, the width of the chaotic layer around the separatrix increases as shown in Fig 3.4(c).

A common tool that is used to quantify the strength of the chaos in the system is using the Lyapunov exponents. On the classical phase space, the distance between two neighboring points present in the chaotic region increases exponentially with time, and the exponent associated with this exponential growth is called the Lyapunov exponent. Suppose the two neighboring points in the phase space at time $t = 0$ are given by $\vec{x}_0$ and $\vec{y}_0 = \vec{x}_0 + \Delta\vec{x}_0$, and the displacement between these two vectors

changes in time given by $\Delta\vec{x}(\vec{x}_0, t)$ with the magnitude

$$d(\vec{x}_0, t) = ||\Delta\vec{x}(\vec{x}_0, t)|| \tag{3.23}$$

The exponent associated with the exponential growth is then defined by

$$\lambda(\vec{x}_0, \Delta\vec{x}_0) = \lim_{t\to\infty} \lim_{d(\vec{x}_0,0)\to 0} \frac{1}{t} \log\left(\frac{d(\vec{x}_0, t)}{d(\vec{x}_0, 0)}\right) \tag{3.24}$$

If the phase space is M-dimensional, then there exists a M-dimensional basis given by $\{\vec{e}_i\}$. The Lyapunov exponents along M different directions are then given by $\lambda_i(\vec{x}_0) = \lambda(\vec{x}_0, \vec{e}_i)$. If $\Delta\vec{x}_0$ is arbitrarily chosen, then the Eq. (3.24) will provide us with the largest Lyapunov exponent since the contribution in $\Delta\vec{x}(\vec{x}_0, t)$ will be dominated by the displacement along the largest Lyapunov direction. Moreover, for Hamiltonian flows, it has been shown that $\lambda_i = -\lambda_{M-i+1}$ where $M = 2f$ with f being the degrees of freedom associated with the system [LL13].

The perturbed LMG Hamiltonian is a system with three-dimensional phase space with different directions corresponding to coordinates on the spherical phase space, θ and ϕ, and time. Since it does not make sense to think about the Lyapunov exponent in the time direction, we ignore this exponent, and we effectively have only one other Lyapunov exponent, corresponding to θ and ϕ direction on the phase space in the system, since $\lambda_\theta = -\lambda_\phi$. Using this Lyapunov exponent, we identify the fraction of phase space that shows chaotic dynamics as a function of control parameter and frequency for a fixed perturbation amplitude (see Fig. 3.5). For this,

we compute the Lyapunov exponent associated with 100 different initial conditions chosen uniformly on the sphere and then identify the fraction of initial conditions that have non-zero Lyapunov exponent. The data obtained in Fig. 3.5 is in excellent agreement with the associated Poincare sections. An important observation that follows from this heat map is that the system becomes chaotic only for $s > 1/2$. This is related to the fact that the separatrix trajectory is present on the phase space only for $s > 1/2$ where chaos first emerges through the mechanism of homoclinic tangle [Rei92]. Moreover, we can also observe that the perturbed system does not show chaos for very small or very large values of ω. This is due to the fact that when the perturbation is oscillating at a very high frequency, the ideal system does not have time to respond to the perturbation and experiences the average effect of the perturbation, which is equivalent to turning off the perturbation in this case. On the other hand, in the presence of low-frequency perturbation, the system does not even notice the perturbation for the relevant time scales.

3.4 Sensitivity and robustness to perturbations in the simulation of QPTs

As discussed above, our dynamical quantum simulation protocol identifies the critical points of the phase transition using the motion of the state in the vicinity of the separatrix trajectory (homoclinic orbits), but as we have shown in the previous section, chaos also originates in the neighborhood of the separatrix trajectory in the presence of a small integrability-breaking perturbation. We now analyze the impact of the integrability-breaking perturbation on the simulation of quantum phase transitions in this section.

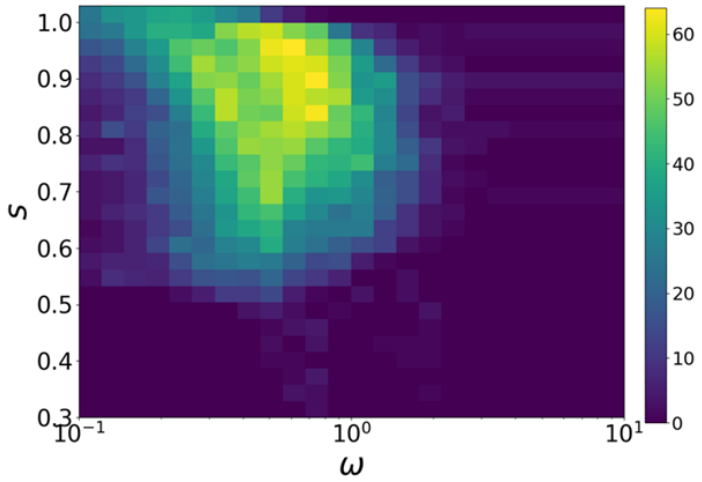

Figure 3.5: The above heat map shows the fraction of phase space that is chaotic for the LMG Hamiltonian in the presence of a perturbation (Eq.(3.22)) as a function of the control parameter and the frequency of the perturbation for a fixed perturbation amplitude, $\varepsilon_0 = 0.05$. The color bar on the right associates different colors with the fraction of phase space that is chaotic.

The bifurcation curves for the GSQPT are shown in Fig. 3.6(a). It should be noted from this figure that the bifurcation diagram obtained in the presence of perturbation, shown by the red-colored curve, is significantly different from the ideal bifurcation curve, shown by the black-colored curve, for $s > s_c^{(gpt)}$. This can be understood by the fact that the initial condition corresponding to GSQPT will be subject to chaotic dynamics only for $s > s_c^{(gpt)}$, as it is located in the vicinity of the separatrix trajectory for these values of the control parameter. This can be seen in the Poincaré sections shown in Fig. 3.6(d-f) where the GSQPT initial condition is labelled by the red dot. We can further support this explanation by noting that the Lyapunov exponent associated with this initial condition as a function of the control parameter is nonzero only for $s > s_c^{(gpt)}$ as shown by the red-colored curve in Fig. 3.6(c). The Lyapunov exponents plotted in this curve have been computed using the method discussed in [RHR98].

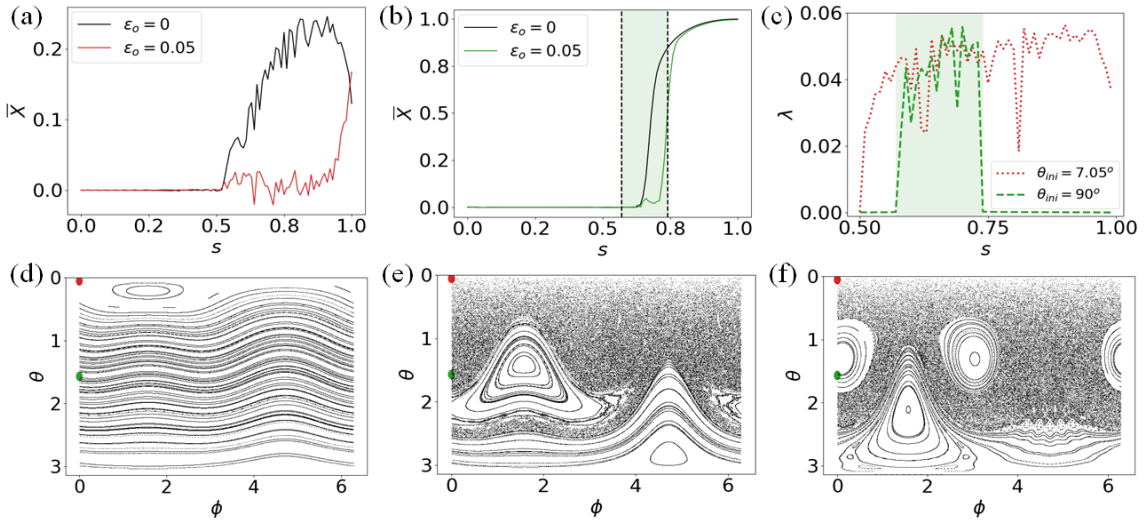

Figure 3.6: **(a-b)** The bifurcation diagrams associated with the GSQPT and the DQPT in the ideal case (black curve) and the perturbed case (red curve for GSQPT and green curve for DQPT) are shown here. It can be seen that the perturbed curve in the GSQPT case has been significantly altered in the presence of perturbation for $s \gtrsim s_c^{(gpt)}(N)$ with respect to the ideal case but only for $s_c^{(dpt)}(N) \lesssim s \lesssim 0.8$ in the DQPT case. **(c)** The Lyapunov exponents associated with the GSQPT and the DQPT initial conditions are plotted as a function of the control parameter as shown by the red and the green colored curves respectively. It can be seen that there is a strong correspondence between the regions of the control parameter where the bifurcation diagrams are appreciably affected by the perturbation and the presence of nonzero Lyapunov exponents. **(d-f)** The Poincarè sections of the LMG Hamiltonian in the presence of the perturbation ($\varepsilon_0 = 0.05$) are plotted as a function of the spherical coordinates of the associated classical phase space for various values of the control parameter, $s = 0.3$ (d), $s = 0.65$ (e) and $s = 0.8$ (f). The red and the green dots show the initial conditions associated with the GSQPT protocol and the DQPT protocol on the phase space.

Similarly, the bifurcation curves associated with DQPT are shown in Fig. 3.6(b), where the ideal and the perturbed bifurcation curves are shown by the black curve and the green curve respectively. Unlike the GSQPT case, the perturbed bifurcation curve in this case is very different from the ideal curve only for intermediate values of the control parameter corresponding to the shaded green region in Fig. 3.6(b). This can again be attributed to the chaos present in the neighborhood of the separatrix trajectory. Recall that, as the value of the control parameter is increased from 1/2 to 1, the homoclinic orbits increase in size bounding trajectories that are farther

away from the unstable fixed point. The DQPT critical point is then the value of s where the initial condition corresponding to DQPT is bounded by the homoclinic orbit. This means that the initial state will be in the neighborhood of separatrix trajectory (and in the chaotic region) only for these intermediate values of s around the DQPT critical point as illustrated by the green dot in the Poincare sections shown in Fig. 3.6(d-f). This is corroborated by noting the Lyapunov exponent for this initial condition is nonzero for the values of the control parameter that correspond to this intermediate region as shown in Fig. 3.6(c). Moreover, it should be noted that since the depth of the associated double well potential increases with the control parameter, the perturbation does not impact the wells for larger values of s, which can be seen by the intact wells present in Fig. 3.6(f). Hence, the DQPT bifurcation diagram becomes resilient to perturbations for larger values of the control parameter.

All the above analysis has been performed by fixing the perturbation amplitude to $\varepsilon_0 = 0.05$, but these results hold true for any perturbation amplitude. That is, the error in time-averaged magnetization associated with the GSQPT and the DQPT protocols is large whenever the corresponding initial conditions are in the vicinity of the separatrix trajectory, which happens for the values of s around the respective critical points of the quantum phase transitions as shown in Fig. 3.7(a-b). Hence, the emergence of chaos in the system makes the system very sensitive to perturbations around the critical regions.

However, there are many quantities that one might be interested in extracting from a quantum simulation. So far, we have focused on the time-averaged magnetizations associated with different initial conditions. Instead, one might be interested

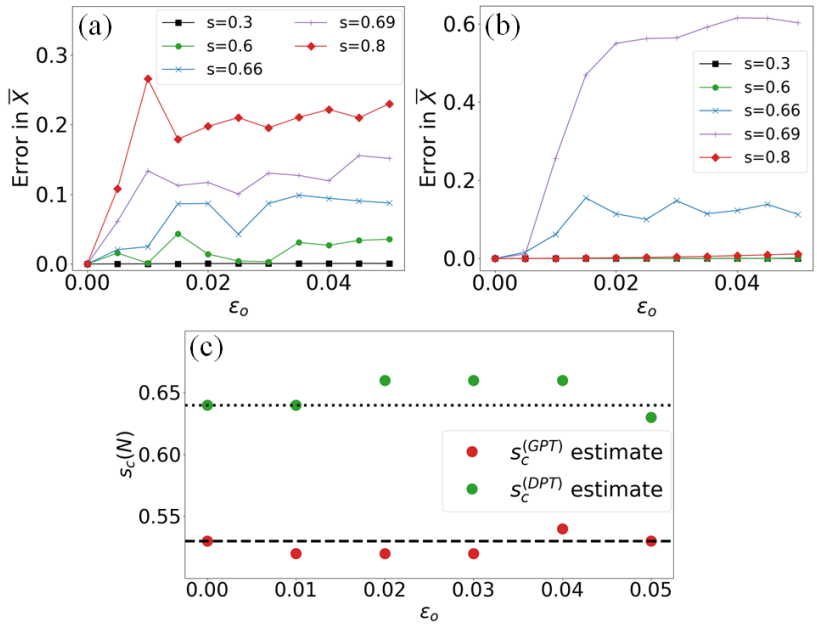

Figure 3.7: (a-b) The error in time-averaged magnetization for the GSQPT (a) and DQPT (b) protocols as function of perturbation amplitude is plotted for various values of the control parameter. **(c)** The critical point estimates associated with the GSQPT and the DQPT are plotted as a function of the perturbation amplitude. Here the critical points are identified as the points where the time-averaged magnetization changes from zero to nonzero. Numerically, the nonzero magnetization is assumed to be a number greater than δ given by $\delta = \sin\left(\varepsilon/\sqrt{2J}\right)$ where $\varepsilon = 0.125$ and $J = 100$. It can be seen that these estimates in the presence of perturbation are close to the ideal values labelled by the dashed (DQPT) and the dotted (GSQPT) lines.

in extracting the critical point associated with the quantum phase transition. This is achieved by using the data from the bifurcation diagram and identifying the value of the control parameter where the time-averaged magnetization becomes larger than a small threshold value, $\overline{X}_{\rm th} \ll 1$. The critical point estimates obtained in this manner are shown in Fig. 3.7(c) for the GSQPT labelled by the red dots and the DQPT labelled by the green dots for various values of the perturbation amplitude. As can be seen in the figure, the critical point estimates in the presence of perturbation are very close to the ideal values marked by the dashed and the dotted line for the GSQPT and the DQPT respectively even though the corresponding bifurcation curves undergo a

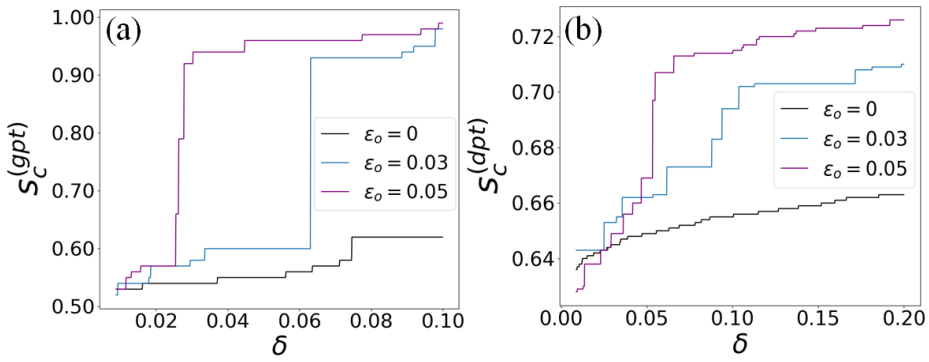

Figure 3.8: The critical point estimates as a function of the threshold parameter δ for the GSQPT (a) and the DQPT (b) protocols are shown here. It should be noted that, in the presence of the perturbation, the critical-point estimates become sensitive to the value of the threshold used in identifying the critical points.

drastic change in the presence of perturbation. This can be ascribed to the fact that the system undergoes global changes on the phase space both in the absence and the presence of the perturbation leading to changes in the time-averaged magnetization from zero to nonzero at the ideal critical points. In the ideal case, these changes happen due to the bifurcation of the fixed point, and in the presence of perturbation, the system's dynamics change from regular to chaotic for $s \gtrsim s_c$.

Even though the critical point estimates are robust with respect to the perturbation, these estimates indeed become sensitive to the exact value of the threshold $\delta = \sin(\frac{\varepsilon}{\sqrt{2J}})$ used in determining the critical points. Here the threshold value $\overline{X}_{th}$ is represented in terms of the average magnetization $(\langle J_x \rangle / J)$ associated with a spin-coherent state located at a polar angle $\frac{\varepsilon}{\sqrt{2J}}$. In Fig. 3.8(a) and 3.8(b), the critical point estimates as a function of the threshold value are plotted for GSQPT and the DQPT respectively for various values of the perturbation amplitude. It can be noted from these figures that the curves associated with the critical point estimates in the presence of perturbation, shown by the blue and the magenta colored curves, increase

sharply with threshold as opposed to the estimates in the ideal case (shown by the black-colored curves), especially for the GSQPT. This might become particularly relevant in the experiments where the critical point estimates could become sensitive to perturbations due to lack of resolution in the time-averaged magnetization.

4

Trotter Errors from Structural Instabilities

4.1 Introduction

Recall that the first order Trotter-Suzuki decomposition allows the simulation of time evolution of a Hamiltonian of the form $H = \sum_{j=1}^{K} H_j$ provided that we have access to time evolution generated by each of the individual terms in the Hamiltonian (see Sec. 1.3). In this chapter, we will focus on the simple case of $H = H_1 + H_2$. Then the time evolution under Trotter decomposition U_{trot} is obtained by the repeated applications of the unitary map given by $U_\delta(\tau) \equiv e^{-iH_1\tau}e^{-iH_2\tau}$ $\left(U_{\text{trot}} = (U_\delta(\tau))^n\right)$, where τ is referred to as the Trotter-step size. The error in each Trotter step can

then be obtained explicitly in a straightforward manner (as shown in [CST+21]) since $U_\delta(\tau)$ follows the differential equation

$$\frac{dU_\delta}{d\tau} = -iHU_\delta + i[H_2, e^{-iH_1\tau}]e^{-iH_2\tau} \ , \tag{4.1}$$

whose solution can be expressed as follows

$$U_\delta(\tau) = e^{-iH\tau} + i\int_0^\tau d\tau' \ e^{-i(\tau-\tau')H}[H_2, e^{-i\tau' H_1}]e^{-i\tau' H_2} \ . \tag{4.2}$$

The above expression can be used for computing the error bound over one Trotter step, which is given by

$$||U_\delta(\tau) - e^{-iH\tau}|| \leq \frac{\tau^2}{2}||[H_1, H_2]|| \ , \tag{4.3}$$

where $||.||$ refers to the spectral norm. Over the entire time evolution T consisting of n Trotter steps ($T = n\tau$), we have

$$||(U_\delta(\tau))^n - e^{-iTH}|| \leq n||U_\delta(\tau) - e^{-i\tau H}|| = \frac{T^2}{2n}||[H_1, H_2]|| \ . \tag{4.4}$$

The above error bound shows that the error in simulation (also known as Trotter errors) that arise from the difference between U_{trot} and the intended time evolution U_{tar} can be made as small as possible by increasing the number of Trotter steps accordingly [Llo96, CST+21]. The error bound also shows how the efficiency of this Trotter-Suzuki algorithm for simulation changes based on the commutator between

the terms involved in the decomposition of the Hamiltonian.

Consider the simulation of the p-spin Hamiltonian $H(s) = -(1-s)J_z - \frac{s}{pJ^{p-1}}J_x^p$ using Trotter decomposition. The ideal target evolution that one wants to implement on the simulator to obtain some quantity of interest, say time-averaged magnetization, is given by

$$U_{\text{tar}} = e^{i\left((1-s)J_z + \frac{s}{pJ^{p-1}}J_x^p\right)n\tau} \,, \tag{4.5}$$

and the unitary map that is obtained under the Trotter-Suzuki decomposition is shown below,

$$U_{\text{trot}} = \left(e^{i(1-s)\tau J_z} e^{i\frac{s\tau}{pJ^{p-1}}J_x^p}\right)^n \equiv \left(U_\delta(\tau)\right)^n \,, \tag{4.6}$$

where we refer to U_{trot} in the above equation as the Trotterized unitary.

The time evolution associated with one Trotter step size τ of the Trotterized unitary can be seen as being generated from the time evolution of a time-dependent Hamiltonian shown below

$$H_\delta(\tau) = -(1-s)J_z - \frac{s\tau}{pJ^{p-1}} \sum_{n=-\infty}^{\infty} \delta(t - n\tau) J_x^p \,, \tag{4.7}$$

where the above sum over n is taken over all the integers. We refer to this class of delta-kicked Hamiltonians as the kicked p-spin Hamiltonians [HKS87, MAPD21]. The Hamiltonian in Eq. (4.7) for $p = 2$ is referred to as the quantum kicked-top (QKT) [HKS87]. The Trotterized unitary can then be seen as repeated application

of the Floquet operator (time evolution operator for one time period of a periodic Hamiltonian) $U_\delta(\tau)$ associated with the above kicked Hamiltonian. It should be noted that even though the target evolution (Eq. (4.5)) is generated by a time-independent Hamiltonian, which is integrable in the classical limit, the Trotterized evolution (Eq. (4.6)), generated by the kicked p-spin models, can be potentially chaotic in the classical limit as the energy of the system is no longer conserved. That is, the number of degrees of freedom in the kicked top models is more than the number of conserved quantities, which allows the possibility of kicked p-spin models to be chaotic [HKS87, MAPD21].

Recently, Sieberer *et al.* have analyzed the behavior of Trotter errors in certain local observables in a closely related version of the $p = 2$ Hamiltonian considered here [SOE+19]. They found that the dynamics of the target Hamiltonian can be accurately simulated for small Trotter step sizes. However, they also showed that the Trotter errors in observables increase sharply for the Trotter-step sizes that make the dynamics of the underlying kicked models chaotic. This nontrivial transition in the behavior of Trotter errors, whose origin can be traced to difference between the target unitary and the Trotterized unitary, cannot be identified by the worst-case error bounds such as Eq. (4.4) as the error bounds are loose. In the regular region, the error in quantum simulation of certain expectation values can be much better than one might expect from the worst-case scenario [SOE+19]. This shows that the physical properties of the system being simulated play an important role in determining the behavior of simulation errors. It is thus desirable to identify whether other physical mechanisms, beyond the regularity-to-chaos crossover, could lead to such behavior.

On the classical phase space, a quasiprobability distribution like the Husimi function ($|\langle\theta,\phi|\psi\rangle|^2$) associated with the eigenstates of the unitary operator will overlap with the corresponding classical trajectories of the unitary operator. This means that the regions of large Trotter errors resulting from classical trajectories of the target unitary being very different from those of the Trotterized unitary will be manifested in the quantum regime as regions where eigenstates of the target unitary and the Trotterized unitary are very different. Therefore, a way to recognize the high Trotter error regions is to compute the inverse participation ratio (IPR) of the Floquet eigenstates of U_δ $\left(\text{eigenstates of } U_\delta \text{ are same as the eigenstates of } U_{\text{trot}} = \left(U_\delta\right)^n\right)$ in the eigenbasis of U_{tar}. The IPR of a given state $|\psi\rangle$ in a particular basis $\left\{|\phi_i\rangle\right\}$ is defined as

$$\text{IPR} = \sum_{\text{i}=1}^{\text{d}} |\langle\phi_{\text{i}}|\psi\rangle|^4 \,, \tag{4.8}$$

where d is the dimension of the Hilbert space. The above quantity ranges between $1/d$ for a fully delocalized state (state with equal superposition of all the basis states) in the basis and one for a fully localized state (state equal to one of the basis states). Moreover, one can define average IPR of one basis in other basis as $\overline{\text{IPR}} \equiv \frac{1}{d}\sum_{i,j=1}^{d} |\langle\phi_i|\psi_j\rangle|^4$. Using average IPR, we define a quantity, referred to as average dissimilarity, which is given by

$$\text{D}(\text{U}_{\text{tar}}, \text{U}_\delta) = \frac{1 - \overline{\text{IPR}}}{1 - \overline{\text{IPR}}_{\text{COE}}}, \tag{4.9}$$

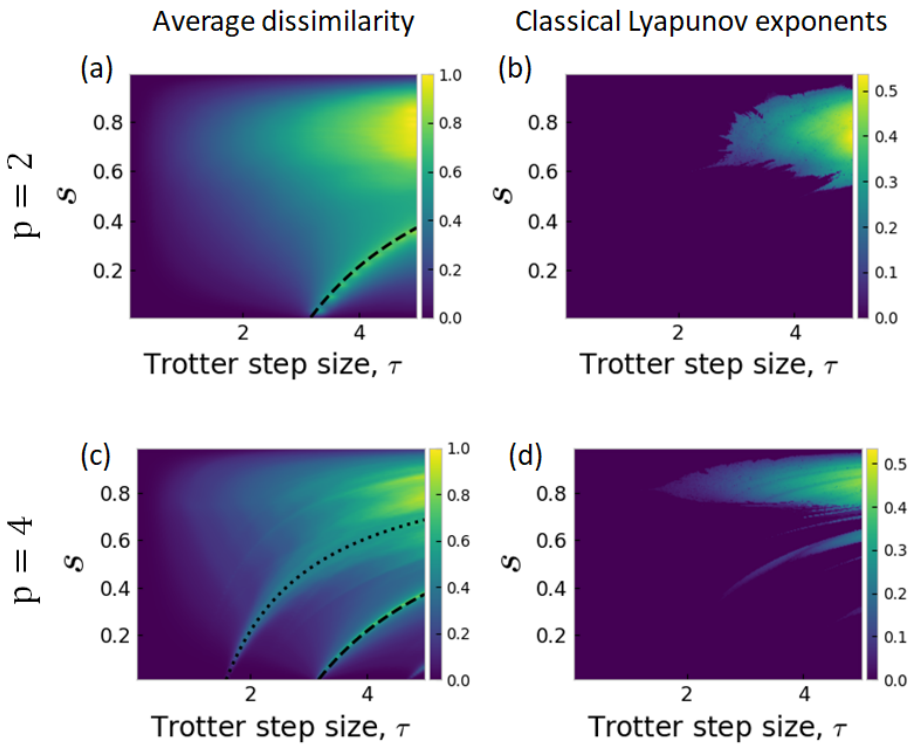

Figure 4.1: (a,c): The average dissimilarity of the Floquet eigenstates in the target Hamiltonian eigenstates is plotted as a function of the control parameter and the Trotter step size for $p = 2$ and $p = 4$ respectively, and $J = 64$ ($N = 128$). The large dissimilarity is shown by the green-colored regions on the heat maps. The black-colored dashed and dotted lines correspond to the curves $\frac{\pi}{1-s}$ and $\frac{\pi}{2(1-s)}$. **(b,d)**: The global Lyapunov exponents obtained from the classical dynamics of the kicked p-spin models with $p = 2$ and $p = 4$ are shown here.

where $\overline{\text{IPR}}_{\text{COE}}$ is the average IPR associated with circular orthogonal ensemble (COE), whose predictions match with the fully chaotic kicked p-spin models [MAPD21, Haa91]. Up to normalization, the dissimilarity ranges between 0 for identical basis sets and $1 - \frac{1}{d}$ for very dissimilar basis sets.

In Fig. 4.1(a), the average dissimilarity between the eigenbasis of U_{tar} and U_δ is plotted as a function of the Trotter step size and the control parameter for the $p = 2$ case. The unitaries U_{tar} and U_δ generate the dynamics associated with the LMG model and the QKT respectively. Note that in Fig. 4.2(a), there are two parameter regions where the dissimilarity between the two eigenbasis sets is high (green-colored

regions). For values of $s \gtrsim 0.5$, the large dissimilarity region can be attributed to the presence of chaotic dynamics in the kicked model as shown in Fig 4.1(b), where the classical global Lyapunov exponents are plotted as a function of the Trotter step size and the control parameter. On the other hand, for values of $s \lesssim 0.5$, the QKT model does not show chaotic dynamics, and therefore the large dissimilarity present around the black dashed line in Fig. 4.1(a) arises from a different physical mechanism present in the kicked model. Later in this chapter, we will see that these dissimilarity regions give rise to large errors in various observables.

Moreover, repeating this analysis for the $p = 4$ Hamiltonian, one finds that the underlying kicked model also show chaotic dynamics for large values of the control parameter (see Fig. 4.1(d)), which then explains the presence of large dissimilarity region for these values of the control parameter shown in Fig. 4.1(c). However, in this case, there are also two additional regions of large dissimilarity (green-colored regions around black dashed and dotted lines in Fig. 4.1(c)), as opposed to one region for $p = 2$, and for small values of the control parameter where the associated kicked model does not show chaotic dynamics. In the next section, we will explore the physical mechanism behind these large dissimilarity regions, which is not related to the chaotic dynamics in contrast to the work of [SOE+19]. We characterize the dissimilar regions through the use of unitary perturbation theory and use this to explain the large simulation errors in these regions.

4.2 Structural instability regions

In order to understand the dissimilarity regions that cannot be attributed to chaos, we will now analyze the eigenstates of the Trotterized unitary associated with the p-spin models using unitary perturbation theory [Per06]. For this, we focus on the region with small values of the control parameter. The target unitary for the p-spin models is given by $U_{\text{tar}} = e^{i\left((1-s)J_z + \frac{s}{pJ^{p-1}}J_x^p\right)\tau}$ and the Trotterized unitary given by

$$U_\delta(\tau) = e^{i(1-s)\tau J_z} e^{i\frac{s\tau}{pJ^{p-1}}J_x^p} \equiv U^{(0)}U' \ . \tag{4.10}$$

For $s \ll 1$, the above Floquet map is dominated by $U^{(0)}$, which generates precessions of the mean spin around the z axis; the term U' can be seen as perturbation. Hence, the eigenstates of the U_δ are expected to be close to those of $U^{(0)}$ with small corrections.

The eigenstates of $U^{(0)}$ are same as those of J_z eigenstates,

$$U^{(0)}|-J+m\rangle = e^{i(1-s)\tau(-J+m)}|-J+m\rangle \equiv e^{-i\phi_m^{(0)}}|-J+m\rangle \ , \tag{4.11}$$

where $m = \{0, 1, ..., 2J\}$, the eigenphases and eigenstates are denoted by $\phi_m^{(0)} = -(1-s)\tau(-J+m)$ and $|-J+m\rangle \equiv |J, m_z = -J+m\rangle$ respectively. The first order correction to the eigenstates of U_δ is then obtained by analyzing the following

equation,

$$U_\delta\Big(|-J+m\rangle + s|\phi_m^{(1)}\rangle\Big) = e^{-i\phi_m^{(0)}}(1-is\phi_m^{(1)})\Big(|-J+m\rangle + s|\phi_m^{(1)}\rangle\Big)$$
$$= e^{-i(1-s)\tau(-J+m)}(1-is\phi_m^{(1)})\Big(|-J+m\rangle + s|\phi_m^{(1)}\rangle\Big) \tag{4.12}$$

where s is the perturbation parameter, $\phi_m^{(1)}$ and $|\phi_m^{(1)}\rangle$ are the first order corrections to the eigenphases and the eigenstates respectively. Taking inner product with the J_z basis elements in the above equation, we obtain

$$\langle -J+m'|\phi_m^{(1)}\rangle = (1-\delta_{m',m})\frac{i\tau}{pJ^{p-1}}\frac{\left(J_x^p\right)_{m',m}}{e^{i(1-s)\tau(m-m')}-1}, \tag{4.13}$$

where $\left(J_x^p\right)_{m',m} \equiv \langle -J+m'|J_x^p|-J+m\rangle$ and $m,m' = \{0,1,...,2J\}$. The above expression for the first-order correction to the eigenstate is not valid in the immediate vicinity of the degenerate points given by $\tau = r\frac{2\pi}{(1-s)(m-m')}$ for some positive nonzero integer, r. However, in the regions around the immediate vicinity of the degenerate points, the above expression predicts a big correction to the unperturbed eigenstates whenever $\left(J_x^p\right)_{m',m} \neq 0$ for $m \neq m'$. Since the operator J_x^p, when expressed in the eigenbasis of J_z, has nonzero matrix elements only in alternating diagonal bands up to offset p, the matrix element $\left(J_x^p\right)_{m',m}$ is nonzero when $m-m' \equiv q = \{p, p-2, ..., 0(1)\}$ for even (odd) p-spin models. Hence, the regions with large eigenvector correction for

a given p-spin model can be identified as the neighborhood of

$$\tau^*_{p,q} \equiv r\frac{2\pi}{(1-s)q}\,, \tag{4.14}$$

where $q = \{p, p-2, ..., 2(1)\}$ for even (odd) p-spin models and r is a positive integer. The eigenstate structure in the region around $\tau^*_{p,q}$ changes rapidly with the Trotter-step size, and hence we refer to them as the structural instability regions of the Floquet operator. These instability regions are centered at $\tau^*_{p,q}$ with some width w. Note that the number of structural instability regions predicted by Eq. (4.15) increase with p value since q has more possibilities for higher values of p.

Consider the $p = 2$ case, which has only one structural instability region that is centered at $\tau^*_{2,2} = \frac{\pi}{1-s}$ [*]. The Floquet operator at $\tau^*_{2,2}$, which is the center of the instability region, is given by

$$U_\delta(\tau = \tau^*_{2,2}) = e^{i\pi J_z} e^{i\frac{s\pi}{(1-s)}\frac{1}{2J}J_x^2}\,. \tag{4.15}$$

The two terms in the above shown Floquet operator commute, as $(J_x)^2 \to (-J_x)^2$ under the action of the parity operator $e^{i\pi J_z}$, which implements a π rotation around the z-axis. Therefore, one can find a common set of eigenvectors for both operators $e^{i\pi J_z}$ and $e^{i\frac{s\pi}{(1-s)}\frac{1}{2J}J_x^2}$, which are given by the parity respecting eigenstates of J_x^2. That is, the eigenstates of $U_\delta(\tau = \tau^*_{2,2})$ are given by $\frac{1}{\sqrt{2}}\big(|J, m_x\rangle \pm |J, -m_x\rangle\big)$. Hence, as the Trotter-step size is varied across from $\tau \sim \tau^*_{2,2} - \frac{w}{2}$, the eigenstates of U_δ change

[*]There are instability regions in the vicinity of integer multiples of $\tau^*_{2,2}$, but these appear at large Trotter step sizes.

rapidly from those that have structure similar to the J_z eigenstates to those that have their structure resembling the J_x^2 eigenstates. As τ is increased further from $\tau = \tau^*_{2,2}$ to $\tau \sim \tau^*_{2,2} + \frac{w}{2}$, the eigenstate structure changes from being similar to J_x^2 eigenstates back to those of J_z eigenstates. It can be seen from Eq. (4.15) that all even p-spin models have a structural instability region centered at $\tau = \tau^*_{p,q=2} = r\frac{\pi}{1-s}$. In fact, $\tau^*_{p,q=2}$ is the black dashed curve that is plotted in Fig. 4.1 (a and c) and overlaps with the high dissimilarity region. Also, for a general even p-spin model, the structure of the eigenstates change from being similar to J_z eigenstates to those of J_x^2 eigenstates and then back to J_z eigenstates, identical to the $p = 2$ case, as Trotter-step size is varied from $\tau \sim \tau^*_{p,q=2} - \frac{w}{2}$ to $\tau \sim \tau^*_{p,q=2} + \frac{w}{2}$.

Since the eigenstates of the Trotterized unitary U_δ change significantly and rapidly in the structural instability regions, the unitary map U_δ becomes very different from the target unitary map U_{tar}. As a result, one would expect large simulation errors associated with various observables when the Trotter-step size is chosen to be in the instability region. We will focus here on analyzing errors in non-equilibrium quantities such as long-time averages in magnetization. The long-time average of an observable J_i is given by

$$\overline{\langle J_i \rangle} = \lim_{n\to\infty} \frac{1}{n} \sum_{l=1}^{n} \langle \psi_0 | (U^n)^\dagger J_i U^n | \psi_0 \rangle, \tag{4.16}$$

where U is the unitary map that generates the time evolution under the respective Hamiltonian for one Trotter-step size, $|\psi_0\rangle$ is the initial state and $i = \{x, y, z\}$. For concreteness, we focus on the simulation error in long-time average of J_z, which is

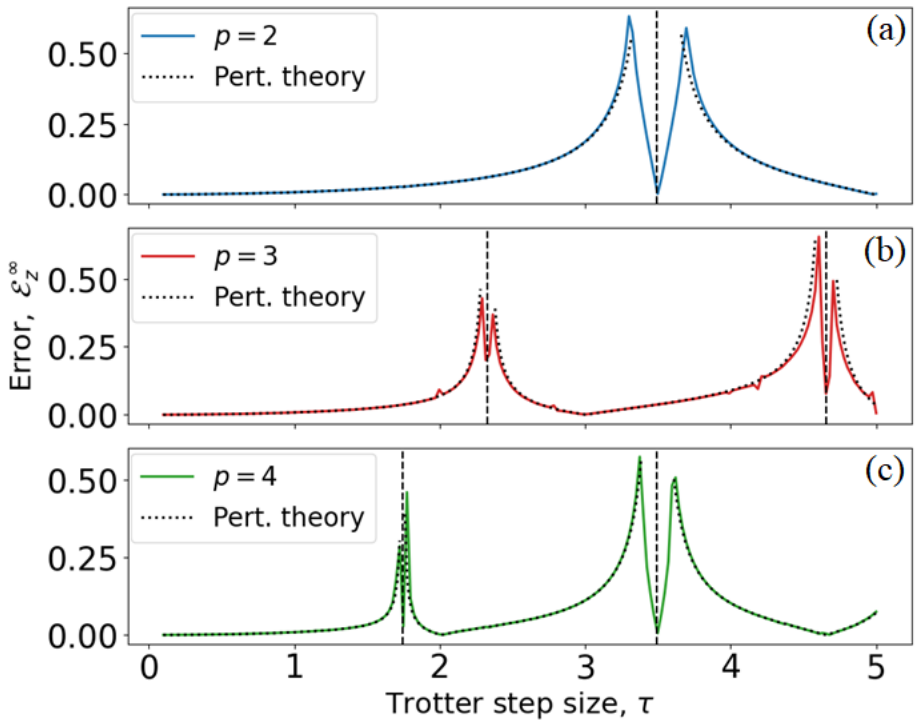

Figure 4.2: The error in the long-time averaged magnetization $\mathcal{E}_z$ obtained numerically for an initial condition $|\Theta_0 = \frac{\pi}{2}, \Phi_0 = 0\rangle$ is shown as a function of the Trotter-step size for $p = 2$, 3 and 4 by the blue, red and green colored curves respectively. The curve shown by the dotted line refers to the analytic expression mentioned in Eq. (4.20), and the vertical dashed lines refer to the center points of the various instability region.

defined as

$$\mathcal{E}_z^\infty(\tau) = \frac{1}{J}\left|\overline{\langle J_z\rangle}_{\rm tar} - \overline{\langle J_z\rangle}_{\rm trot}\right|, \tag{4.17}$$

where $\overline{\langle J_z\rangle}_{\rm tar}$ and $\overline{\langle J_z\rangle}_{\rm trot}$ are the time averages obtained under the action of the unitary maps $U_{\rm tar}$ and U_δ respectively. The simulation error in $\overline{\langle J_z\rangle}$ for an initial spin-coherent state $|\psi_0\rangle = |\Theta_0 = \frac{\pi}{2}, \Phi_0 = 0\rangle$ obtained from numerical calculation is shown in Fig. 4.2(a-c) for $p = 2$, $p = 3$ and $p = 4$ respectively. As anticipated, the error in $\overline{\langle J_z\rangle}$ increases sharply in the neighborhood of the instability regions given by $\tau^*_{2,2} = \frac{\pi}{1-s}$ for $p = 2$, $\tau^*_{3,1} = \frac{2\pi}{1-s}$, $\tau^*_{3,3} = \frac{2\pi}{3(1-s)}$ for $p = 3$ and $\tau^*_{4,2} = \frac{\pi}{1-s}$, $\tau^*_{4,4} = \frac{2\pi}{4(1-s)}$ for

$p = 4$ (the center points of these instability region are shown by the vertical dashed lines in Fig. 4.2). It can be seen in all these cases, the error first increases sharply, then decreases in the immediate neighborhood of the instability region before increasing again leading to two separate error peaks, both of which belong to the same instability region. The particular shape of error curve in the instability region is dependent on the initial state used and the observable being measured.

Note that number of high error regions increase with the value of p, as the instability regions also increase with p value. Moreover, these high error regions start to develop at smaller values of the Trotter-step size as the value of p is increased since $\tau^*_{p,q} = \frac{2\pi}{q(1-s)}$ becomes smaller as q is allowed to have larger values for larger p-spin model. However, the high error regions that appear at smaller values of the Trotter-step size have narrower width. We can understand this by analyzing the rate at which the spectrum becomes degenerate in a particular instability region as τ is varied. For this, we Taylor expand the spectral gap (shown in Eq. (4.14)) around the central point of the structural instability region as follows,

$$\frac{1}{e^{i(1-s)q\tau} - 1} \approx \frac{e^{-i(1-s)q\tau} - 1}{q^2(1-s)^2(\tau - \tau^*)^2}. \tag{4.18}$$

The width of the instability region is inversely proportional to the rate at which the system becomes degenerate, which is given by $\frac{1}{q^2(1-s)^2}$. This explains the fact the error regions that appear at smaller values of the Trotter-step size, which correspond to larger values of q, are narrower compared to the error regions centered at larger Trotter-step sizes.

We can also find an analytic expression for the error in the long-time averaged magnetization to first order in s. The expression for $\mathcal{E}_z^{\infty}(\tau)$, when the initial state is chosen to be a spin-coherent state $|\Psi^{(0)}\rangle = |\Theta, \Phi\rangle$, is given by

$$\mathcal{E}_z^{\infty}(\tau) = \Bigg| \sum_{q=\{p,p-2,\ldots,2(1)\}} \frac{sq}{pJ^{p-1}} \left[\cos(q\Phi) \left(\frac{2}{q(1-s)} - \tau \cot\Big(\frac{q(1-s)}{2}\tau\Big) \right) + \tau \sin(q\Phi) \right] \sum_{m=0}^{2J-q} |\rho^{(0)}_{m+q,m}(\Theta)| \, (J_x^p)_{m,m+q} \Bigg|, \tag{4.19}$$

where $A_{r_1,r_2} = \langle -J + r_1 | A | -J + r_2 \rangle$ for an operator A. For more details on the derivation of the above expression, and the more general expression for simulation error of an arbitrary observable with an arbitrary initial condition, refer to Appendix B. The above expression is shown by black dotted curve for the initial condition $|\psi_0\rangle = |\Theta_0 = \frac{\pi}{2}, \Phi_0 = 0\rangle$ in Fig. 4.2(a-c). As can be seen, it agrees well with the numerically obtained curves for simulation error besides the region in the immediate vicinity of the degenerate points ($\tau^*_{p,q}$), where the error curves have inverted-triangular shape (the analytic expressions are not shown in these regions in Fig. 4.2 because they diverge here). Beyond the immediate vicinity of the degenerate points, the expression shown in Eq. (4.20) predicts large error at every value of q present in the summation, which correspond to all the instability regions present in a given p-spin model. The cotangent term, which is the dominant term in the Eq. (4.20) around the high-error region, captures the shape of the peak outside the immediate vicinity of the instability region.

4.3 Effective Hamiltonian

We have seen in the previous section that the structure of the eigenvectors associated with the Floquet operator changes significantly from those of the target unitary operator in the instability regions, which result in large simulation errors. In this section, we will perform further analysis of the instability region that clarifies the connection with large simulation errors. We do this by constructing an effective Hamiltonian associated with $U_\delta(\tau)$ for the Trotter-step sizes in the instability region and with this, examine the classical limit of the associated effective Hamiltonian.

For small values of the control parameter $s \ll 1$, recall that the target unitary operator associated with all the p-spin models for one Trotter step is given by $U_{\text{tar}}(t = \tau) \sim e^{i(1-s)\tau J_z}$. This unitary operator essentially generates precessions of the mean spin around the z-axis. The dynamics of the Trotterized unitary operator $U_{\text{trot}} = U_\delta(\tau)^n$ closely resembles the action of the target unitary operator when the Trotter-step size is not in the instability regions. In the instability regions, as we will see, the classical phase-space structure associated with U_δ undergoes major structural changes associated with bifurcations of fixed points, leading to trajectories that are very different from the target dynamics.

We will start our analysis by considering the LMG Hamiltonian, whose target evolution and the Trotterized evolution are shown in Eq. (4.5) and Eq. (4.6) respectively with $p = 2$. To better understand the Trotterized dynamics in the instability regions,

we analyze U_δ^2 as shown below,

$$\begin{aligned}\left(U_\delta(\tau_{2,2}^*+\Delta\tau)\right)^2 &= \left(e^{i\pi J_z}e^{i(1-s)\Delta\tau J_z}e^{i\frac{s}{2J}(\tau_{2,2}^*+\Delta\tau)J_x^2}\right)^2 \\ &= e^{i2\pi J_z}\left(e^{i(1-s)\Delta\tau J_z}e^{i\frac{s}{2J}(\tau_{2,2}^*+\Delta\tau)J_x^2}\right)^2.\end{aligned} \tag{4.20}$$

For s, $\frac{\Delta\tau}{\tau_{2,2}^*+\Delta\tau} \ll 1$, the unitary map can be written as $\left(U_\delta(\tau_{2,2}^*+\Delta\tau)\right)^2 = \pm\, e^{-i2(\tau_{2,2}^*+\Delta\tau)H_{\text{eff}}^{(2,2)}}$ with

$$H_{\text{eff}}^{(2,2)} = -(1-s)\frac{\Delta\tau}{\tau_{2,2}^*+\Delta\tau}J_z - \frac{s}{2J}J_x^2. \tag{4.21}$$

Hence, the Trotterized dynamics of the system every alternate step in the instability region can be described by this effective Hamiltonian. For $\Delta\tau > 0$, this Hamiltonian is also the target LMG Hamiltonian that we want to simulate but with an effective control parameter s_{eff} given by

$$s_{\text{eff}} = \frac{1}{1+\frac{1-s}{s}\frac{\Delta\tau}{\tau_{2,2}^*+\Delta\tau}}, \tag{4.22}$$

which is always greater than $1/2$ when $\Delta\tau$ is chosen in the structural instability region. More specifically, the effective control parameter increases from $1/2$ to 1 as $\Delta\tau$ is decreased from $\frac{\pi}{1-s}(\frac{s}{1-2s})$ to 0. Therefore, the Trotterized unitary every other step implements the dynamics associated with the ferromagnetic phase of the LMG Hamiltonian even though the goal was to simulate paramagnetic dynamics ($s \ll 1$), which corresponds to precessions about the external field.

We can further substantiate this result by investigating the associated classical

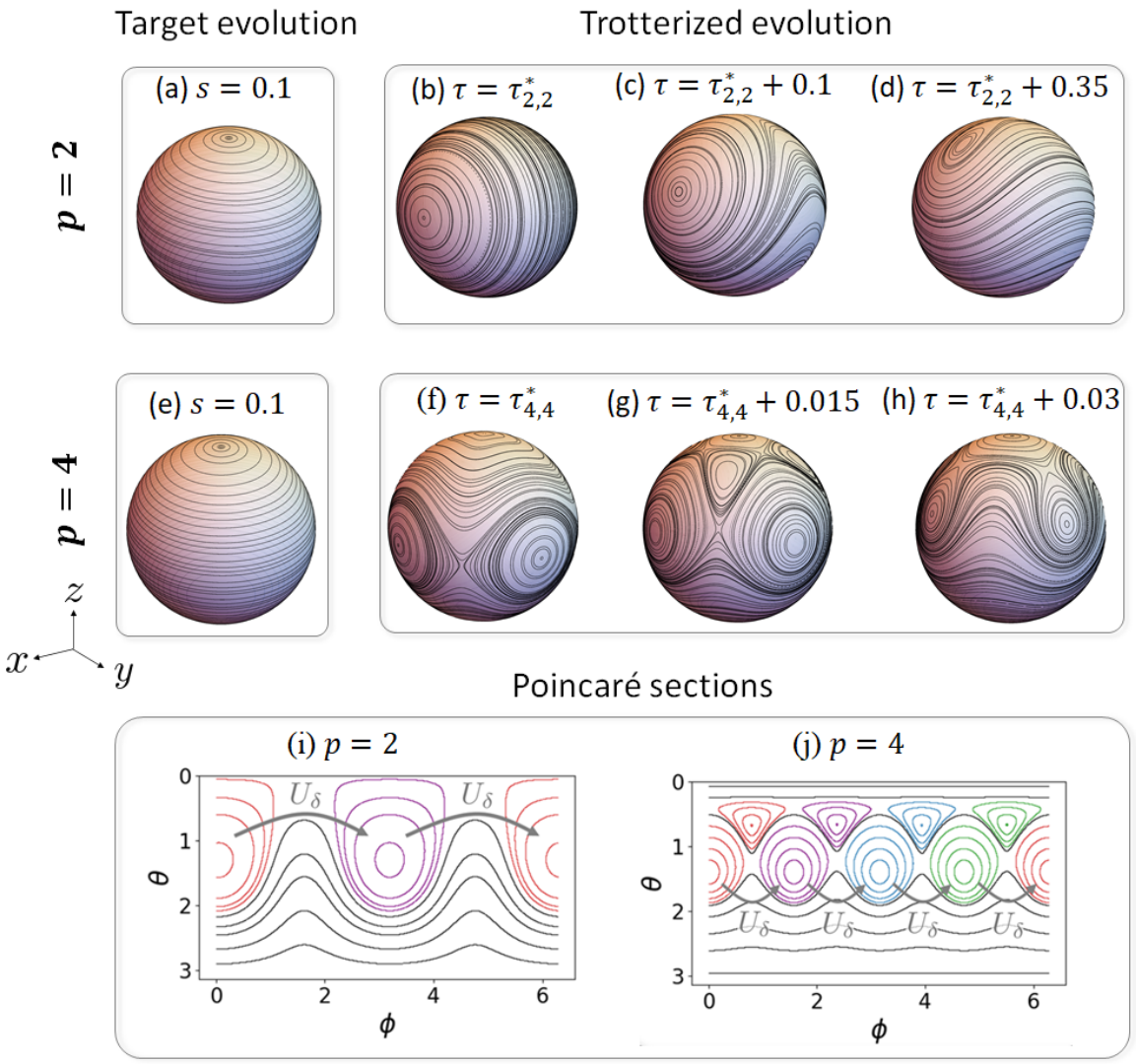

Figure 4.3: (a,e) The classical phase space trajectories associated with the target Hamiltonian at $s = 0.1$ for $p = 2$ and $p = 4$ are shown in (a) and (e) respectively. **(b-d):** The phase-space trajectories traced out by the Trotter dynamics in the instability region around $\tau^*_{2,2}$ are shown here. The change in the phase space structure in this case is accomodated by a one to two bifurcation. **(f-h):** The phase-space trajectories under Trotter evolution in the instability region around $\tau^*_{4,4}$. The changes on the phase space are facilitated by various one to four bifurcations. **(i,j):** Identical to the phase-space trajectories shown in (c) and (g), but plotted as a function of the spherical coordinates θ and ϕ. The trajectories that are bounded by the various homoclinic/ heteroclinic orbits are plotted in different colors. For $p = 2$ (shown in (i)), an initial condition that starts in one of the lobes goes back and forth between the two lobes tracing out the effective Hamiltonian dynamics every second step. For $p = 4$ (shown in (j)), an initial condition that starts in one of the lobes jumps through all the four different lobes leading to the dynamics of the effective Hamiltonian only every fourth step.

phase space trajectories. In Fig. 4.3 (a), we show the classical phase space associated with U_{tar} for $s = 0.1$, which effectively consists of precessions around the z-axis as expected. The phase space associated with U_{trot} in the neighborhood of $\tau^*_{2,2} = \frac{\pi}{1-s} \approx 3.49$ is shown in Fig. 4.3 (b-d), where the precessions around the z-axis change to precessions around the x-axis as τ is decreased from $\sim (\tau^*_{2,2} + \frac{\pi}{1-s}(\frac{s}{1-2s}))$ to $\tau^*_{2,2}$ (seen left to right in the figure) in a manner identical to the transition that occurs in the ideal LMG Hamiltonian as s is increased from 1/2 to 1. Note that even though the phase space associated with the Trotter dynamics looks identical to the phase space for the LMG Hamiltonian with s_{eff} given in Eq. (4.23), the individual trajectories on the associated Trotterized phase-space trace out the LMG Hamiltonian trajectories only when one considers every alternate step of the Trotterized evolution. This process is facilitated by a period-doubling bifurcation, where a stable fixed point located at $Z = 1$ becomes unstable at $\tau = \tau^*_{2,2} + \frac{\pi}{1-s}(\frac{s}{1-2s})$ and breaks into two other stable fixed points as τ is decreased towards $\tau^*_{2,2}$. As a result of this bifurcation, an orbit of period two is created, which constitutes the two fixed points (period 2) on the hemisphere $Z \geq 0$ shown in Fig. 4.3 (b-d). A initial condition located on one of the fixed points inside a particular homoclinic orbit goes back and forth with the second fixed point located inside the other homoclinic orbit. Likewise, an initial condition located in the neighborhood of these fixed points but inside the homoclinic orbits also jump between the two lobes (purple and red lobes in Fig. 4.3 (i) where the phase space trajectories are plotted as a function of spherical coordinates θ and ϕ) present on either side of the YZ plane tracing out the corresponding LMG Hamiltonian trajectories only when odd/even steps are considered. On the other hand, for initial

conditions located outside the homoclinic orbits, the Trotter dynamics trace out the actual LMG Hamiltonian trajectories every single step (black-colored curves in Fig. 4.3 (i)). Repeating the above analysis for negative values of $\Delta\tau$, one finds that all the processes described above, including period-doubling bifurcation for $\Delta\tau > 0$ now take place on the hemisphere $Z < 0$.

A similar investigation of the structural instability regions present around $\tau^*_{p,2} = \frac{\pi}{1-s}$ for a general even p-spin model shows that the Trotter dynamics in these cases is also described by the ferromagnetic phase of the corresponding p-spin Hamiltonian (or the Hamiltonian with a relative negative sign for $\Delta\tau < 0$) for small values of s although the target evolution always corresponds to executing paramagnetic-phase dynamics.

The dynamics in the other instability regions is even more different from the target dynamics. For instance, consider the instability region around $\tau^*_{4,4} = \frac{\pi}{2(1-s)}$ in the $p = 4$ case. Analyzing $\left(U_\delta(\tau^*_{4,4}+\Delta\tau)\right)^4$ in this case, one finds the effective Hamiltonian that describes the dynamics every fourth step, which is given by

$$H^{(4,4)}_{\text{eff}} = -(1-s)\frac{\Delta\tau}{\Delta\tau + \tau^*_{4,4}} J_z - \frac{s}{8J^3}(J_x^4 + J_y^4). \tag{4.23}$$

The phase space trajectories associated with the Trotter dynamics in the neighborhood of $\tau^*_{4,4}$ are shown in Fig. 4.3 (f-h). In this case, the initial conditions that are bound by the various heteroclinic orbits trace out the trajectories associated with $H^{(4,4)}_{\text{eff}}$ only every fourth step. In the intermediate steps, the Trotterized dynamics involves jumping between the different lobes present on the phase space. This is illustrated using Fig 4.3 (j) where the red, purple, blue and green colored trajectories

represent every first, second, third and fourth step respectively. The change in the structure of the phase-space trajectories in this case is accommodated by two different 1-to-4 bifurcations.

In the general case, the Trotter dynamics in the neighborhood of $\tau^*_{p,q} = r\frac{2\pi}{q(1-s)}$ can be understood by analyzing $\big(U_\delta(\tau+\Delta\tau)\big)^q$ as shown below

$$\begin{aligned}(U_\delta(\tau+\Delta\tau))^q &= \big(e^{i\frac{2\pi}{q}J_z}e^{i(1-s)\Delta\tau J_z}e^{i\frac{s}{pJ^{p-1}}(\tau^*_{p,q}+\Delta\tau)J_x^p}\big)^q \\ &= \pm W_{\frac{(2q-2)\pi}{q}}...W_{\frac{4\pi}{q}}W_{\frac{2\pi}{q}}W,\end{aligned} \tag{4.24}$$

where

$$W \equiv e^{i(1-s)\Delta\tau J_z}e^{i\frac{s}{pJ^{p-1}}(\tau^*_{p,q}+\Delta\tau)J_x^p}, \tag{4.25}$$

and

$$\begin{aligned}W_\theta &\equiv e^{-i\theta J_z}We^{i\theta J_z} \\ &= e^{i(1-s)\Delta\tau J_z}e^{i\frac{s}{pJ^{p-1}}(\tau^*_{p,q}+\Delta\tau)(J_x\cos\theta+J_y\sin\theta)^p}.\end{aligned} \tag{4.26}$$

When s, $\frac{\Delta\tau}{\tau^*+\Delta\tau} \approx \frac{\Delta\tau}{\tau^*} \ll 1$, the Trotterized evolution every q^{th} step can be described using an effective Hamiltonian defined by $\big(U_\delta(\tau+\Delta\tau)\big)^q = e^{-iq(\tau^*_{p,q}+\Delta\tau)H_{\text{eff}}^{(p,q)}}$, where $H_{\text{eff}}^{(p,q)}$ is given by

$$\begin{aligned}H_{\text{eff}}^{(p,q)} &= -(1-s)\frac{\Delta\tau}{\tau^*+\Delta\tau}J_z \\ &\quad - \frac{s}{pqJ^{p-1}}\sum_{m=1}^{q}\left(J_x\cos\left[\frac{2\pi(m-1)}{q}\right]+J_y\sin\left[\frac{2\pi(m-1)}{q}\right]\right)^p.\end{aligned} \tag{4.27}$$

The above expression for the effective Hamiltonian can be simplified for the even p-spin models, which have additional parity symmetry. In that case, the $(\frac{q}{2}+k)^{th}$ term in the summation becomes identical to the k^{th} term, and the number of terms in the summation decrease by half. On the classical phase space, the Trotterized dynamics undergoes a 1 to q bifurcation at the edges of the instability region resulting in creation of period q orbits, and thus q different lobes. As expected, the Trotter evolution realizes the trajectories of $H_{\text{eff}}^{(p,q)}$ only every q^{th} step and leads to jumping between q different lobes in the intermediate steps. The presence of these lobes can also be seen by the presence of an emergent symmetry [†] that appears in the structural instability region. The emergent symmetry is the invariance of the effective Hamiltonian shown in Eq. (4.28) under $\frac{2\pi}{q}$ rotation around the z-axis: $[H_{\text{eff}}^{(p,q)}, e^{i\frac{2\pi}{q}J_z}] = 0$. Therefore, the associated classical phase space is also invariant under such rotation.

In conclusion, the construction of the effective Hamiltonian provides a physical picture of the connection between the instability regions and large errors in the simulation. We showed that for the Trotter step sizes chosen in the instability region, the Trotterized unitary leads to time evolution of the system under an effective Hamiltonian that is very different from the target Hamiltonian. Based on classical phase space analysis, we showed that these structural changes in the instability region are assisted by various bifurcations that lead to creation of periodic orbits and hyperbolic points that are not present on the phase space associated with the ideal, target

[†]This symmetry is called emergent symmetry because it arises due to the drive and is absent in the undriven system. These symmetries can be approximate meaning that only the first few terms in the convergent expansion of the effective Hamiltonian respect these symmetries, and they have important consequences such as non-trivial steady states in the long-time limit of a Floquet system [LDM14], etc. For more details on the study of emergent symmetries, refer to [HD21, HSMD21].

Hamiltonian.

5

Summary and Outlook

The idea of quantum simulation was introduced by Feynman in 1982. Since then, significant developments in the field have led us to the NISQ era, where we have devices of moderate size that have the capability, in the absence of imperfections, to simulate systems that cannot be simulated on a classical computer. One of the main goals associated with these NISQ-era simulators, which are faulty due to lack of error correction, is to extract a quantity reliably from the quantum simulation of a system that cannot be efficiently simulated on a state-of-the-art classical computer. In the work presented in this dissertation, we have analyzed the role played by the physical

properties of the system being simulated in determining the output error of an analog quantum simulator. Specifically, in Chapter 3 and 4, we have presented our results on the reliability of quantum simulation in the absence of error correction corresponding to two different paradigms.

In Chapter 3, we have considered the setting where an external perturbation causes the simulation of an integrable system (LMG model) to become chaotic. We then have analyzed the reliability of the simulator in extracting quantities such as the time-averaged magnetization and the critical point estimates. For this, we have first proposed protocols to extract the critical points of the ground-state quantum phase transition (GSQPT) and the dynamical quantum phase transition (DQPT) inspired by the semi-classical description of the LMG model. Followed by this, we have characterized the emergence of chaos in the system as a function of the perturbation strength. Finally, we have showed that the critical point estimates are robust to perturbations because they correspond to global changes in the structure of the phase space and does not require knowledge about the whole quantum state. On the other hand, the time-averaged magnetizations associated with the initial conditions of the GSQPT and the DQPT protocols are affected significantly as the quantity depends on the state of the system.

Here, we have only studied the reliability of quantum simulation in extracting information about the GSQPT and the DQPT. It would be interesting to extend this study to investigate the excited-state quantum phase transitions (ESQPTs) in the presence of chaos-inducing perturbation. Since the ESQPTs in the mean-field limit are associated with the states localized in the vicinity of the unstable fixed

point, it is reasonable to expect that the various signatures of the ESQPTs become fragile in the presence of chaos for values of the control parameter around the critical point [STPB16]. Furthermore, beyond the collective spin systems with one degree of freedom, it is interesting to explore the effects of many-body chaos in many-body models.

In Chapter 4, we have considered the framework where the time evolution associated with the Hamiltonian of interest is simulated through the Trotter-Suzuki decomposition (Trotterization). The accuracy of the simulation increases as the Trotter-step size is decreased. We have shown that the simulation errors associated with magnetization in the p-spin models increase sharply around certain values of the Trotter-step sizes, referred to as the structural instability regions. We have analytically obtained the location of these regions among other characteristics through the use of the unitary perturbation theory. Moreover, we showed that the number of such high-error regions increase with the value of p. Also, the high-error regions that are associated with higher values of p appear at smaller values of the Trotter-step sizes making them relevant for the NISQ-era devices. Finally, we were able to explain the presence of large simulation errors in instability regions through the explicit construction of an effective Hamiltonian, which models the Trotter evolution accurately for all the p-spin models in the instability regions. In the mean-field limit, these instability regions are characterized by multiple bifurcations leading to rapid changes in the structure of the phase space.

We have also found that the delta kicked p-spin Hamiltonian (Eq. (4.7)), which generates the time-evolution under the Trotter-Suzuki decomposition of the p-spin Hamil-

tonian, shows interesting non-equilibrium behavior. In particular, the delta-kicked p-spin Hamiltonian develops a subharmonic response with periodicity nT where $n \geq 2$ even though the kicked Hamiltonian is periodic with period T provided the parameter regimes correspond to instability regions. A system showing such behavior is said to be in a Floquet time crystal phase. An exhaustive study of the Floquet time crystal behavior in the kicked p-spin models is presented in the preprint [MnACP22].

In summary, the results shown in this dissertation suggest that the output of a quantum simulator cannot be fully trusted in the absence of error correction. For this, we have made an extensive use of the p-spin models, which are mean-field models. The mean-field nature of the p-spin models allowed us to perform explicit calculations and obtain important important insights into various aspects of our work. We want to point out that the results presented in this dissertation are likely to apply to other many-body systems that are not mean-field models. This intuition follows from the fact that all-to-all interaction graphs are often seen to provide correct behavior of the systems described by the Hamiltonian $H = BJ_z + \sum_{i,j} \frac{J_0}{|i-j|^\alpha} \sigma_x^{(i)} \sigma_x^{(j)}$ for $\alpha \lesssim 2$. For instance, Zunkovic et al. use the intuition gained from the mean-field analysis of the LMG model ($\alpha = 0$) to understand the various aspects of the dynamical quantum phase transitions in the models with small, nonzero values of α [ŽHKS18]. Similarly, Zhang et al. also use the mean-field analysis ($\alpha = 0$) to understand the DQPT behavior for $\alpha \sim 1$ [ZPH+17]. Finally, in Ref. [SOE+19], Sieberer et al. also first exhibit the relationship between large Trotter errors and chaos using the mean-field LMG model, and then extend their analysis numerically to non-zero values of α. The above-mentioned works hint that our results obtained from the mean-field models

generalize to other finite-range models with nonzero values of α. We will leave it as future work to extend our results to many-body systems and explore other properties that affect reliability of the simulator.

A

Finite-size Scaling of GSQPT Critical Point

In this appendix, we derive the critical point scaling with the system size of the GSQPT. The goal is to obtain the barrier height and the zero-point energy of the system using the potential shown in Eq. (2.36) and then obtain the value of the control parameter s when this occurs. The expression for the barrier height can be obtained from the effective potential $V(s,x)$ by subtracting potential at the global minima from the barrier height (barrier is located at $x=0$)

$$V(s,x=0)-V\big(s,x=x_0\big)=\left(s-1+\frac{1}{4s}\right)+\frac{1}{N}\left(s-\frac{1}{2}\right)+\mathcal{O}\left(\frac{1}{N^2}\right), \qquad \text{(A.1)}$$

where $x_0 = \frac{\sqrt{2s-1}}{s} - \frac{s}{\sqrt{2s-1}}h + \mathcal{O}(h^{3/2})$ is the point of global minima. The zero-point energy can then be computed by noting that the potential energy expression in Eq. (2.36) will be of the form $V(s,x) = V(s,x_0) + \frac{1}{2}m\omega^2(x-x_0)^2$ when Taylor expanded around $x = x_0$ with $m\omega^2 = \left.\frac{\partial^2 V(s,x)}{\partial x^2}\right|_{x=x_0}$. Therefore, the zero-point energy is given by

$$\begin{aligned} E_0 &= h\frac{\omega}{2} \quad \text{where} \quad h = \frac{1}{N} \\ &= h\sqrt{\frac{s(2s-1)}{(s-1)}} + \mathcal{O}(h^2)\ . \end{aligned} \tag{A.2}$$

Recall that the system has position-dependent mass, but we approximate the mass in the above equation by its value at the point of the global minimum. Setting the barrier equal to the zero-point energy, one obtains

$$s_c^{(gpt)}(N) = \frac{1}{2} + \frac{N^{-\frac{2}{3}}}{2^{\frac{1}{3}}} + \mathcal{O}\left(\frac{1}{N}\right), \tag{A.3}$$

which can be rewritten as

$$\frac{s_c^{(gpt)}(N) - s_c^{(gpt)}}{s_c^{(gpt)}} \propto N^{-\frac{2}{3}}\ . \tag{A.4}$$

B

Perturbation theory expression

The long-time average of an operator A, assuming the time-evolution operator corresponding to one time-step has nondegenerate eigenphases, is given by

$$\overline{\langle A \rangle}_{\infty} = \sum_{r=1}^{d} \langle \phi_r | \rho^{(0)} | \phi_r \rangle \langle \phi_r | A | \phi_r \rangle \tag{B.1}$$

where $\rho^{(0)}$ is the initial state and $|\phi_r\rangle$ is the r^{th} eigenstate of the system. The error in this observable due to Trotterization is given by

$$\mathcal{E}_A^{\infty}(\tau) = \frac{1}{J} |\overline{\langle A \rangle}_{\infty,\mathrm{id}} - \overline{\langle A \rangle}_{\infty,\tau}| \tag{B.2}$$

where $\overline{\langle A\rangle}_{\infty,\mathrm{id}}$ is the long-time average of A under the ideal Hamiltonian evolution, and $\overline{\langle A\rangle}_{\infty,\tau}$ is the long-time average under Trotterized evolution. Assuming that the eigenstates of the system change under a perturbation $|\phi_r\rangle \to |\phi_r^{(0)}\rangle + \lambda|\phi_r^{(1)}\rangle$, the expression for the long-time average to the first order is given by

$$\overline{\langle A\rangle}_{\infty,\lambda} = \sum_{m=0}^{2J} \rho_{m,m}^{(0)} A_{m,m} + 2\lambda \sum_{m,n\neq m}^{2J} \mathrm{Re}\Big(\big(A_{m,m}\, \rho_{n,m}^{(0)} + \rho_{m,m}^{(0)}\, A_{n,m}\big) \langle\phi_m^{(1)}|\phi_n^{(0)}\rangle \Big) \quad \text{(B.3)}$$

The above expression can be evaluated for ideal Hamiltonian evolution to obtain $\overline{\langle A\rangle}_{\infty,id}$ up to first order in s using Hamiltonian perturbation theory with $H_0 = -(1-s)J_z$ being the unperturbed Hamiltonian and $H_1 = -\frac{s}{pJ^{p-1}} J_x^p$ being the perturbed Hamiltonian

$$\overline{\langle A\rangle}_{\infty,\mathrm{id}} = \sum_{m=0}^{2J} \rho_{m,m}^{(0)} A_{m,m} + \frac{2s}{pJ^{p-1}(1-s)} \sum_{m,n\neq m}^{2J} \mathrm{Re}\Big(\big(A_{m,m}\, \rho_{n,m}^{(0)} + \rho_{m,m}^{(0)}\, A_{n,m}\big) \frac{(J_x^p)_{m,n}}{m-n} \Big) \quad \text{(B.4)}$$

Likewise, Eq. (B.1) can be evaluated to obtain $\overline{\langle A\rangle}_{\infty,\tau}$ up to first order in s using unitary perturbation theory with unperturbed unitary, $U_0 = e^{i(1-s)\tau J_y}$, and the perturbed unitary $U_p = e^{is\tau \frac{J_z^p}{pJ^{p-1}}}$

$$\begin{aligned} \overline{\langle A\rangle}_{\infty,\tau} &= \sum_{m=0}^{2J} \rho_{m,m}^{(0)} A_{m,m} \\ &\quad + \frac{2s\tau}{pJ^{p-1}} \sum_{m,n\neq m}^{2J} \mathrm{Re}\Big(\big(\rho_{n,m}^{(0)} A_{m,m} + A_{n,m}\rho_{m,m}^{(0)}\big) \frac{-i(J_x^p)_{m,n}}{e^{-i(1-s)\tau(m-n)} - 1} \Big) \end{aligned} \quad \text{(B.5)}$$

The error is then given by

$$\mathcal{E}_A^{\infty}(\tau) = \frac{2s}{pJ^{p-1}}\Bigg|\sum_{m,n\neq m}^{2J} \mathrm{Re}\Bigg(\big(A_{m,m}\rho^{(0)}_{n,m} + \rho^{(0)}_{m,m}\,A_{n,m}\big)(J_x^p)_{m,n} \left(\frac{1}{(1-s)(m-n)} + \frac{i\tau}{e^{-i(1-s)\tau(m-n)}-1}\right)\Bigg)\Bigg| \tag{B.6}$$

The above expression can be further simplified by expanding the summation in n and noticing the matrix elements of $(J_x^p)_{m,n}$ are nonzero for $n = m \pm p, m \pm p-2, ..., m \pm 0(1)$. Focusing on two particular terms with $n = m \pm p - q$ we obtain

$$\begin{aligned}\mathcal{E}_A^{\infty}(\tau)\big|_{n=m\pm q} = \frac{2s}{pJ^{p-1}}\sum_{m=0}^{2J-(p-q)} \mathrm{Re}\Bigg[\Big(\rho^{(0)}_{m+p-q,m}A_{m,m} + A_{m+p-q,m}\rho^{(0)}_{m,m}\Big)(J_x^p)_{m,m+p-q} \left(\frac{i\tau}{e^{i(p-q)(1-s)\tau}-1} - \frac{1}{(p-q)(1-s)}\right)\Bigg] \\ + \frac{2s}{pJ^{p-1}}\sum_{m=p-q}^{2J} \mathrm{Re}\Bigg[\Big(\rho^{(0)}_{m-(p-q),m}A_{m,m} + A_{m-(p-q),m}\rho^{(0)}_{m,m}\Big)(J_x^p)_{m,m-(p-q)} \left(\frac{i\tau}{e^{-i(p-q)(1-s)\tau}-1} + \frac{1}{(p-q)(1-s)}\right)\Bigg]\end{aligned} \tag{B.7}$$

Manipulating the second term in above expression by first shifting the index of the second term in the above equation, $m \to m-(p-q)$, and then setting $\mathrm{Re}[z] = \mathrm{Re}[z^*]$

in the second term results in the following expression for the error

$$\mathcal{E}_A^{\infty}(\tau) = \frac{2s}{pJ^{p-1}} \sum_{q=\{0,2,\ldots,p-1(p)\}} \sum_{m=0}^{2J-(p-q)} \mathrm{Re}\Bigg[\Big(\rho^{(0)}_{m+p-q,m}\big(A_{m+p-q,m+p-q} - A_{m,m}\big) + A_{m+p-q,m}\big(\rho^{(0)}_{m+p-q,m+p-q} - \rho^{(0)}_{m,m}\big)\Big)(J_x^p)_{m,m+p-q}\left(\frac{1}{(p-q)(1-s)} - \frac{i\tau}{e^{i(p-q)(1-s)\tau}-1}\right)\Bigg] \tag{B.8}$$

Focusing on the error in J_z, the above expression further simplifies to the following

$$\mathcal{E}_z^{\infty}(\tau) = \frac{2s}{pJ^{p-1}} \sum_{q=\{0,2,\ldots,p-1(p)\}} \sum_{m=0}^{2J-(p-q)} \mathrm{Re}\Bigg[\big(p-q\big)\rho^{(0)}_{m+p-q,m}(J_x^p)_{m,m+p-q} \left(\frac{1}{(p-q)(1-s)} - \frac{i\tau}{e^{i(p-q)(1-s)\tau}-1}\right)\Bigg] \tag{B.9}$$

Relabelling the index $q \to p-q$ results in the final expression,

$$\mathcal{E}_z^{\infty}(\tau) = \frac{2s}{pJ^{p-1}} \sum_{q=\{p,p-2,\ldots,0(1)\}} \sum_{m=0}^{2J-q} \mathrm{Re}\Bigg[q\rho^{(0)}_{m+q,m}(J_x^p)_{m,m+q}\left(\frac{1}{q(1-s)} - \frac{i\tau}{e^{iq(1-s)\tau}-1}\right)\Bigg] \tag{B.10}$$

C

Beyond Mean Field Limit

In Chapter 2, we have considered the p-spin models in the mean-field limit. Specifically, we obtained the Heisenberg equations of motion (Eq. (2.41)) for the collective angular momentum operators and then ignored the mean-field fluctuations by setting $\langle O_1 O_2 \rangle = \langle O_1 \rangle \langle O_2 \rangle$. Without resorting to such approximation, the equations of motion for the angular momentum operators $\big(\langle J_x \rangle, \langle J_y \rangle, \langle J_z \rangle\big)$ couple to expectation values of second-order polynomials in angular momentum operators, which in turn couple to higher-order polynomials resulting in a hierarchy of coupled differential equations. In the mean-field limit, we ignore the correlations between the

operators by setting the second order cumulant, $\langle\langle O_1 O_2\rangle\rangle \equiv \langle O_1 O_2\rangle - \langle O_1\rangle\langle O_2\rangle$, to zero. This limit is useful in the p-spin model as it describes the thermodynamic limit ($N \to \infty$) or the classical limit. A known technique to study larger dimensional systems ($N \gg 1$, but $N \neq \infty$) without solving for the equations associated with the full quantum system is to approximate the third correlations in terms of lower-order correlations and ignore the role played by higher-order correlations in the equations of motion. This is achieved by setting all the third-order cumulants, $\langle\langle O_1 O_2 O_3\rangle\rangle \equiv \langle O_1 O_2 O_3\rangle - \langle O_1 O_2\rangle\langle O_3\rangle - \langle O_1\rangle\langle O_2 O_3\rangle - \langle O_1 O_3\rangle\langle O_2\rangle + 2\langle O_1\rangle\langle O_2\rangle\langle O_3\rangle$, to zero. As a result, one could learn about the behavior of large N collective-spin systems by just solving 8 coupled differential equations instead of $N+1$ differential equations resulting from the Schrodinger equation. This limit has been studied in the LMG model in Ref. [VA00].

A question then arises: can one study systems that are too large to be analyzed by solving $N+1$ differential equations but small enough such that the higher-order correlation functions play an important role? A straightforward way to analyze such systems is the cumulant expansion method, whereby one sets n^{th}-order cumulant to zero, which will result in ignoring $(n+1)^{th}$- order and higher order correlations, and then numerically solves the closed set of coupled differential equations involving operators that contain product of at most $n-1$ operators. The n^{th} order cumulant of product of n operators is defined as

$$\langle\langle O_1 O_2 ... O_n\rangle\rangle \equiv \sum_{l=0}^{n-1} (-1)^l \; l! \; C_l(O_1 O_2, ..., O_n) \; , \tag{C.1}$$

where $C_l(O_1, O_2, ..., O_n)$ requires identifying all the l partitions of the product $O_1O_2...O_n$ while preserving the order of the operators and replacing the resulting $l+1$ subsets with their expectation values. $C_l(O_1, O_2, ..., O_n)$ is then obtained by summing over all such possible terms for a given p. For instance, for $n = 3$, $C_0(O_1O_2O_3) = \langle O_1O_2O_3\rangle$, $C_1(O_1O_2O_3) = \langle O_1O_2\rangle\langle O_3\rangle + \langle O_1\rangle\langle O_2O_3\rangle + \langle O_1O_3\rangle\langle O_2\rangle$ and $C_2(O_1O_2O_3) = \langle O_1\rangle\langle O_2\rangle\langle O_3\rangle$. For more details on cumulants, refer to [G+85]. In fact, this algorithm has been recently implemented in Julia programming language to build equations of motion in quantum optical systems [PHR22]. In this appendix, we attempt to construct analytic expressions for the coupled differential equations in the LMG model using spherical tensors. We will first provide a brief introduction to the spherical tensors in the next section, and then use them in the following section to construct equations of motion analytically.

C.1 Spherical Tensors

A spherical tensor of rank k is defined as an operator that transforms under rotations in the manner similar to spherical harmonics as shown below

$$\mathcal{D}(R)\; T_q^{(k)}(J)\; \mathcal{D}^\dagger(R) = \sum_{q'=-k}^{k} \langle k, q'|\mathcal{D}(R)|k, q\rangle\; T_{q'}^{(k)}(J)\;, \tag{C.2}$$

where $\mathcal{D}(R) = e^{-i\gamma\, \vec{J}.\vec{n}}$ is the rotation operator with rotation specified by the angle γ and rotation axis $\vec{n}$ [SN14]. Equivalently, they can be defined using the following

commutator relationships [SN14],

$$[J_z, T_q^{(k)}(J)] = qT_q^{(k)}(J) \tag{C.3}$$

$$[J_\pm, T_q^{(k)}(J)] = \sqrt{k(k+1) - q(q\pm 1)}T_{q\pm 1}^{(k)}(J) \tag{C.4}$$

Unlike Cartesian tensors, spherical tensors are irreducible, so they cannot be further decomposed into components that behave differently under the action of rotation operators. The spherical tensors can be explicitly expressed in terms of angular momentum eigenstates as

$$T_q^{(k)}(J) = \sqrt{\frac{2k+1}{2J+1}} \sum_{m,m'=-J}^{J} C_{J\ m;k\ q}^{J\ m'} |J, m'\rangle\langle J, m| \tag{C.5}$$

where $J_z|J, m\rangle = m|J, m\rangle$, k and q are both integers with $0 \leq k \leq 2J$ and $-k \leq q \leq k$ [KR08]. In the remainder of the Appendix, we will implicitly assume the dependence of J in spherical tensor operators and denote the tensors by just $T_q^{(k)}$. The above set of operators form an orthonormal basis for

$$\mathrm{Tr}\big((T_{q_1}^{(k_1)})^\dagger T_{q_2}^{(k_2)}\big) = \delta_{k_1,k_2}\delta_{q_1,q_2} \tag{C.6}$$

Similar to spherical harmonics, they also have the following property

$$\big(T_q^{(k)}\big)^\dagger = (-1)^q T_q^{(k)} \tag{C.7}$$

From Eq. (C.5), the rank 0 tensor can be trivially identified as an identity operator,

$$T_0^{(0)} = \frac{1}{\sqrt{2J+1}}\,\mathrm{I}\,. \tag{C.8}$$

All the spherical tensors can be explicitly constructed in terms of collective angular momentum operator. For this, notice that the k^{th} component of a rank k tensor can be identified in a straightforward manner as

$$T_k^{(k)}(J) = (-1)^k \frac{2^k}{\pi^{1/4}} \sqrt{\frac{(2k+1)(k-1/2)!\,(2J-k)!}{k!\,(2J+k+1)!}} J_+^k \tag{C.9}$$

since the Clebsch Gordon coefficient $C^{J\ -k+m}_{J\ m;\ k\ -k}$ is known analytically. The remaining spherical tensors in terms of the collective angular momentum operators can be obtained in a manner analogous to deriving the eigenstates of J_z from the stretched state using the lowering operator. Following Eq. (C.4), one can construct $(k-p)^{\text{th}}$ component of a rank k tensor using p commutators as shown below

$$T_{k-p}^{(k)} = (-1)^k \frac{2^k}{\pi^{1/4}} \sqrt{\frac{(2k+1)(k-1/2)!\,(2J-k)!}{k!\,(2J+k+1)!}} \sqrt{\frac{(2k-p)!}{(p)!(2k)!}} [J_-, [J_-, ..., [J_-, J_+^k]...]]. \tag{C.10}$$

Replacing $J_- \to xJ_-$ in the above expression so that the algebraic power of x keeps track of the number of commutators involved, we have

$$T^{(k)}_{k-p} = (-1)^k \frac{2^k}{\pi^{1/4}} \sqrt{\frac{(2k+1)(k-1/2)!\,(2J-k)!}{k!\,(2J+k+1)!}} \sqrt{\frac{(2k-p)!\,p!}{(2k)!}} \tag{C.11}$$

$$\left(e^{x\,\mathrm{ad_J}_-} T^{(k)}_k\right)\Big|_{x^p\text{component}} \tag{C.12}$$

where $\mathrm{ad}_{J_-} O \equiv [J_-, O]$ for an operator O. Using the Baker-Hausdorff lemma [SN14] in the above equation, we obtain

$$\begin{aligned} T^{(k)}_{-k+p} &= (-1)^k \gamma(J,k,p) \left(e^{x\,J_-} J_+^k e^{-x\,J_-}\right)\Big|_{x^p\text{component}} \\ &= (-1)^k \gamma(J,k,p) \left(e^{x\,J_-} J_+ e^{-x\,J_-}\right)^k\Big|_{x^p\text{component}}, \end{aligned} \tag{C.13}$$

where $\gamma(J,k,p) = 2^k \sqrt{\frac{(2k+1)(k-1/2)!(2J-k)!}{\sqrt{\pi}k!(2J+k+1)!}} \sqrt{\frac{(2k-p)!(p)!}{(2k)!}}$. Simplifying the above expression further, we have

$$T^{(k)}_{k-p} = \gamma(J,k,p) \left(-J_+ + 2xJ_z + x^2 J_-\right)^k\Big|_{x^p\text{component}} \tag{C.14}$$

The above formula allows us to obtain arbitrary spherical tensor in terms of collective spin operators from the expansion of $\left(-J_+ + 2xJ_z + x^2 J_-\right)^k$. For instance, the following code in Mathematica software will produce all the spherical tensors mentioned in Table (C.1) using Eq. (C.13).

```
Clear["Global`*"]

Needs["Quantum`Notation`"];
```

```
SetQuantumAliases[];

SetQuantumObject[SubPlus[J], SubMinus[J], Subscript[J, z]];

a=(2 k +1) (k - 1/2)! (2 j - k)!;

b=Sqrt[\Pi] k! (2 j + k + 1)!;

\[Gamma][j_, k_, p_] := 2^{k} Sqrt[a/b] Sqrt[((2 k - p)! p!)/(2 k)!];

t[j_, k_, q_] := FunctionExpand[\[Gamma][j, k, k - q]] Coefficient[

(-SubPlus[J] + 2 x Subscript[J, z] + x^2 SubMinus[J])^k,x, k - q];

Do[Do[ Print["T(k=", k, ",q=", q, ")=", t[j, k, q]], {q, k, -k, -1}],

{k, 1, 3}]
```

C.2 Beyond Mean-Field Limit Using Spherical Tensor Formalism

Consider the rotated version of the LMG Hamiltonian mentioned in Eq.(2.27), which is given by

$$H = -(1-s)J_x - \frac{s}{2J}J_z^2 = -\frac{(1-s)}{2}(J_+ + J_-) - \frac{s}{2J}J_z^2 \tag{C.15}$$

The Heisenberg equations of motion associated with the LMG Hamiltonian for an arbitrary spherical tensor is given by

$$\frac{d}{dt}\langle T_q^{(k)}\rangle = -i\frac{1-s}{2}\Big(\big\langle[J_+, T_q^k]\big\rangle + \big\langle[J_-, T_q^k]\big\rangle\Big) - i\frac{s}{2J}\big\langle[J_z^2, T_q^k]\big\rangle \tag{C.16}$$

The commutator relation in Eq. (C.3) allows the simplification of the first two terms in the above equation. Using Eq. (C.2), the third term can be rewritten

$$T_0^{(1)} = \sqrt{3}\frac{1}{\sqrt{J(J+1)(2J+1)}}J_z$$

$$T_1^{(1)} = -\sqrt{\frac{3}{2}}\frac{1}{\sqrt{J(J+1)(2J+1)}}J_+$$

$$T_{-1}^{(1)} = \sqrt{\frac{3}{2}}\frac{1}{\sqrt{J(J+1)(2J+1)}}J_-$$

$$T_0^{(2)} = \frac{\sqrt{5}}{2}\frac{1}{\sqrt{J(J+1)(2J+1)(2J-1)(2J+3)}}\left(4J_z^2 - J_+J_- - J_-J_+\right)$$

$$T_1^{(2)} = -\sqrt{\frac{15}{2}}\frac{1}{\sqrt{J(J+1)(2J+1)(2J-1)(2J+3)}}\left(J_zJ_+ + J_+J_z\right)$$

$$T_{-1}^{(2)} = \sqrt{\frac{15}{2}}\frac{1}{\sqrt{J(J+1)(2J+1)(2J-1)(2J+3)}}\left(J_zJ_- + J_-J_z\right)$$

$$T_2^{(2)} = \sqrt{\frac{15}{2}}\frac{1}{\sqrt{J(J+1)(2J+1)(2J-1)(2J+3)}}J_+^2$$

$$T_{-2}^{(2)} = \sqrt{\frac{15}{2}}\frac{1}{\sqrt{J(J+1)(2J+1)(2J-1)(2J+3)}}J_-^2$$

$$T_0^{(3)} = \sqrt{\frac{7}{4}}\frac{1}{\sqrt{J(J+1)(2J+1)(2J-1)(2J+3)(J+2)(J-1)}}(4J_z^3 - J_zJ_+J_- - J_+J_zJ_- - J_zJ_-J_+ - J_-J_zJ_+ - J_+J_-J_z - J_-J_+J_z)$$

$$T_1^{(3)} = \frac{1}{2}\sqrt{\frac{7}{3}}\frac{1}{\sqrt{J(J+1)(2J+1)(2J-1)(2J+3)(J+2)(J-1)}}(J_+^2J_- + J_-J_+^2 + J_+J_-J_+ - 4J_z^2J_+ - 4J_+J_z^2 - 4J_zJ_+J_z)$$

$$T_{-1}^{(3)} = -\frac{1}{2}\sqrt{\frac{7}{3}}\frac{1}{\sqrt{J(J+1)(2J+1)(2J-1)(2J+3)(J+2)(J-1)}}(J_-^2J_+ + J_+J_-^2 + J_-J_+J_- - 4J_z^2J_- - 4J_-J_z^2 - 4J_zJ_-J_z)$$

$$T_2^{(3)} = \sqrt{\frac{35}{6}}\frac{1}{\sqrt{J(J+1)(2J+1)(2J-1)(2J+3)(J+2)(J-1)}}(J_+^2J_z + J_zJ_+^2 + J_+J_zJ_+)$$

$$T_{-2}^{(3)} = \sqrt{\frac{35}{6}}\frac{1}{\sqrt{J(J+1)(2J+1)(2J-1)(2J+3)(J+2)(J-1)}}(J_-^2J_z + J_zJ_-^2 + J_-J_zJ_-)$$

$$T_3^{(3)} = -\sqrt{\frac{35}{4}}\frac{1}{\sqrt{J(J+1)(2J+1)(2J-1)(2J+3)(J+2)(J-1)}}J_+^3$$

$$T_{-3}^{(3)} = \sqrt{\frac{35}{4}}\frac{1}{\sqrt{J(J+1)(2J+1)(2J-1)(2J+3)(J+2)(J-1)}}J_-^3$$

Table C.1: The above table contains the spherical tensor operators of rank 1, 2 and 3 obtained from Eq. (C.13)

as $[J_z^2, T_q^k] = q\{J_z, T_q^k\} = q\alpha_0^{(1)}\{T_0^{(1)}, T_q^{(k)}\}$. The anticommutator can be evaluated using the following formula

$$\{T_{q1}^{(k1)}, T_{q2}^{(k2)}\} = (-1)^{2J}\sqrt{(2k_1+1)(2k_2+1)}\sum_{\lambda=|k1-k2|}^{k1+k2}\langle k_1 q_1, k_2 q_2|\lambda, q_1+q_2\rangle \Big((-1)^{k_1+k_2}+(-1)^{\lambda}\Big)\begin{Bmatrix} k_1 & k_2 & \lambda \\ J & J & J \end{Bmatrix} T_{q_1+q_2}^{(\lambda)}, \tag{C.17}$$

Hence, Eq. (C.15) can be written as

$$\frac{d}{dt}\langle T_q^{(k)}\rangle = -i\frac{1-s}{2}\left(\sqrt{k(k+1)-q(q+1)}\langle T_{q+1}^k\rangle + \sqrt{k(k+1)-q(q-1)}\langle T_{q-1}^k\rangle\right) - i\frac{qs}{2J}(-1)^{2J}\left(c_{k+1,q}\langle T_q^{k+1}\rangle + c_{k,q}\langle T_q^{k-1}\rangle\right) \tag{C.18}$$

where $c_{k,q} = \sqrt{\frac{(k^2-q^2)(2J+k+1)(2J-k+1)}{(2k+1)(2k-1)}}$. Evaluating the above expression for rank-1 tensors, one obtains the equations of motion for the collective angular spin momentum operators (J_x, J_y, J_z). As expected, these equations will be coupled to rank-2 tensor operators, which are second-degree polynomials in collective spin operators, and the equations for rank-2 tensor operators will be coupled to higher rank tensor operators. Notice that Eq. (C.17) provides an explicit expression for all the equations of motion required to study the system. The final step in the cumulant expansion method involves ignoring higher-order correlations by setting appropriate cumulants to zero. We study this issue by explicitly analyzing two special cases.

C.2.1 Mean-field Limit

Writing out the equations of motion for rank-1 tensor operators using Eq. (C.17), we obtain

$$\begin{aligned}
\frac{d}{dt}\langle T_1^{(1)}\rangle &= -i\frac{1-s}{\sqrt{2}}\langle T_0^{(1)}\rangle - i\frac{s}{2J}\sqrt{\frac{(2J+3)(2J-1)}{5}}\langle T_1^{(2)}\rangle \\
\frac{d}{dt}\langle T_0^{(1)}\rangle &= -i\frac{1-s}{\sqrt{2}}\big(\langle T_0^{(1)}\rangle + \langle T_{-1}^{(1)}\rangle\big) \\
\frac{d}{dt}\langle T_{-1}^{(1)}\rangle &= -i\frac{1-s}{\sqrt{2}}\langle T_0^{(1)}\rangle + i\frac{s}{2J}\sqrt{\frac{(2J+3)(2J-1)}{5}}\langle T_{-1}^{(2)}\rangle
\end{aligned} \tag{C.19}$$

The above set of equations are equivalent to equations of motion shown in Eq. (2.42). However, note the variables $\big(\langle T_1^{(1)}\rangle, \langle T_{-1}^{(1)}\rangle\big)$ in the above equations are complex. Therefore, the equation associated with $\langle T_{-1}^{(1)}\rangle$ can be obtained by taking complex conjugate of the equation associated with $\langle T_1^{(1)}\rangle$ and using the property $\langle T_q^{(k)}\rangle^* = (-1)^q\langle T_{-q}^{(k)}\rangle$. Therefore, we will ignore all the equations associated with tensor operators that have negative values of q. Now, focusing on $T_1^{(2)}$, which is the relevant operator in Eq (C.18), and setting the second-order cumulant to zero ($\langle AB\rangle = \langle A\rangle\langle B\rangle$), we have

$$\langle T_1^{(2)}\rangle = -\sqrt{\frac{20}{3}}\sqrt{\frac{J(J+1)(2J+1)}{(2J-1)(2J+3)}}\langle T_0^{(1)}\rangle\langle T_1^{(1)}\rangle \tag{C.20}$$

Hence, we have the following closed set of equations in the mean-field limit (equivalent to Eq. (2.41))

$$\begin{aligned}
\frac{d}{dt}\langle T_1^{(1)}\rangle &= -i\frac{1-s}{\sqrt{2}}\langle T_0^{(1)}\rangle + is\sqrt{\frac{(J+1)(2J+1)}{3J}}\langle T_0^{(1)}\rangle\langle T_1^{(1)}\rangle \\
\frac{d}{dt}\langle T_0^{(1)}\rangle &= -i\frac{1-s}{\sqrt{2}}\big(\langle T_1^{(1)}\rangle + \langle T_{-1}^{(1)}\rangle\big)
\end{aligned} \tag{C.21}$$

C.2.2 Gaussian Limit

In this case, we set third-order cumulants to zero, which leads to approximating third-order correlations in terms of lower-order correlation functions, and ignoring fourth and higher order correlations. The equations of motion now include five (rank-2 tensor operators) additional equations as shown below

$$\begin{aligned}
\frac{d}{dt}\langle T_2^{(2)}\rangle &= -i(1-s)\langle T_1^{(2)}\rangle - i\frac{s}{J}\sqrt{\frac{2(2J+4)(2J-2)}{7}}\langle T_2^{(3)}\rangle \\
\frac{d}{dt}\langle T_1^{(2)}\rangle &= -i\frac{(1-s)}{2}\left(\sqrt{6}\langle T_0^{(2)}\rangle + 2\langle T_2^{(2)}\rangle\right) \\
&\quad - i\frac{s}{2J}\left(\sqrt{\frac{2(2J+3)(2J-1)}{5}}\langle T_1^{(1)}\rangle + \sqrt{\frac{16(2J+4)(2J-2)}{35}}\langle T_1^{(3)}\rangle\right) \\
\frac{d}{dt}\langle T_0^{(2)}\rangle &= -i\frac{(1-s)}{2}\sqrt{6}\left(\langle T_1^{(2)}\rangle + \langle T_{-1}^{(2)}\rangle\right) \\
\frac{d}{dt}\langle T_1^{(1)}\rangle &= -i\frac{1-s}{\sqrt{2}}\langle T_0^{(1)}\rangle - i\frac{s}{2J}\sqrt{\frac{(2J+3)(2J-1)}{5}}\langle T_1^{(2)}\rangle \\
\frac{d}{dt}\langle T_0^{(1)}\rangle &= -i\frac{1-s}{\sqrt{2}}\big(\langle T_0^{(1)}\rangle + \langle T_{-1}^{(1)}\rangle\big)
\end{aligned} \tag{C.22}$$

By setting third order cumulants to 0, we will have a closed set of equations containing 8 differential equations. This results in the following approximations for 3^{rd}-rank

tensor operators,

$$\begin{aligned}
\langle T_2^{(3)}\rangle &= \frac{\alpha_2^{(3)}}{\alpha_2^{(2)}\alpha_0^{(2)}} 3\langle T_2^{(2)}\rangle\langle T_0^{(1)}\rangle - \frac{\alpha_2^{(3)}}{\alpha_1^{(1)}\alpha_1^{(2)}} 3\langle T_1^{(2)}\rangle\langle T_1^{(1)}\rangle - \frac{\alpha_2^{(3)}}{\alpha_0^{(1)}(\alpha_1^{(1)})^2} 6\langle T_0^{(1)}\rangle\big(\langle T_1^{(1)}\rangle\big)^2 \\
\langle T_1^{(3)}\rangle &= \frac{\alpha_1^{(3)}}{\alpha_{-1}^{(1)}\alpha_2^{(2)}} 3\langle T_2^{(2)}\rangle\langle T_{-1}^{(1)}\rangle - \frac{\alpha_1^{(3)}}{\alpha_0^{(2)}\alpha_1^{(2)}} 3\langle T_0^{(2)}\rangle\langle T_1^{(1)}\rangle - \frac{\alpha_1^{(3)}}{\alpha_0^{(1)}\alpha_1^{(2)}} 12\langle T_0^{(1)}\rangle\langle T_1^{(2)}\rangle \\
&\quad - \frac{\alpha_1^{(3)}}{\alpha_{-1}^{(1)}\big(\alpha_1^{(1)}\big)^2} 6\langle T_{-1}^{(1)}\rangle\big(\langle T_1^{(1)}\rangle\big)^2 + \frac{\alpha_1^{(3)}}{\alpha_1^{(1)}\big(\alpha_1^{(0)}\big)^2} 24\langle T_1^{(1)}\rangle\big(\langle T_0^{(1)}\rangle\big)^2
\end{aligned} \tag{C.23}$$

where $\alpha_q^{(k)}$ is the appropriate normalization constant for the spherical tensor $T_q^{(k)}$.

Notice that in this cumulant expansion method, where we approximate a higher rank tensor operator (associated with higher-order correlations) in terms of lower rank tensor operators (lower-order correlations), a particular pattern emerges. The terms in the approximation of $\langle T_q^{(k)}\rangle$ include sum over all the terms, where each term has product of expectation values of lower-rank tensors such that sum of ranks (superscripts) and sum of the components (subscripts) involved in the product equal k and q respectively. For instance, approximating $\langle T_q^{(k)}\rangle$ by setting k^{th}-order cumulants to zero leads to an approximation that allows $\langle T_q^{(k)}\rangle$ to be written as

$$\langle T_q^{(k)}\rangle = \sum_{\substack{k_1+k_2+\ldots+k_l=k \\ q_1+q_2+\ldots+q_l=q}} \alpha_{q_1,\ldots,q_l}^{(k_1,\ldots,k_l)} \ \langle T_{q_1}^{(k_1)}\rangle\langle T_{q_2}^{(k_2)}\rangle\ldots\langle T_{q_l}^{(k_l)}\rangle \tag{C.24}$$

where each term in the above summation satisfies the conditions $k_1+k_2+\ldots+k_l=k$ and $q_1+q_2+\ldots+q_l=q$. Moreover, preliminary analysis suggests that the coefficients $\alpha_{q_1,\ldots,q_l}^{(k_1,\ldots,k_l)}$ also be predicted using combinatorics. All of this analysis suggests that a closed-form expression can be written for approximating higher-order correlation func-

tions in terms of lower-order correlation functions using the cumulant approximation method when the spherical-tensor framework is used.

In summary, cumulant approximation method involves two important steps. The first step is to write down all the differential equations that couple lower-order moments to higher-order moments. The second step involves approximating higher-order correlations, say k^{th}-order correlations, in terms of lower-order correlation functions after deciding that k^{th} and higher-order correlations will be ignored. In this Appendix, we have shown that a closed-form expression can be written for all the equations of motion in a straightforward manner, provided they are expressed in terms of spherical tensors. Moreover, we have also derived an expression for the generating function of spherical tensors in terms of the collective spin operators. Then, we have also suggested, based on our preliminary analysis, that approximating higher-order correlation functions in terms of lower-order correlation functions has a closed-form expression. This makes the spherical-tensor framework more amenable to theoretical analysis.

Finally, it needs to be pointed out that the closed set of differential equations obtained from this approximation method might not necessarily be stable. Therefore, even if one obtains the closed set of differential equations using cumulant expansion method, the solution might be unstable in the long-time limit. Hence, it is interesting in future to explore and identify if there exists any relationship between the kind of Hamiltonians that leads to stable differential equations and the physical properties of such Hamiltonians.

Bibliography

A

[AA11] Proceedings of the forty-third annual acm symposium on theory of computing, 2011.

[AAB+19] F. Arute, K. Arya, R. Babbush, D. Bacon, J. C. Bardin, R. Barends, R. Biswas, S. Boixo, F. G. Brandao, D. A. Buell, et al. Quantum supremacy using a programmable superconducting processor. *Nature*, 574(7779):505–510, 2019.

[ABC+21] E. Altman, K. R. Brown, G. Carleo, L. D. Carr, E. Demler, C. Chin, B. DeMarco, S. E. Economou, M. A. Eriksson, K.-M. C. Fu, et al. Quantum simulators: Architectures and opportunities. *PRX Quantum*, 2(1):017003, 2021.

[AGDLHG05] A. Aspuru-Guzik, A. D. Dutoi, P. J. Love, and M. Head-Gordon. Simulated quantum computation of molecular energies. *Science*, 309(5741):1704–1707, 2005.

B

[BCC+15] D. W. Berry, A. M. Childs, R. Cleve, R. Kothari, and R. D. Somma. Simulating hamiltonian dynamics with a truncated taylor series. *Physical review letters*, 114(9):090502, 2015.

[BDN12] I. Bloch, J. Dalibard, and S. Nascimbene. Quantum simulations with ultracold quantum gases. *Nature Physics*, 8(4):267–276, 2012.

[BFK+13] V. Bapst, L. Foini, F. Krzakala, G. Semerjian, and F. Zamponi. The quantum adiabatic algorithm applied to random optimization problems: The quantum spin glass perspective. *Physics Reports*, 523(3):127–205, 2013.

[BJ83] R. Botet and R. Jullien. Large-size critical behavior of infinitely coordinated systems. *Physical Review B*, 28(7):3955, 1983.

[BN09] I. Buluta and F. Nori. Quantum simulators. *Science*, 326(5949):108–111, 2009.

[Bra02] D. Braun. Quantum chaos and quantum algorithms. *Physical Review A*, 65(4):042317, 2002.

[BS12] V. Bapst and G. Semerjian. On quantum mean-field models and their quantum annealing. *Journal of Statistical Mechanics: Theory and Experiment*, 2012(06):P06007, 2012.

[BSK+17] H. Bernien, S. Schwartz, A. Keesling, H. Levine, A. Omran, H. Pichler, S. Choi, A. S. Zibrov, M. Endres, M. Greiner, et al. Probing many-body dynamics on a 51-atom quantum simulator. *Nature*, 551(7682):579–584, 2017.

C

[CAB+21] M. Cerezo, A. Arrasmith, R. Babbush, S. C. Benjamin, S. Endo, K. Fujii, J. R. McClean, K. Mitarai, X. Yuan, L. Cincio, et al. Variational quantum algorithms. *Nature Reviews Physics*, 3(9):625–644, 2021.

[Car96] J. Cardy. *Scaling and renormalization in statistical physics*, volume 5. Cambridge university press, 1996.

[CFS08] T. Caneva, R. Fazio, and G. E. Santoro. Adiabatic quantum dynamics of the lipkin-meshkov-glick model. *Physical Review B*, 78(10):104426, 2008.

[CLPHLM06] O. Castaños, R. López-Peña, J. G. Hirsch, and E. López-Moreno. Classical and quantum phase transitions in the lipkin-meshkov-glick model. *Physical Review B*, 74(10):104118, 2006.

[CMAPD21] K. Chinni, M. H. Muñoz-Arias, P. M. Poggi, and I. H. Deutsch. Trotter errors from dynamical structural instabilities of floquet maps in quantum simulation. *arXiv preprint arXiv:2110.03568*, 2021.

[CMN+18] A. M. Childs, D. Maslov, Y. Nam, N. J. Ross, and Y. Su. Toward the first quantum simulation with quantum speedup. *Proceedings of the National Academy of Sciences*, 115(38):9456–9461, 2018.

[CPD21] K. Chinni, P. M. Poggi, and I. H. Deutsch. Effect of chaos on the simulation of quantum critical phenomena in analog quantum simulators. *Phys. Rev. Research*, 3:033145, Aug 2021.

[CST+21] A. M. Childs, Y. Su, M. C. Tran, N. Wiebe, and S. Zhu. Theory of trotter error with commutator scaling. *Physical Review X*, 11(1):011020, 2021.

[CTV17] E. T. Campbell, B. M. Terhal, and C. Vuillot. Roads towards fault-tolerant universal quantum computation. *Nature*, 549(7671):172–179, 2017.

[CZ12] J. I. Cirac and P. Zoller. Goals and opportunities in quantum simulation. *Nature physics*, 8(4):264–266, 2012.

D

[Deu20] I. H. Deutsch. Harnessing the power of the second quantum revolution. *PRX Quantum*, 1(2):020101, 2020.

E

[EWL+21] S. Ebadi, T. T. Wang, H. Levine, A. Keesling, G. Semeghini, A. Omran, D. Bluvstein, R. Samajdar, H. Pichler, W. W. Ho, et al. Quantum phases of matter on a 256-atom programmable quantum simulator. *Nature*, 595(7866):227–232, 2021.

F

[Fey82] R. P. Feynman. Simulating Physics with Computers. *International Journal of Theoretical Physics*, 21(6-7):467–488, June 1982.

[FGG14] E. Farhi, J. Goldstone, and S. Gutmann. A quantum approximate optimization algorithm. *arXiv preprint arXiv:1411.4028*, 2014.

[FHD+21] T. Freeth, D. Higgon, A. Dacanalis, L. MacDonald, M. Georgakopoulou, and A. Wojcik. A model of the cosmos in the ancient greek antikythera mechanism. *Scientific reports*, 11(1):1–15, 2021.

[Fla00] V. V. Flambaum. Time dynamics in chaotic many-body systems: can chaos destroy a quantum computer? *Australian Journal of Physics*, 53(4):489–497, 2000.

G

[G+85] C. W. Gardiner et al. *Handbook of stochastic methods*, volume 3. springer Berlin, 1985.

[GAN14] I. M. Georgescu, S. Ashhab, and F. Nori. Quantum simulation. *Reviews of Modern Physics*, 86(1):153, 2014.

[GG18] S. Garfinkel and R. Grunspan. *The Computer Book: From the Abacus to Artificial Intelligence, 250 Milestones in the History of Computer Science*. Sterling Milestones Series. Sterling, 2018.

[Gol18] N. Goldenfeld. *Lectures on phase transitions and the renormalization group*. CRC Press, 2018.

[Gro96] L. K. Grover. A fast quantum mechanical algorithm for database search. In *Proceedings of the twenty-eighth annual ACM symposium on Theory of computing*, pages 212–219, 1996.

[GS00] B. Georgeot and D. L. Shepelyansky. Emergence of quantum chaos in the quantum computer core and how to manage it. *Physical Review E*, 62(5):6366, 2000.

H

[Haa91] F. Haake. Quantum signatures of chaos. In *Quantum Coherence in Mesoscopic Systems*, pages 583–595. Springer, 1991.

[HCT+12] P. Hauke, F. M. Cucchietti, L. Tagliacozzo, I. Deutsch, and M. Lewenstein. Can one trust quantum simulators? *Reports on Progress in Physics*, 75(8):082401, 2012.

[HD21] A. Haldar and A. Das. Statistical mechanics of floquet quantum matter: The exact and emergent conservation laws. *Journal of Physics: Condensed Matter*, 2021.

[HHZ19] M. Heyl, P. Hauke, and P. Zoller. Quantum localization bounds trotter errors in digital quantum simulation. *Science advances*, 5(4):eaau8342, 2019.

[HKS87] F. Haake, M. Kuś, and R. Scharf. Classical and quantum chaos for a kicked top. *Zeitschrift für Physik B Condensed Matter*, 65(3):381–395, 1987.

[HQ18] W. Hofstetter and T. Qin. Quantum simulation of strongly correlated condensed matter systems. *Journal of Physics B: Atomic, Molecular and Optical Physics*, 51(8):082001, 2018.

[HSMD21] A. Haldar, D. Sen, R. Moessner, and A. Das. Dynamical freezing and scar points in strongly driven floquet matter: Resonance vs emergent conservation laws. *Physical Review X*, 11(2):021008, 2021.

J

[JDZO+12] B. Juliá-Díaz, T. Zibold, M. Oberthaler, M. Melé-Messeguer, J. Martorell, and A. Polls. Dynamic generation of spin-squeezed states in bosonic josephson junctions. *Physical Review A*, 86(2):023615, 2012.

[JKK+10] T. Jörg, F. Krzakala, J. Kurchan, A. C. Maggs, and J. Pujos. Energy gaps in quantum first-order mean-field–like transitions: The problems that quantum annealing cannot solve. *EPL (Europhysics Letters)*, 89(4):40004, feb 2010.

K

[KDM+18] N. Klco, E. F. Dumitrescu, A. J. McCaskey, T. D. Morris, R. C. Pooser, M. Sanz, E. Solano, P. Lougovski, and M. J. Savage. Quantum-classical computation of schwinger model dynamics using quantum computers. *Physical Review A*, 98(3):032331, 2018.

[KNG+08] H.-M. Kwok, W.-Q. Ning, S.-J. Gu, H.-Q. Lin, et al. Quantum criticality of the lipkin-meshkov-glick model in terms of fidelity susceptibility. *Physical Review E*, 78(3):032103, 2008.

[Kny16] S. Knysh. Zero-temperature quantum annealing bottlenecks in the spin-glass phase. *Nature communications*, 7(1):1–9, 2016.

[KR08] A. Klimov and J. Romero. A generalized wigner function for quantum systems with the su (2) dynamical symmetry group. *Journal of Physics A: Mathematical and Theoretical*, 41(5):055303, 2008.

L

[LC17] G. H. Low and I. L. Chuang. Optimal hamiltonian simulation by quantum signal processing. *Physical review letters*, 118(1):010501, 2017.

[LC19] G. H. Low and I. L. Chuang. Hamiltonian simulation by qubitization. *Quantum*, 3:163, 2019.

[LDM14] A. Lazarides, A. Das, and R. Moessner. Periodic thermodynamics of isolated quantum systems. *Physical review letters*, 112(15):150401, 2014.

[LKP+20] N. K. Lysne, K. W. Kuper, P. M. Poggi, I. H. Deutsch, and P. S. Jessen. Small, highly accurate quantum processor for intermediate-depth quantum simulations. *Physical review letters*, 124(23):230501, 2020.

[LL13] A. J. Lichtenberg and M. A. Lieberman. *Regular and chaotic dynamics*, volume 38. Springer Science & Business Media, 2013.

[Llo96] S. Lloyd. Universal quantum simulators. *Science*, pages 1073–1078, 1996.

[LMG65] H. J. Lipkin, N. Meshkov, and A. Glick. Validity of many-body approximation methods for a solvable model:(i). exact solutions and perturbation theory. *Nuclear Physics*, 62(2):188–198, 1965.

M

[MAF+18] V. Mourik, S. Asaad, H. Firgau, J. J. Pla, C. Holmes, G. J. Milburn, J. C. McCallum, and A. Morello. Exploring quantum chaos with a single nuclear spin. *Physical Review E*, 98(4):042206, 2018.

[MAPD21] M. H. Muñoz-Arias, P. M. Poggi, and I. H. Deutsch. Nonlinear dynamics and quantum chaos of a family of kicked p-spin models. *Physical Review E*, 103(5):052212, 2021.

[McC99] S. McCartney. Eniac: The triumphs and tragedies of the world's first computer. , 1999.

[MCWW97] G. Milburn, J. Corney, E. M. Wright, and D. Walls. Quantum dynamics of an atomic bose-einstein condensate in a double-well potential. *Physical Review A*, 55(6):4318, 1997.

[MMS+16] E. A. Martinez, C. A. Muschik, P. Schindler, D. Nigg, A. Erhard, M. Heyl, P. Hauke, M. Dalmonte, T. Monz, P. Zoller, et al. Real-time dynamics of lattice gauge theories with a few-qubit quantum computer. *Nature*, 534(7608):516–519, 2016.

[MnACP22] M. H. Muñoz Arias, K. Chinni, and P. M. Poggi. *In preparation*, 2022.

[MnADJP20] M. H. Muñoz Arias, I. H. Deutsch, P. S. Jessen, and P. M. Poggi. Simulation of the complex dynamics of mean-field p-spin models using measurement-based quantum feedback control. *Phys. Rev. A*, 102:022610, Aug 2020.

[MNV+17] S. Matsuura, H. Nishimori, W. Vinci, T. Albash, and D. A. Lidar. Quantum-annealing correction at finite temperature: Ferromagnetic p-spin models. *Physical review A*, 95(2):022308, 2017.

N

[NC02] Quantum computation and quantum information, 2002.

[NO10] H. Nishimori and G. Ortiz. *Elements of phase transitions and critical phenomena*. Oup Oxford, 2010.

O

[ONL18] M. Ohkuwa, H. Nishimori, and D. A. Lidar. Reverse annealing for the fully connected p-spin model. *Physical Review A*, 98(2):022314, 2018.

P

[Per84] A. Peres. Stability of quantum motion in chaotic and regular systems. *Physical Review A*, 30(4):1610, 1984.

[Per06] A. Peres. *Quantum theory: concepts and methods*, volume 57. Springer Science & Business Media, 2006.

[PHR22] D. Plankensteiner, C. Hotter, and H. Ritsch. Quantumcumulants. jl: A julia framework for generalized mean-field equations in open quantum systems. *Quantum*, 6:617, 2022.

[PMS+14] A. Peruzzo, J. McClean, P. Shadbolt, M.-H. Yung, X.-Q. Zhou, P. J. Love, A. Aspuru-Guzik, and J. L. O'brien. A variational eigenvalue solver on a photonic quantum processor. *Nature communications*, 5(1):1–7, 2014.

[Pre18] J. Preskill. Quantum computing in the nisq era and beyond. *Quantum*, 2:79, 2018.

[PSO+18] L. Pezze, A. Smerzi, M. K. Oberthaler, R. Schmied, and P. Treutlein. Quantum metrology with nonclassical states of atomic ensembles. *Reviews of Modern Physics*, 90(3):035005, 2018.

R

[Rei92] L. E. Reichl. *The transition to chaos*, volume 6. Springer, 1992.

[RHR98] G. Rangarajan, S. Habib, and R. D. Ryne. Lyapunov exponents without rescaling and reorthogonalization. *Physical Review Letters*, 80(17):3747, 1998.

[RWS+17] M. Reiher, N. Wiebe, K. M. Svore, D. Wecker, and M. Troyer. Elucidating reaction mechanisms on quantum computers. *Proceedings of the National Academy of Sciences*, 114(29):7555–7560, 2017.

S

[Sac11] S. Sachdev. *Quantum phase transitions*. Cambridge university press, 2011.

[SC93] R. Schack and C. M. Caves. Hypersensitivity to perturbations in the quantum baker's map. *Physical review letters*, 71(4):525, 1993.

[Sho94] P. W. Shor. Algorithms for quantum computation: discrete logarithms and factoring. In *Proceedings 35th annual symposium on foundations of computer science*, pages 124–134. Ieee, 1994.

[SKS+21] C. N. Self, K. E. Khosla, A. W. Smith, F. Sauvage, P. D. Haynes, J. Knolle, F. Mintert, and M. Kim. Variational quantum algorithm with information sharing. *npj Quantum Information*, 7(1):1–7, 2021.

[SML+14] H. Strobel, W. Muessel, D. Linnemann, T. Zibold, D. B. Hume, L. Pezzè, A. Smerzi, and M. K. Oberthaler. Fisher information and entanglement of non-gaussian spin states. *Science*, 345(6195):424–427, 2014.

[SN14] J. Sakurai and J. Napolitano. Modern quantum mechanics 2nd edition. *Person New International edition*, 2014.

[SOE+19] L. M. Sieberer, T. Olsacher, A. Elben, M. Heyl, P. Hauke, F. Haake, and P. Zoller. Digital quantum simulation, trotter errors, and quantum chaos of the kicked top. *npj Quantum Information*, 5(1):1–11, 2019.

[SS01] P. H. Song and D. L. Shepelyansky. Quantum computing of quantum chaos and imperfection effects. *Physical review letters*, 86(10):2162, 2001.

[SSS20] A. Sehrawat, C. Srivastava, and U. Sen. Equilibrium and dynamical phase transitions in fully connected quantum ising model: Approximate energy eigenstates and critical time. *arXiv preprint arXiv:2012.00561*, 2020.

[SSW+21] P. Scholl, M. Schuler, H. J. Williams, A. A. Eberharter, D. Barredo, K.-N. Schymik, V. Lienhard, L.-P. Henry, T. C. Lang, T. Lahaye, et al. Quantum simulation of 2d antiferromagnets with hundreds of rydberg atoms. *Nature*, 595(7866):233–238, 2021.

[STPB16] L. F. Santos, M. Távora, and F. Pérez-Bernal. Excited-state quantum phase transitions in many-body systems with infinite-range interaction: Localization, dynamics, and bifurcation. *Physical Review A*, 94(1):012113, 2016.

[SZZ17] M. Sarovar, J. Zhang, and L. Zeng. Reliability of analog quantum simulation. *EPJ quantum technology*, 4(1):1–29, 2017.

T

[TLM+19] A. Tranter, P. J. Love, F. Mintert, N. Wiebe, and P. V. Coveney. Ordering of trotterization: Impact on errors in quantum simulation of electronic structure. *Entropy*, 21(12):1218, 2019.

[TMS+17] J. Tomkovič, W. Muessel, H. Strobel, S. Löck, P. Schlagheck, R. Ketzmerick, and M. K. Oberthaler. Experimental observation of the poincaré-birkhoff scenario in a driven many-body quantum system. *Physical Review A*, 95(1):011602, 2017.

V

[VA00] A. Vardi and J. R. Anglin. Condensates beyond mean field theory: quantum backreaction as decoherence. *arXiv preprint physics/0007054*, 2000.

W

[WSH19] B.-B. Wei, G. Sun, and M.-J. Hwang. Dynamical scaling laws of out-of-time-ordered correlators. *Physical Review B*, 100(19):195107, 2019.

X

[XSL+20] K. Xu, Z.-H. Sun, W. Liu, Y.-R. Zhang, H. Li, H. Dong, W. Ren, P. Zhang, F. Nori, D. Zheng, et al. Probing dynamical phase transitions with a superconducting quantum simulator. *Science advances*, 6(25):eaba4935, 2020.

Y

[YN11] J. You and F. Nori. Atomic physics and quantum optics using superconducting circuits. *Nature*, 474(7353):589–597, 2011.

Z

[ŽHKS18] B. Žunkovič, M. Heyl, M. Knap, and A. Silva. Dynamical quantum phase transitions in spin chains with long-range interactions: Merging different concepts of nonequilibrium criticality. *Physical review letters*, 120(13):130601, 2018.

[ZLI+21] X. Zhou, W.-S. Lee, M. Imada, N. Trivedi, P. Phillips, H.-Y. Kee, P. Törmä, and M. Eremets. High-temperature superconductivity. *Nature Reviews Physics*, pages 1–4, 2021.

[ZPH+17] J. Zhang, G. Pagano, P. W. Hess, A. Kyprianidis, P. Becker, H. Kaplan, A. V. Gorshkov, Z.-X. Gong, and C. Monroe. Observation of a many-body dynamical phase transition with a 53-qubit quantum simulator. *Nature*, 551(7682):601–604, 2017.

[ZWD+20] H.-S. Zhong, H. Wang, Y.-H. Deng, M.-C. Chen, L.-C. Peng, Y.-H. Luo, J. Qin, D. Wu, X. Ding, Y. Hu, et al. Quantum computational advantage using photons. *Science*, 370(6523):1460–1463, 2020.